This dissertation thesis aims to develop a cost-effective and reliable partial discharge (PD) sensor for online monitoring of power cables. The research focuses on improving high-frequency current transformers (HFCT) to overcome magnetic saturation issues and optimize their sensitivity. The research begins by investigating the nature of PD signals transmitted along power cables and their measurable bandwidth. An analytical power cable model is developed to simulate the transmission process and determine the remaining bandwidth at the cable ends where the PD sensors are installed. Based on these findings, an optimized HFCT sensor design is investigated, which guarantees maximum sensitivity to PD pulses. For this purpose, an analytical HFCT model is derived.

However, the challenge with HFCTs is their susceptibility to magnetic saturation caused by the high 50 Hz operating currents of power cables. To address this issue, an improved split-core HFCT design is proposed, capable of self-adjusting its air gap length based on the saturation level. A microcontroller controls a servo motor to optimize the air gap length in real-time, ensuring maximum sensitivity without saturation. This solution enables online monitoring of power cables using HFCT technology.

The key contributions of this thesis include the improved split-core HFCT design with self-adjusting air gap length, an analytical power cable model for HF signal transmission, an analytical HFCT model for design optimization, and a method for real-time PD signal evaluation. Future work should focus on further optimizing the sensor design and integrating advanced methods for PD detection and signal evaluation.

ISSN 1612-2526
ISBN 978-3-948749-43-9
DOI 10.24352/UB.OVGU-2024-050

Martin Fritsch: Measurement of Partial Discharges on Power Cables

MAFO 98

Res Electricae Magdeburgenses
MAgdeburger FOrum zur Elektrotechnik

Martin Fritsch

Measurement of Partial Discharges on Power Cables: A Step Towards Successful Online Monitoring

Magdeburg 2024

MAFO
Band 98

Measurement of Partial Discharges on Power Cables: A Step Towards Successful Online Monitoring

Dissertation

zur Erlangung des akademischen Grades

Doktoringenieur

(Dr.-Ing.)

von **M. Sc. Martin Fritsch**

geb. am 25.05.1993 in Mühlhausen

genehmigt durch die Fakultät für Elektrotechnik und Informationstechnik
der Otto-von-Guericke-Universität Magdeburg

Gutachter:

Univ.-Prof. Dr.-Ing. habil. Martin Wolter

Univ.-Prof. Dr.-Ing. Peter Werle

Promotionskolloquium am 12. März 2024

Res Electricae Magdeburgenses

Magdeburger Forum zur Elektrotechnik, Jg. 22, Band 98, 2024
http://www.mafo.ovgu.de/

IMPRESSUM

Herausgeber:

- Prof. Dr.-Ing. Andreas Lindemann, Lehrstuhl für Leistungselektronik, Institut für Elektrische Energiesysteme
- Prof. Dr.-Ing. habil. Martin Wolter, Lehrstuhl für Elektrische Netze und Erneuerbare Energie, Institut für Elektrische Energiesysteme
- Prof. Dr. rer. nat. Georg Rose, Lehrstuhl für Medizinische Telematik/Medizintechnik, Institut für Medizintechnik
- Prof. Dr.-Ing. Ralf Vick, Lehrstuhl für Elektromagnetische Verträglichkeit, Institut für Medizintechnik

Gründungsherausgeber:

- Prof. Dr. rer. nat. habil. Jürgen Nitsch
- Prof. Dr.-Ing. habil. Zbigniew Antoni Styczynski

alle: Otto-von-Guericke-Universität Magdeburg
Postfach 4120, 39016 Magdeburg

V. i. S. d. P.:
Dr.-Ing. Martin Fritsch
Otto-von-Guericke-Universität Magdeburg, Postfach 4120, 39016 Magdeburg

1. Auflage, Magdeburg, Otto-von-Guericke-Universität, 2024
Zugl.: Magdeburg, Univ., Diss., 2024

Auflage: 20
Redaktionsschluss: April 2024

ISSN: 1612-2526
ISBN: 978-3-948749-43-9
DOI: 10.24352/UB.OVGU-2024-050

Bezug über die Herausgeber

Druck: docupoint GmbH
Otto-von-Guericke-Allee 14, 39179 Barleben

Kurzzusammenfassung

Die elektrischen Verteilnetze, welche zu einem hohen Anteil aus Energiekabeln bestehen, werden in Zukunft einer zunehmenden Auslastung ausgesetzt sein und eine wichtigere Rolle im Energieversorgungssystem spielen. Die höhere Auslastung ist ein Problem, da die meisten Energiekabel bereits Jahrzehnte alt sind und die elektrische Festigkeit ihrer Isolierung sich mit der Zeit verschlechtert. Da der Zustand der Kabelisolierung den Verteilnetzbetreibern (VNB) im Allgemeinen nicht bekannt ist, wird das Risiko für Kabelausfälle entsprechend steigen. Um kostspielige Versorgungsunterbrechungen zu vermeiden, benötigen die VNB daher eine zustandsorientierte Instandhaltungsstrategie für ihre Energiekabel. Die gebräuchlichste Methode zur Zustandsüberwachung ist die Teilentladungsmessung (TE), die kleine elektrische Entladungen an Isolierungsdefekten frühzeitig erkennt. Heutige TE-Sensoren sind jedoch üblicherweise nicht für eine kontinuierliche Online-Überwachung konzipiert und oft schlicht zu teuer, weshalb ihre Anwendung für VNB erheblich eingeschränkt ist.

Ziel dieser Dissertation ist daher die Entwicklung eines günstigen und zuverlässigen TE-Sensors zur Online-Überwachung von Energiekabeln. Der Fokus der Forschung liegt auf der Verbesserung von Hochfrequenz-Stromwandlern (HFCT), um deren Probleme bezüglich magnetischer Sättigung zu überwinden und ihre Empfindlichkeit zu optimieren. Zu Beginn der Arbeit wird hierzu das Übertragungsverhalten von TE-Signalen auf Energiekabeln und ihre messbare Bandbreite untersucht. Hierzu wird ein analytisches Energiekabelmodell hergeleitet, um die verbleibende Bandbreite der TE-Impulse an den Kabelenden, an denen die TE-Sensoren installiert werden, zu bestimmen. Auf Grundlage dieser Erkenntnisse wird ein optimiertes HFCT-Sensordesign ermittelt. Zu diesem Zweck wird ein analytisches HFCT-Modell entwickelt.

Die eigentliche Herausforderung bei der Nutzung von HFCTs zur Online-TE-Messung ist jedoch deren Anfälligkeit für magnetische Sättigung, verursacht durch die hohen 50-Hz-Betriebsströme der Energiekabel. Zur Lösung dieses Problems wird ein verbessertes HFCT-Design mit geteiltem Kern vorgeschlagen, wobei der Sensor in der Lage ist, die Luftspaltlänge selbstständig entsprechend des derzeitigen Sättigungsniveaus zu variieren. Ein Mikrocontroller steuert hierzu einen Servomotor an, um die Luftspaltlänge in Echtzeit zu regeln und maximale Empfindlichkeit ohne Sättigung zu gewährleisten. Diese Lösung ermöglicht die Online-Überwachung von Energiekabeln mit HFCT-Technologie.

Zu den wichtigsten Beiträgen dieser Arbeit gehören das verbesserte Split-Core HFCT-Design mit selbstregelnder Luftspaltlänge, ein analytisches Übertragungsleitungsmodell für die HF-Signalübertragung, ein analytisches HFCT-Modell zur Designoptimierung und eine Methode zur Echtzeitauswertung der TE-Messung. Zukünftige Arbeiten sollten sich der weiteren Optimierung des Sensordesigns und der Integration fortgeschrittener Methoden zur TE-Detektion und Signalauswertung widmen.

Abstract

The electrical distribution grids, which are mainly build on power cables, will face higher loads in the future and will thus play an increasingly important role in the power supply system. This is a problem because most power cables are already several decades old and the dielectric strength of their insulation deteriorates over time. Since the condition of the power cable insulation is usually unknown to the distribution system operators (DSO), the risk of cable failures will increase accordingly. To prevent costly supply interruptions, the DSOs require a condition-based maintenance strategy for their power cables. The most common method for condition monitoring is partial discharge (PD) measurement, which detects small electrical discharges occurring at insulation defects at an early stage. However, today's PD sensors are usually not designed for continuous online monitoring and are often very expensive, which limits their usefulness for DSOs.

This dissertation thesis aims to develop a cost-effective and reliable PD sensor for online monitoring of power cables. The research focuses on improving high-frequency current transformers (HFCT) to overcome magnetic saturation issues and optimize their sensitivity. The research begins by investigating the nature of PD signals transmitted along power cables and their measurable bandwidth. An analytical power cable model is developed to simulate the transmission process and determine the remaining bandwidth at the cable ends where the PD sensors are installed. Based on these findings, an optimized HFCT sensor design is investigated, which guarantees maximum sensitivity to PD pulses. For this purpose, an analytical HFCT model is derived.

However, the challenge with HFCTs is their susceptibility to magnetic saturation caused by the high 50 Hz operating currents of power cables. To address this issue, an improved split-core HFCT design is proposed, capable of self-adjusting its air gap length based on the saturation level. A microcontroller controls a servo motor to optimize the air gap length in real-time, ensuring maximum sensitivity without saturation. This solution enables online monitoring of power cables using HFCT technology.

The key contributions of this thesis include the improved split-core HFCT design with self-adjusting air gap length, an analytical power cable model for HF signal transmission, an analytical HFCT model for design optimization, and a method for real-time PD signal evaluation. Future work should focus on further optimizing the sensor design and integrating advanced methods for PD detection and signal evaluation.

Contents

List of Figures

List of Tables

List of Symbols

Symbols printed in bold depict vectors and matrices.

Greek letters

α	attenuation constant	Np/m	σ	electrical conductivity	S/m
β	phase constant	rad/m	τ	relaxation time	s
δ	skin depth	m	$\underline{\gamma}$	propagation constant	Np/m
λ	wavelength	m	$\underline{\mu}$	relative permeability	-
Φ	magnetic flux	Vs	$\underline{\varepsilon}$	relative dielectric permittivity	-
ω	angular frequency	rad/m	ζ	broadness of relaxation peak	-
ϕ	rotation angle	°			

Physics Constants

μ_0	vacuum permeability	$1.25664 \cdot 10^{-6}$ Vs/Am
ε_0	dielectric permittivity of vacuum	$8.85418 \cdot 10^{-12}$ As/Vm

Variables

$\underline{I}$	current spectral density	A/Hz	d	thickness or distance	m
$\underline{r}$	reflection coefficient	-	E	electrical field strength	V/m
$\underline{U}$	voltage spectral density	V/Hz	F	amplitude factor	-
A	cross-section area	m^2	f	frequency	Hz
B	magnetic flux density	T	G	gain	-
C	capacitance	F	G'	insulator conductance	S/m
c	pulse width in PD model	s	H	magnetic field strength	A/m
C'	insulator capacitance	F/m	h	height	m

i	current in time domain	A
J	current density	A/m^2
k	correction factor	-
L	inductance	H
l	length	m
L'	conductor inductance	H/m
N	number of samples	-
n	number	-
R	resistance	Ω
r	radius	m
R'	conductor resistance	Ω/m
S	scattering parameter	-
t	time	s
u	voltage in time domain	V
v	velocity	m/s
Y'	shunt admittance	S/m
Z	impedance	Ω
z	position or location	m
Z'	series impedance	Ω/m

Indices

50 Ω	measured at 50 Ω termination
∞	at infinite frequency
σ	leakage
-3 dB	-3 dB cut-off frequency
-6 dB	-6 dB cut-off frequency
50 Hz	at frequency 50 Hz
air	air gap
amp	amplified
b	backward
bnc	BNC cable
cal	calibrator (used to generate PD-like pulses)
c	characteristic; core
co	copper
dB	converted to logarithmic scale
DC	at frequency 0 Hz
dec	decrease
eff	effective
fe	core losses
f	forward
FF	fringing flux
FFT	fast Fourier transform
FWHM	full width at half maximum
hf	high-frequency
I	current related
in	inner
ins	insulation
lin	linear

L	load (HFCT output)
max	maximum
meas	measurement; measured
min	minimum
M	material
m	magnetizing
mod	model
opt	optimum
out	outer
PD	partial discharge
peak	peak detector output voltage
pot	potentiometer
p	parasitic
r	rated
Sat	saturation; saturated
sc1	inner semiconducting layer
sc2	outer semiconducting layer
sc	oscilloscope
s	source; sampling
tot	total
T	transfer (HFCT sensitivity)
t	termination
U	voltage related
weak	at defective spot
z	at position z (coordinate)

List of Abbreviations

ADC analog-to-digital converter

BNC Bayonet Neill Concelman

CAD computer aided design

DFT discrete Fourier transform

DSO distribution system operator

FDM fused deposition modeling

FFT fast Fourier transform

FWHM full width at half maximum

HF high-frequency

HFCT high-frequency current transformer

HV high voltage

IEC international electrotechnical commission

MV medium voltage

PCB printed circuit board

PD partial discharge

RMS root mean square

RX receive

SAIDI system average interruption duration index

SMA sub miniature version A

THD total harmonic distortion

TX transmit

UHF ultra-high-frequency

VHF very-high-frequency

VNA vector network analyzer

VSD voltage spectral density

XLPE cross-linked polyethylene

1 Introduction

Due to the transformation of the electrical energy system towards renewable energies, energy transport is increasingly shifting to the distribution grid level. At the same time, the distribution systems are characterized by a high degree of cabling. In Germany, for example, around 80 percent of all transmission lines at the medium voltage (MV) level (6 – 30 kV) are power cables, which corresponds to a total length of about 400 000 km [1]. Most of these power cables are decades old and the condition of their electrical insulation is unknown. The power cable insulation is usually made of organic polymers like cross-linked polyethylene (XLPE), and it is known that its dielectric strength decreases with age [2], [3]. At the same time, the load on most power cables will increase in the near future as more and more decentralized power generation and electrical loads are connected to the distribution grids (higher bidirectional load flow due to energy transition) [4], [5]. Cable failures will therefore occur more frequently in the coming decades and the consequences of these failures in terms of grid stability will become more critical.

In order to maintain the high level of supply security (SAIDI of 12.7 minutes in Germany in 2021 [6]), the introduction of a condition-based maintenance strategy for all power cables would be beneficial for each distribution system operator (DSO) to avoid cable failures and resulting supply interruptions. For this purpose, it would be necessary to permanently monitor the insulation condition of all power cables. The most common method for this task is to measure the partial discharge (PD) content of the power cables with PD sensors. So far, however, no DSO continuously monitors its grid for PDs, as today's PD sensors are not suitable for online monitoring. Instead, DSOs only monitor their grids for power cable failures and can only react once a power cable already broke down. Successful PD monitoring allows DSOs to act proactively and not just reactively.

PDs are small electrical breakdowns that occur at defects in the dielectric insulation of power cables (or any other assets). The PD activity does not destroy the cable immediately, as in the case of a short-circuit, but lasts for a while, gradually damaging the dielectric insulation. PDs are thus a first indicator of defective high voltage (HV) insulation and can be measured as weak current pulses with amplitudes in the milliampere range and pulse widths of only a few nanoseconds [7].

There are several known methods for measuring PDs. For a comprehensive overview, see [8], [9]. The most common method is PD measurement based on the IEC 60270 standard, using capacitive sensors with a narrow bandwidth of usually < 400 kHz [10]. This method is a pure offline PD measurement and therefore not suitable for any online monitoring. Another popular approach, used especially for measuring PD on power

cables, is the use of inductive sensors called high-frequency current transformers (HFCT). These sensors have a wide bandwidth up into the MHz range, but are also usually only suitable for offline monitoring because their magnetic core easily saturates when the power cable is online [11], [12]. Accordingly, today's commercially available HFCTs are mainly used for offline monitoring, and the scientific literature does not yet provide a general solution to the saturation problem. There are some other approaches to PD measurement based on the electromagnetic radiation of the PDs or on their acoustic or optical emissions. However, none of these approaches is suitable for PD monitoring of power cables. Electromagnetic emissions associated with PDs on power cables are very low because power cables are low-pass filters for the PD signals and the cable terminations have poor antenna geometry (the rest of the cable is shielded anyway). Acoustic as well as optical phenomena do not occur with power cables because they are underground lines.

In summary, if a DSO's power cables were constantly monitored for PDs, incipient cable failures could be predicted in time to prevent costly supply interruptions. Such online monitoring offers a number of advantages:

- Continuous PD measurement in real-time
- Capture of all PD events instead of random short-term offline measurements
- No interruption of the power supply during measurement
- Monitoring of power cables under real operating conditions

However, continuous online monitoring of power cables is rarely performed due to the lack of suitable PD sensors. Today, most commercial PD measurement systems are designed for routine testing according to the IEC 60270 standard and are not optimized for online monitoring. Such devices are powerful tools, but must be evaluated by hand and are far too expensive to monitor just one single power cable. Accordingly, there is still a need among DSOs for cost-effective and reliable PD detectors to reduce outages and thus costs.

This thesis therefore deals with the development of a PD sensor for online monitoring of power cables. The sensor should be as inexpensive as possible while providing maximum sensitivity to the PD pulses. The development is based on the inductive HFCT approach, as it is the most promising for online power cable monitoring. Today's HFCTs are usually designed for offline measurements only, as they are susceptible to magnetic saturation [12]–[14]. In this work, HFCT technology is improved to enable online monitoring. In this way, this thesis wants to take a small step towards establishing a PD online monitoring for power cables.

1.1 Partial Discharges

A PD is a localized dielectric breakdown of an electrical insulation under HV stress [10]. PDs can thus occur in the electrical insulation system of any HV asset. In this work, PD always refers to internal PD that arise at weak spots within a solid electrical insulator, e. g., in power cables. There are other PD phenomena such as surface or corona discharge, but they are not relevant in the context of this thesis because they do not occur in the solid insulation of power cables.

Fig. 1.1 shows part of the cross-section of a simplified power cable. The cable consists of three coaxial layers, namely an inner conductor, an outer conductor and the dielectric insulation layer in between. A voltage is applied between the inner and outer conductors, creating an electric field $\boldsymbol{E}$. The dielectric strength of the solid insulating layer must be strong enough to withstand this electric field. As long as this condition is met, there will be no voltage breakdown. On the left side of the figure, the insulation is of good quality, so the condition of the cable is fine.

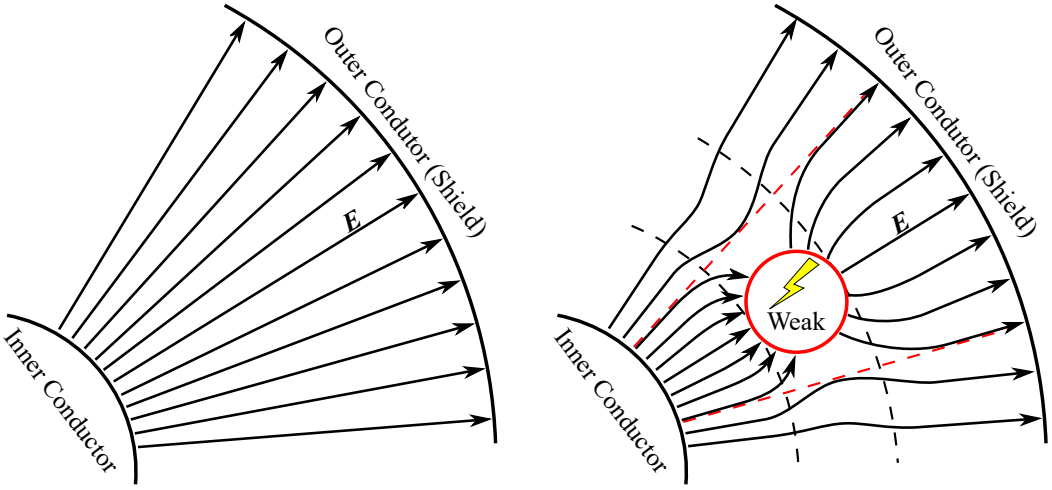

Figure 1.1: Cross-section of a power cable, left in good condition, right with defective insulation. PDs arise at weak spots in the solid insulating layer. The discharge does not bridge the whole distance between the two conductors.

On the right side, the insulation has a weak spot, which may be caused, for example, by external impacts or by the natural aging of the cable. The formation of a PD pulse can best be imagined by thinking of the weak spot as a cavity filled with gas. Inside this cavity, the permittivity is lower than that of the original insulation $\varepsilon_{\text{weak}} < \varepsilon_{\text{ins}}$, which is why the electric field is more concentrated at this point. In addition, the dielectric strength at the weak point is reduced. For these reasons, the weak spot cannot withstand the high voltage and a local breakdown occurs. The discharge bridges only part of the distance between the two conductors, so it is a partial discharge. PDs do not destroy the

power cable immediately, but they persist and gradually deteriorate the insulating layer. The appearance of PD pulses is thus an important indicator of incipient cable failure.

In the time domain, PDs are transient electromagnetic pulses characterized by a short pulse duration. Two exemplary PD pulses are shown in Fig. 1.2, left. The pulses can be described by their amplitude $\hat{u}_{\mathrm{PD}}$ and pulse width t_{FWHM}, which is defined as full width at half maximum (FWHM). The pulse widths are usually in the nanosecond range [8].

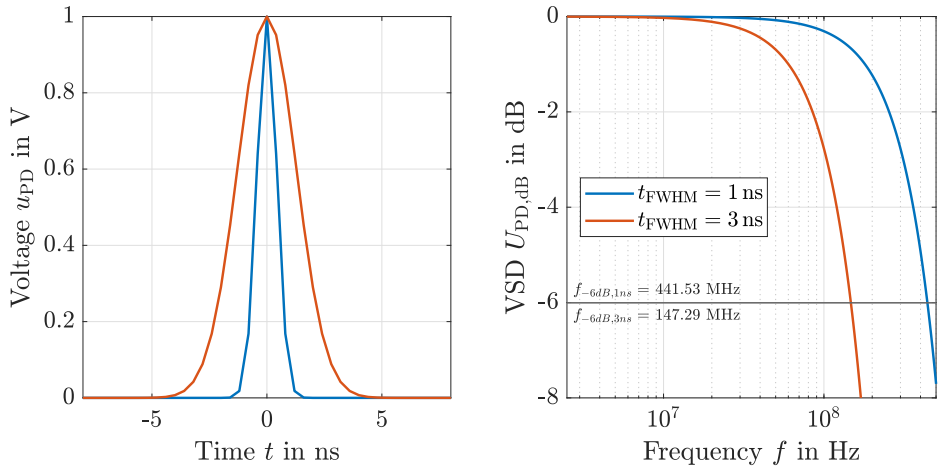

Figure 1.2: Two exemplary PD pulses in the time and frequency domain. Both pulses have an amplitude of $\hat{u}_{\mathrm{PD}} = 1\,\mathrm{V}$ and last only a few nanoseconds. Their pulse width t_{FWHM} is defined by the Full Width at Half Maximum (FWHM).

The Fourier transform can be used to transform the PD signals from the time domain to the frequency domain $u_{\mathrm{PD}}(t) \overset{\mathcal{F}}{\longrightarrow} \underline{U}_{\mathrm{PD}}(f)$. When referring to Fourier transform in this work, Matlab's fast Fourier transform (FFT) algorithm is used to compute the discrete Fourier transform (DFT) of the measured signal. For better scaling, the DFT is then divided by the sampling frequency of the measurement vector to see how the spectral content is distributed over frequency. The result $\underline{U}_{\mathrm{PD}}(f)$ is the voltage spectral density (VSD) of the measured PD pulses in $\frac{\mathrm{V}}{\mathrm{Hz}}$ [15]. For the figures it is useful to convert the VSD to a logarithmic scale:

$$U_{\mathrm{PD,dB}}(f) = 20\log_{10}\left(\frac{|\underline{U}_{\mathrm{PD}}(f)|}{\max\left(|\underline{U}_{\mathrm{PD}}(f)|\right)}\right) \tag{1.1}$$

The logarithmic VSD of the exemplary PD pulses is shown in Fig. 1.2, right. The nanosecond pulses are composed of a wide frequency spectrum from 0 Hz to several tens of MHz. The shorter the pulse duration, the wider the corresponding frequency spectrum, as can be seen in the figure.

Using the logarithmic scale, it is possible to determine the -6 dB cut-off frequency of a PD pulse $f_{-6\,\mathrm{dB}}$, which corresponds to its bandwidth. A superposition of sinusoids with frequencies from 0 Hz to the -6 dB frequency forms the voltage pulse in the time domain. At -6 dB, the spectral amplitude has decreased by half. In general, the shorter the pulse, the wider its bandwidth. With a PD duration of 1 ns, the cut-off frequency is about $f_{-6\,\mathrm{dB}} = 440\,\mathrm{MHz}$. The cut-off frequency of the 3 ns pulse is $f_{-6\,\mathrm{dB}} \approx 147\,\mathrm{MHz}$ and is therefore much lower.

So, it can be seen that the PD signal spectrum usually covers the entire high-frequency (HF: 3 – 30 MHz) range and parts of the very-high-frequency (VHF: 30 – 300 MHz) range and sometimes even extends into the ultra-high-frequency (UHF: 0.3 – 3 GHz) range for very short PD pulses. A PD sensor with a measuring bandwidth extending into the HF range can thus record a large part of the spectrum of all PDs. It should be remembered that the standard PD measurement method according to IEC 60270 only measures in a bandwidth of $< 400\,\mathrm{kHz}$. It is obvious that any PD measurement method that uses a higher bandwidth is superior to the standard method.

However, most of the PD sensors available on the market today, especially those for power cables, are based on the standard method [16]. In addition to the low measurement bandwidth, the standard method has another major disadvantage. It is an offline measurement method, i. e., the device under test must be switched off and an artificial test voltage is applied [17]. Since PDs occur stochastically [18]–[20], sporadic measurements on randomly selected power cables are not meaningful. Only permanent online monitoring makes sense. Therefore, all power cables in a distribution grid must be equipped with an individual PD sensor. For this purpose, a large number of PD sensors are required, which must therefore be as cost-effective as possible. Another disadvantage of most of today's PD sensor systems is that the measurements have to be evaluated manually. This does not meet the requirements of online monitoring, which should evaluate the measurement data automatically and in real-time. Neither research nor any company has yet offered a final solution to all these problems.

1.2 Research Objective and Contribution of the Work

The DSOs' grids are mainly based on old power cables, the condition of the electrical insulation of which is not known. At the same time, the distribution grids will be exposed to increased stress in the future due to the increasing trends towards decentralized energy generation, electromobility, heat pumps and electricity-based industrial processes. Thus, cable failures will become more serious in terms of grid stability. In order to avoid cable failures and thus costly supply interruptions, it would be good to know the condition of all power cables to establish condition-based maintenance. The key to condition monitoring of power cables is PD measurement.

Unfortunately, as of today, there are no PD sensors available that meet all the requirements placed on them:

- Ability for continuous online monitoring
- Sensor performance should not be affected by the high 50 Hz operating currents of the power cable (e. g., magnetic saturation of HFCT sensors)
- Costs per unit must be as low as possible, since each cable must be equipped with an individual sensor
- No galvanic coupling between sensor and power cable is allowed
- Measurement data must be processed and evaluated automatically and in real-time

Based on these requirements, this thesis aims to develop a PD sensor with the maximum possible sensitivity. In order to solve this task, many open research questions had to be answered step by step. The following paragraphs provide an overview of the main research objectives and structure of this work.

At the beginning of the work, it is investigated how the measurable PD signals on power cables look like. The problem is, that usually only the cable ends are accessible for sensor installation, while PDs can occur along the entire length of the power cable. The PD signals must therefore propagate along the power cable before measurement. Since power cables are poor transmitters of HF signals such as PD, they are strongly attenuated and distorted along their way. To understand this transmission process, a power cable model suitable for the HF range is presented in Chapter 2. The focus is on XLPE power cables, as they account for the largest share of all installed power cables [21]. The developed power cable model is then used to investigate the measurable bandwidth of the PD signals remaining at the cable end.

Based on the obtained results, a PD sensor optimized for power cables is next being developed. It is concluded that HFCT technology is best suited for this task. Accordingly, the next step is to find an optimal HFCT design for the defined measurement bandwidth. Since there is almost no scientific literature on this topic, the optimization of an HFCT for a specific bandwidth is still an open research question. Therefore, in Chapter 3, an analytical HFCT model is derived and validated with measurements from various self-made HFCT sensors. This HFCT model is then used to find an optimized HFCT design that guarantees maximum sensitivity within the defined measurement bandwidth. However, this HFCT design is not yet suitable for online monitoring of power cables.

A major problem when using HFCTs to measure PDs online is magnetic saturation of the sensor core due to the high 50 Hz operating current of the power cable. So the next research question is how to improve HFCT technology for online monitoring. To avoid saturation and maintain the high PD sensitivity of the optimized HFCT prototype,

air gaps are inserted into its magnetic core, i. e., a split-core is used. These air gaps should be large enough to avoid saturation, but no larger, or the sensitivity of the HFCT will be unnecessarily reduced. In addition, the optimum air gap length varies with the amplitude of the 50 Hz operating current of the power cable. Chapter 4 deals with the air gap problem in detail and presents solutions for determining the optimal air gap length of HFCT cores. It is concluded that the conventional HFCT design with a constant air gap length is not practical. Instead, to ensure the highest possible sensitivity at all times, the air gap length of the HFCT must vary over time.

Therefore, an improved split-core HFCT capable of self-adjusting its air gap length is developed, manufactured and tested in Chapter 5. The air gap is controlled in real-time based on the saturation level of the HFCT core. For this purpose, a microcontroller is used to control a servo motor that optimally adjusts the air gap length of the HFCT. According to today's scientific literature, no such HFCT system exists to date. The developed solution proves that HFCT technology can be used for online monitoring of power cables and is patent pending.

The main contributions of this thesis are:

- the improved split-core HFCT that can self-adjust its air gap length based on the saturation level, and the corresponding control strategy.
- the analytical transmission line model valid for the HF range.
- the analytical HFCT model to calculate the transfer function of any HFCT design.
- the developed method of signal evaluation for the detection of PDs in real-time.

The topic of online monitoring of power cables with HFCT sensors does not have a large focus in the scientific community. Accordingly, there is a great lack of high-quality publications on this topic. It therefore makes no sense to write a separate chapter just to give an overview of the existing literature. Instead, the few articles and papers that are relevant in the context of this thesis are cited directly in the respective chapters.

2 Transmission of PD Pulses on Power Cables

A PD can occur anywhere in the insulation of a power cable. The point of origin of a PD pulse can therefore be anywhere along the cable length, as shown in Fig. 2.1. From the point of origin, the PDs propagate in both directions along the power cable. A measurement can usually only be made at the ends of the power cable, as the rest of it is buried and therefore not accessible. Accordingly, before measurement, the PD signal must first propagate from its point of origin to the measurement point. This propagation is not loss-free, i. e., the PD pulses are attenuated and distorted on their way. The attenuation increases with the distance traveled. At the end of the cable, only a portion of the initial PD signal remains to be measured [22].

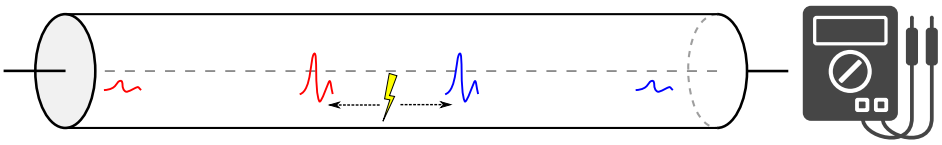

Figure 2.1: Schematic transmission of a PD pulse along a power cable. The PD signal must travel the distance between its point of origin and the measurement point and is subject to attenuation and dispersion.

To develop an efficient PD sensor, the residual signal at the end of the power cable must be known. For this purpose, a model is needed that describes the propagation of PD signals on transmission lines. In this chapter, such a model is derived and validated. Furthermore, simulations with this model are shown to analyze PD transmission on power cables.

The following Section 2.1 explains how PD pulses can be modeled. Then, Section 2.2 presents the transmission line model. Afterwards, in Section 2.3, the propagation behavior of power cables is analyzed. Section 2.4 provides a quick guide on how to use the model, while Section 2.5 presents measurements to validate it. Finally, Section 2.6 presents simulation results for the analysis of PD transmission on power cables. Parts of this chapter have been published in [23], [24].

2.1 Partial Discharge Model

Most of the PD pulses used for the experiments in this work are artificially generated using a Haefely KAL9511 PD calibrator (shown in Fig. 2.10 on page 28). This calibrator can generate PD-like pulses with an adjustable charge from 1 to 100 pC. The output voltage $u_{\mathrm{PD,cal}}$ of a 100 pC pulse of the calibrator is shown on the left side of Fig. 2.2, measured at the 50 Ω-input channel of an oscilloscope (see red line). With 50 Ω the

circuit is impedance matched and there are no reflections on the line. The measured 100 pC pulse has an amplitude of $\hat{u}_{\mathrm{PD,cal}} \approx 0.64\,\mathrm{V}$ and pulse width of $t_{\mathrm{FWHM}} \approx 8\,\mathrm{ns}$.

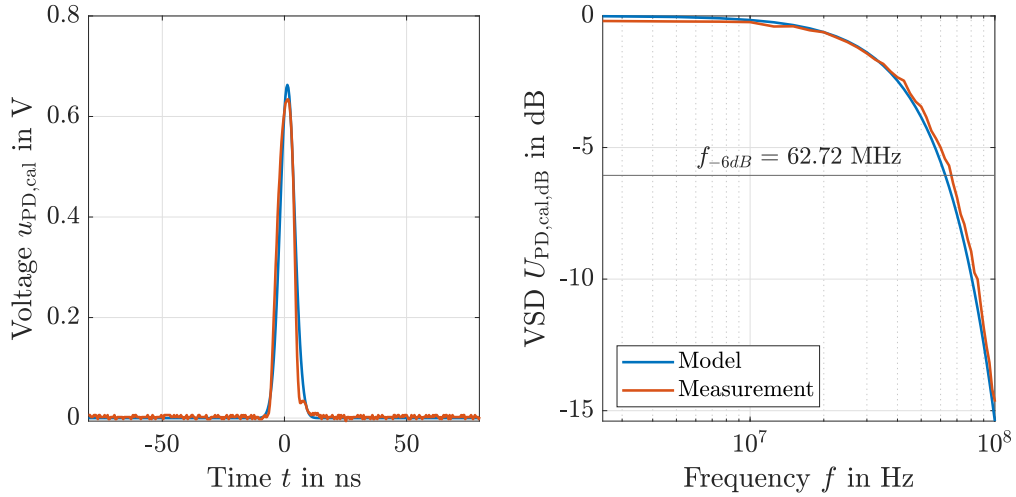

Figure 2.2: Measured output signal of the PD calibrator for a 100 pC pulse in the time and frequency domain.

The measured 100 pC calibrator pulse is also transformed into the frequency domain and its logarithmic VSD is calculated according to (1.1). The result $U_{\mathrm{PD,cal,dB}}(f)$ is shown on the right side of Fig. 2.2 (see red line). The -6 dB cut-off frequency or bandwidth of the PD pulse of the calibrator is $f_{-6\,\mathrm{dB}} \approx 62.72\,\mathrm{MHz}$.

In the time domain, a PD can be modeled by a Gaussian function. The mathematical description of a symmetric Gaussian function is [25], [26]:

$$u_{\mathrm{PD,mod}}(t) = \hat{u}_{\mathrm{PD}}\,\mathrm{e}^{-\frac{(t-t_0)^2}{2c^2}} \tag{2.1}$$

where $t_0 = 0\,\mathrm{s}$ is the position of the peak center and c describes the pulse width. The relationship between t_{FWHM} and c is:

$$c = \frac{t_{\mathrm{FWHM}}}{2\sqrt{2\ln(2)}} \approx 0.42466\,t_{\mathrm{FWHM}} \tag{2.2}$$

In the frequency domain, the mathematical description of the Gaussian function is [25], [26]:

$$U_{\mathrm{PD,mod}}(\omega) = \hat{u}_{\mathrm{PD}}\,c\,\sqrt{2\pi}\,\mathrm{e}^{-\frac{(c\,\omega)^2}{2}} \tag{2.3}$$

The result of (2.3) is again a VSD that can be converted to a logarithmic scale using (1.1).

To fit the Gaussian PD model of (2.1) to a specific PD pulse measurement, the values of the three free parameters $\hat{u}_{\mathrm{PD}}$, t_0 and c are determined by an optimization algorithm. For this purpose, the algorithm varies the free parameters until the sum of squared residuals between PD measurement and the Gaussian PD model is minimal.

The optimization algorithm was used to fit the Gaussian PD model to the measured 100 pC pulse of the calibrator. The result is also shown in Fig. 2.2 (see blue lines). A comparison of measurement and model shows that the Gaussian PD model reproduces the measurement with sufficient accuracy. The PD model can thus be used to simulate realistic PDs. It can be fitted to any symmetrical PD pulse using the optimization algorithm (PDs are always symmetrical at the time of ignition [25]; asymmetry results from dispersion [27]).

2.2 Transmission Line Model

PDs propagate from their point of origin via a transmission line to a measuring device. The following section shows how this process can be modeled and simulated. For this purpose, a transmission line model suitable for HF signals is derived. The model can thus be used to simulate the transmission of PDs or any other signals. In the remainder of the chapter, the transmission line model is used to simulate the propagation of PD pulses on power cables. However, it should be highlighted that the model can be applied to all transmission lines, e. g., overhead lines, gas-insulated lines, etc.

It has already been shown in Section 1.1 that the bandwidths of PD pulses are in the MHz range. The shortest wavelengths of such HF signals are usually much shorter than the length of the transmission lines (electrical length). For example, 3 MHz corresponds to a wavelength of $\lambda \approx 100\,\mathrm{m}$ and 30 MHz corresponds to a wavelength of $\lambda \approx 10\,\mathrm{m}$. Most transmission lines are much longer. The PD propagation process must therefore be described using transmission line theory. The model thus requires a solution of the telegrapher's equations.

However, most of today's publications on PD transmission have not considered transmission line theory, e. g., [28]–[31]. There are two publications [27], [32] that offer a solution of the telegrapher's equations, but both results are inconsistent, have shortcomings in the derivation of their solution, and are therefore not fully comprehensible. This work addresses these deficiencies and provides a comprehensible and validated transmission line model for the HF domain.

This section introduces the transmission line model and is organized as follows. Subsection 2.2.1 gives a short introduction to telegrapher's equations, before in Subsection 2.2.2 their general solution is provided. Subsection 2.2.3 defines the characteristic impedance

and reflection coefficient. Finally, in Subsection 2.2.4 a specific solution of the telegrapher's equations for the PD transmission problem is derived.

2.2.1 Derivation of the Telegrapher's Equations

At the beginning it should be mentioned that a large number of parameters will be introduced on the following pages. Namely, the primary line constants $R'(\omega)$, $L'(\omega)$, $C'(\omega)$, $G'(\omega)$ as well as the secondary line constants $\underline{Z}'(\omega)$, $\underline{Y}'(\omega)$, $\underline{\gamma}(\omega)$, $\alpha(\omega)$, $\beta(\omega)$, $\underline{Z}_\mathrm{c}(\omega)$ and $\underline{r}_\mathrm{z}(\omega)$. All of them are frequency dependent. However, to improve the readability of the text, the frequency dependency is not marked in the rest of the text.

It is assumed that the material and structure of the transmission line are homogeneous over its entire length. This assumption is close to reality for most transmission lines such as power cables or overhead lines. The equivalent circuit of such a transmission line can then be divided into infinitesimally small equal elements of length Δz, see Fig. 2.3. Each segment of this distributed-element model is then characterized as follows:

$$R' = \frac{\Delta R}{\Delta z} \text{ in } \frac{\Omega}{\mathrm{m}} \qquad L' = \frac{\Delta L}{\Delta z} \text{ in } \frac{\mathrm{H}}{\mathrm{m}} \tag{2.4}$$

$$C' = \frac{\Delta C}{\Delta z} \text{ in } \frac{\mathrm{F}}{\mathrm{m}} \qquad G' = \frac{\Delta G}{\Delta z} \text{ in } \frac{\mathrm{S}}{\mathrm{m}} \tag{2.5}$$

These four electrical parameters are called primary line constants. With their help, any conductive transmission line can be fully characterized. Contrary to their name, they are not constants, but frequency dependent $R'(\omega)$, $L'(\omega)$, $C'(\omega)$ and $G'(\omega)$.

The telegrapher's equations are derived from Fig. 2.3. The application of Kirchhoff's voltage law with $\Delta z \to 0$ leads to:

$$-\frac{\partial u(z,t)}{\partial z} = R' \cdot i(z,t) + L' \cdot \frac{\partial i(z,t)}{\partial t} \tag{2.6}$$

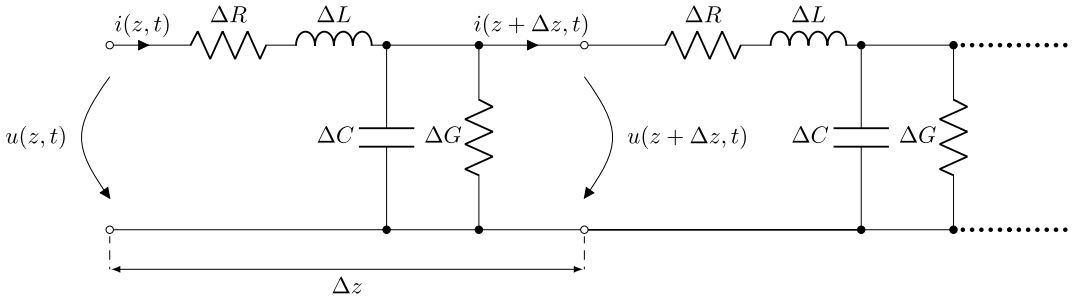

Figure 2.3: Distributed-element model of a transmission line.

The application of Kirchhoff's current law with $\Delta z \to 0$ leads to:

$$-\frac{\partial i(z,t)}{\partial z} = G' \cdot u(z,t) + C' \cdot \frac{\partial u(z,t)}{\partial t} \tag{2.7}$$

The two coupled linear partial differential equations (2.6) and (2.7) are the telegrapher's equations in the time domain. For a more detailed derivation see [33], [34].

If only steady-state sinusoidal signals are considered, further simplification can be achieved by transforming these equations into the frequency domain. Voltage and current signals are then represented as a superposition of many sinusoidal signals with different frequencies. Since all time information is lost in the frequency domain, this approach is not suitable for studying transient events. However, it can be used if only the transmission behavior of the line is to be studied.

The sine functions can be formulated in phasor notation with Root Mean Square (RMS) magnitudes as follows:

$$u(z,t) = \sqrt{2}\,U(z)\,\cos(\omega t + \varphi_\mathrm{U}) = \sqrt{2}\ \mathrm{Re}\left(\underline{U}(z)\ \mathrm{e}^{\mathrm{j}\omega t}\right) \tag{2.8}$$

$$i\,(z,t) = \sqrt{2}\ I(z)\,\cos(\omega t + \varphi_\mathrm{I}) = \sqrt{2}\ \mathrm{Re}\left(\underline{I}\,(z)\,\mathrm{e}^{\mathrm{j}\omega t}\right) \tag{2.9}$$

where $\underline{U}(z) = U(z)\,\mathrm{e}^{\mathrm{j}\varphi_\mathrm{U}}$ and $\underline{I}(z) = I(z)\,\mathrm{e}^{\mathrm{j}\varphi_\mathrm{I}}$. Transforming (2.6) and (2.7) into the frequency domain by substituting (2.8) and (2.9) then yields:

$$-\frac{\partial \underline{U}(z)}{\partial z} = (R' + \mathrm{j}\omega L')\ \underline{I}\,(z) = \underline{Z}'\,\underline{I}\,(z) \tag{2.10}$$

$$-\frac{\partial \underline{I}\,(z)}{\partial z} = (G' + \mathrm{j}\omega C')\,\underline{U}(z) = \underline{Y}'\,\underline{U}(z) \tag{2.11}$$

where $\underline{Z}'$ is the complex series impedance per unit length in $\frac{\Omega}{\mathrm{m}}$ and $\underline{Y}'$ is the complex shunt admittance per unit length in $\frac{\mathrm{S}}{\mathrm{m}}$. It should be kept in mind that series impedance and shunt admittance are frequency dependent.

The derivation of (2.10) and (2.11) with respect to z and subsequent mutual substitution lead to the telegrapher's equations in the frequency domain:

$$\frac{\partial^2 \underline{U}(z)}{\partial z^2} = \underline{Z}'\,\underline{Y}'\ \underline{U}(z) = \underline{\gamma}^2\,\underline{U}(z) \tag{2.12}$$

$$\frac{\partial^2 \underline{I}\,(z)}{\partial z^2} = \underline{Z}'\,\underline{Y}'\ \underline{I}\ (z) = \underline{\gamma}^2\,\underline{I}\,(z) \tag{2.13}$$

Two complex wave equations (2.12) and (2.13) are obtained, where $\underline{\gamma}$ is the propagation

constant of the transmission line. The two wave equations are now decoupled from each other. They describe the current and voltage distribution along a transmission line. The transmission behavior of the transmission line is characterized only by the propagation constant $\underline{\gamma}$, which can be split into the attenuation constant α in $\frac{\mathrm{Np}}{\mathrm{m}}$ and the phase constant β in $\frac{\mathrm{rad}}{\mathrm{m}}$:

$$\underline{\gamma} = \sqrt{\underline{Z}'\,\underline{Y}'} = \sqrt{(R' + \mathrm{j}\omega L')\,(G' + \mathrm{j}\omega C')} = \alpha + \mathrm{j}\beta \tag{2.14}$$

The conversion from neper to decibel is $1\,\mathrm{Np} \approx 8.686\,\mathrm{dB}$ [35], [36]. It should be kept in mind that the propagation constant, attenuation constant and phase constant are also all frequency dependent.

To calculate the propagation constant of a given transmission line according to (2.14), the primary line constants of that line have to be known. If a power cable is used as transmission line, its primary line constants are determined as described in Section 2.3.

2.2.2 General Solution of the Telegrapher's Equations

A general solution of the wave equations (2.12) and (2.13) can be given using the exponential approach:

$$\underline{U}(z) = \underline{U}_\mathrm{f}\,\mathrm{e}^{-\underline{\gamma}z} + \underline{U}_\mathrm{b}\,\mathrm{e}^{\underline{\gamma}z} \tag{2.15}$$

$$\underline{I}(z) = \underline{I}_\mathrm{f}\,\mathrm{e}^{-\underline{\gamma}z} + \underline{I}_\mathrm{b}\,\mathrm{e}^{\underline{\gamma}z} \tag{2.16}$$

Physically, this solution can be interpreted as the sum of a forward and a backward traveling wave. The constants $\underline{U}_\mathrm{f}$ and $\underline{U}_\mathrm{b}$ are the phasors of the forward and backward voltage wave in V. The constants $\underline{I}_\mathrm{f}$ and $\underline{I}_\mathrm{b}$ are the phasors of the forward and backward current wave in A. All four unknown parameters are determined by the boundary conditions of the problem to be solved [37], [38]. The boundary conditions that describe the specific problem of PD transmission on power cables are derived in Section 2.2.4.

2.2.3 Characteristic Impedance and Reflection Coefficient

In order to solve the wave equations in the next section, it is necessary to introduce two more fundamentals of transmission line theory. First, voltage and current waves of the general solution are related to each other via $\underline{Z}_\mathrm{c}$:

$$\underline{Z}_\mathrm{c} = \frac{\underline{U}_\mathrm{f}}{\underline{I}_\mathrm{f}} = -\frac{\underline{U}_\mathrm{b}}{\underline{I}_\mathrm{b}} = \sqrt{\frac{\underline{Z}'}{\underline{Y}'}} \tag{2.17}$$

where $\underline{Z}_\mathrm{c}$ is the characteristic impedance of the transmission line in Ω [39].

Second, backward and forward traveling waves are related to each other via $\underline{r}_\mathrm{z}$:

$$\frac{\underline{U}_\mathrm{b}\,\mathrm{e}^{\gamma z}}{\underline{U}_\mathrm{f}\,\mathrm{e}^{-\gamma z}} = \frac{\frac{\underline{U}(z)}{\underline{I}(z)} - \underline{Z}_\mathrm{c}}{\frac{\underline{U}(z)}{\underline{I}(z)} + \underline{Z}_\mathrm{c}} = \frac{\underline{Z}_\mathrm{z} - \underline{Z}_\mathrm{c}}{\underline{Z}_\mathrm{z} + \underline{Z}_\mathrm{c}} = \underline{r}_\mathrm{z} \tag{2.18}$$

where $\underline{r}_\mathrm{z}$ is the reflection coefficient at position z of the transmission line. The reflection coefficient depends on the impedance $\underline{Z}_\mathrm{z}$ at this point and indicates which portion of a forward traveling wave is reflected back into the transmission line [34]. Reflections occur only at discontinuities along the transmission line.

Now all the necessary equations have been derived and the telegrapher's equations can be solved for the PD transmission problem.

2.2.4 Specific Solution for the PD Transmission Problem

In order to obtain a specific solution of the general solution, some boundary conditions must be defined for the PD transmission problem. Fig. 2.4 shows the modeling concept. It consists of a transmission line of finite length l with arbitrary termination impedances $\underline{Z}_1$ and $\underline{Z}_2$ at both ends. A PD (or any other signal with HF spectrum) can occur at any point $0 \leq z_\mathrm{s} \leq l$ along the transmission line. At this point z_s, a PD source must be modeled.

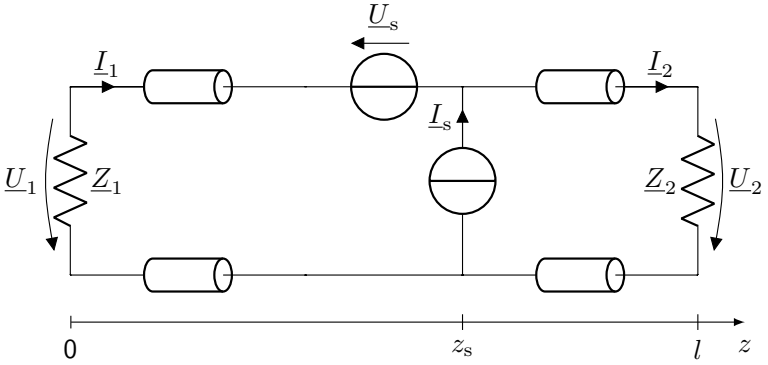

Figure 2.4: Modeling approach for the propagation of PD on a transmission line. The line is terminated at its ends with $\underline{Z}_1$ and $\underline{Z}_2$. The PD can occur at any point z_s along the length of the line l and is represented by a voltage $\underline{U}_\mathrm{s}$ and a current source $\underline{I}_\mathrm{s}$.

The PD source modeling is subject to the following considerations. In the previous Section 2.1, the voltage signal of a PD was measured directly at the input of an oscilloscope. It is also possible to measure the current of a PD pulse, e. g., with a current probe at the oscilloscope input. Accordingly, a PD can be modeled in the time domain

by a voltage pulse or by a current pulse. Both representations are equivalent. To enable both options also in the frequency domain, the model is equipped with a voltage $\underline{U}_\mathrm{s}$ and a current source $\underline{I}_\mathrm{s}$. Both sources are located at the PD origin point z_s.

One part of the transmission line is on the left of the PD $z < z_\mathrm{s}$ and the other part on the right $z > z_\mathrm{s}$. The general solution of the telegrapher's equation in the frequency domain (2.15) and (2.16) applies to both parts individually. Setting up the initial system of equations under further consideration of (2.17):

$$\left.\begin{aligned} \underline{U}_1(z) &= \underline{U}_{\mathrm{f},1}\,\mathrm{e}^{-\underline{\gamma}z} + \underline{U}_{\mathrm{b},1}\,\mathrm{e}^{\underline{\gamma}z} \\ \underline{I}_1(z) &= \frac{\underline{U}_{\mathrm{f},1}}{\underline{Z}_\mathrm{c}}\,\mathrm{e}^{-\underline{\gamma}z} - \frac{\underline{U}_{\mathrm{b},1}}{\underline{Z}_\mathrm{c}}\,\mathrm{e}^{\underline{\gamma}z} \end{aligned}\right\} z < z_\mathrm{s} \tag{2.19}$$

$$\left.\begin{aligned} \underline{U}_2(z) &= \underline{U}_{\mathrm{f},2}\,\mathrm{e}^{-\underline{\gamma}z} + \underline{U}_{\mathrm{b},2}\,\mathrm{e}^{\underline{\gamma}z} \\ \underline{I}_2(z) &= \frac{\underline{U}_{\mathrm{f},2}}{\underline{Z}_\mathrm{c}}\,\mathrm{e}^{-\underline{\gamma}z} - \frac{\underline{U}_{\mathrm{b},2}}{\underline{Z}_\mathrm{c}}\,\mathrm{e}^{\underline{\gamma}z} \end{aligned}\right\} z > z_\mathrm{s} \tag{2.20}$$

Four boundary conditions are required to solve this initial equation system (four unknown phasors). Two of them result from the termination impedances at the ends of the transmission line:

$$\underline{U}_1(0) = -\underline{Z}_1\,\underline{I}_1(0) \tag{2.21}$$

$$\underline{U}_2(l) = \underline{Z}_2\,\underline{I}_2(l) \tag{2.22}$$

The other two are obtained by the transition condition at z_s:

$$\underline{I}_2\,(z_\mathrm{s}) = \underline{I}_1(z_\mathrm{s}) + \underline{I}_\mathrm{s} \tag{2.23}$$

$$\underline{U}_2(z_\mathrm{s}) = \underline{U}_1(z_\mathrm{s}) + \underline{U}_\mathrm{s} \tag{2.24}$$

Now the initial system of equations can be solved for the given boundary conditions. At first a detailed formulation of the four boundary conditions with (2.19) and (2.20) can be given:

$$\underline{U}_{\mathrm{f},1} + \underline{U}_{\mathrm{b},1} = -\underline{Z}_1\left(\frac{\underline{U}_{\mathrm{f},1}}{\underline{Z}_\mathrm{c}} - \frac{\underline{U}_{\mathrm{b},1}}{\underline{Z}_\mathrm{c}}\right) \tag{2.25}$$

$$\underline{U}_{\mathrm{f},2}\,\mathrm{e}^{-\underline{\gamma}l} + \underline{U}_{\mathrm{b},2}\,\mathrm{e}^{\underline{\gamma}l} = \underline{Z}_2\left(\frac{\underline{U}_{\mathrm{f},2}}{\underline{Z}_\mathrm{c}}\,\mathrm{e}^{-\underline{\gamma}l} - \frac{\underline{U}_{\mathrm{b},2}}{\underline{Z}_\mathrm{c}}\,\mathrm{e}^{\underline{\gamma}l}\right) \tag{2.26}$$

$$\frac{\underline{U}_{\mathrm{f},1}}{\underline{Z}_\mathrm{c}}\,\mathrm{e}^{-\underline{\gamma}z_\mathrm{s}} - \frac{\underline{U}_{\mathrm{b},1}}{\underline{Z}_\mathrm{c}}\,\mathrm{e}^{\underline{\gamma}z_\mathrm{s}} + \underline{I}_\mathrm{s} = \frac{\underline{U}_{\mathrm{f},2}}{\underline{Z}_\mathrm{c}}\,\mathrm{e}^{-\underline{\gamma}z_\mathrm{s}} - \frac{\underline{U}_{\mathrm{b},2}}{\underline{Z}_\mathrm{c}}\,\mathrm{e}^{\underline{\gamma}z_\mathrm{s}} \tag{2.27}$$

$$\underline{U}_{\mathrm{f},1}\,\mathrm{e}^{-\underline{\gamma}z_\mathrm{s}} + \underline{U}_{\mathrm{b},1}\,\mathrm{e}^{\underline{\gamma}z_\mathrm{s}} + \underline{U}_\mathrm{s} = \underline{U}_{\mathrm{f},2}\,\mathrm{e}^{-\underline{\gamma}z_\mathrm{s}} + \underline{U}_{\mathrm{b},2}\,\mathrm{e}^{\underline{\gamma}z_\mathrm{s}} \tag{2.28}$$

Solving (2.25) for the forward voltage phasor $\underline{U}_{\mathrm{f},1}$ of the left section of the transmission line:

$$\underline{U}_{\mathrm{f},1} = \underline{U}_{\mathrm{b},1} \left(\frac{\underline{Z}_1 - \underline{Z}_\mathrm{c}}{\underline{Z}_1 + \underline{Z}_\mathrm{c}} \right) = \underline{U}_{\mathrm{b},1}\, \underline{r}_1 \tag{2.29}$$

Solving (2.26) for the backward voltage phasor $\underline{U}_{\mathrm{b},2}$ of the right section of the transmission line:

$$\underline{U}_{\mathrm{b},2} = \underline{U}_{\mathrm{f},2} \left(\frac{\underline{Z}_2 - \underline{Z}_\mathrm{c}}{\underline{Z}_2 + \underline{Z}_\mathrm{c}} \right) \mathrm{e}^{-2\underline{\gamma} l} = \underline{U}_{\mathrm{f},2}\, \underline{r}_2\, \mathrm{e}^{-2\underline{\gamma} l} \tag{2.30}$$

Solving (2.27) for the backward voltage phasor $\underline{U}_{\mathrm{b},1}$ of the left section of the transmission line:

$$\underline{U}_{\mathrm{b},1} = \underline{U}_{\mathrm{f},1}\, \mathrm{e}^{-2\underline{\gamma} z_\mathrm{s}} - \underline{U}_{\mathrm{f},2}\, \mathrm{e}^{-2\underline{\gamma} z_\mathrm{s}} + \underline{U}_{\mathrm{b},2} + \underline{I}_\mathrm{s}\, \underline{Z}_\mathrm{c}\, \mathrm{e}^{-\underline{\gamma} z_\mathrm{s}} \tag{2.31}$$

Solving (2.28) for the forward voltage phasor $\underline{U}_{\mathrm{f},2}$ of the right section of the transmission line:

$$\underline{U}_{\mathrm{f},2} = \underline{U}_{\mathrm{f},1} + \underline{U}_{\mathrm{b},1}\, \mathrm{e}^{2\underline{\gamma} z_\mathrm{s}} - \underline{U}_{\mathrm{b},2}\, \mathrm{e}^{2\underline{\gamma} z_\mathrm{s}} + \underline{U}_\mathrm{s}\, \mathrm{e}^{\underline{\gamma} z_\mathrm{s}} \tag{2.32}$$

Substituting (2.29) and (2.30) into (2.31):

$$\underline{U}_{\mathrm{b},1} = \frac{\underline{U}_{\mathrm{f},2}\, (\underline{r}_2\, \mathrm{e}^{-2\underline{\gamma} l} - \mathrm{e}^{-2\underline{\gamma} z_\mathrm{s}}) + \underline{I}_\mathrm{s}\, \underline{Z}_\mathrm{c}\, \mathrm{e}^{-\underline{\gamma} z_\mathrm{s}}}{1 - \underline{r}_1\, \mathrm{e}^{-2\underline{\gamma} z_\mathrm{s}}} \tag{2.33}$$

Substituting (2.29) and (2.30) into (2.32):

$$\underline{U}_{\mathrm{f},2} = \frac{\underline{U}_{\mathrm{b},1}\, (\underline{r}_1 + \mathrm{e}^{2\underline{\gamma} z_\mathrm{s}}) + \underline{U}_\mathrm{s}\, \mathrm{e}^{\underline{\gamma} z_\mathrm{s}}}{1 + \underline{r}_2\, \mathrm{e}^{-2\underline{\gamma} l}\, \mathrm{e}^{2\underline{\gamma} z_\mathrm{s}}} \tag{2.34}$$

Now substituting (2.33) into (2.34) and again solve for $\underline{U}_{\mathrm{f},2}$:

$$\underline{U}_{\mathrm{f},2} = \frac{1}{2}\, \frac{(\underline{U}_\mathrm{s} + \underline{I}_\mathrm{s}\, \underline{Z}_\mathrm{c})\, \mathrm{e}^{\underline{\gamma} z_\mathrm{s}} - (\underline{U}_\mathrm{s} - \underline{I}_\mathrm{s}\, \underline{Z}_\mathrm{c})\, \underline{r}_1\, \mathrm{e}^{-\underline{\gamma} z_\mathrm{s}}}{1 - \underline{r}_1\, \underline{r}_2\, \mathrm{e}^{-2\underline{\gamma} l}} \tag{2.35}$$

And finally substituting (2.34) into (2.33) and solve for $\underline{U}_{\mathrm{b},1}$:

$$\underline{U}_{\mathrm{b},1} = \frac{\mathrm{e}^{-\underline{\gamma} l}}{2}\, \frac{(\underline{U}_\mathrm{s} + \underline{I}_\mathrm{s}\, \underline{Z}_\mathrm{c})\, \underline{r}_2\, \mathrm{e}^{-\underline{\gamma}(l - z_\mathrm{s})} - (\underline{U}_\mathrm{s} - \underline{I}_\mathrm{s}\, \underline{Z}_\mathrm{c})\, \mathrm{e}^{\underline{\gamma}(l - z_\mathrm{s})}}{1 - \underline{r}_1\, \underline{r}_2\, \mathrm{e}^{-2\underline{\gamma} l}} \tag{2.36}$$

The four initially unknown phasors of the equation system are now known for the given boundary conditions. Thus, (2.29), (2.30), (2.35) and (2.36) can now be used to write

the final solution of the initial system of equations. For $z < z_\mathrm{s}$ yields:

$$\begin{aligned}\underline{U}_1(z) = \frac{\mathrm{e}^{-\underline{\gamma} l}(\mathrm{e}^{\underline{\gamma} z} + \underline{r}_1 \mathrm{e}^{-\underline{\gamma} z})}{2\left(1 - \underline{r}_1 \underline{r}_2 \mathrm{e}^{-2\underline{\gamma} l}\right)} \Big[\left(\underline{r}_2 \mathrm{e}^{-\underline{\gamma}(l-z_\mathrm{s})} - \mathrm{e}^{\underline{\gamma}(l-z_\mathrm{s})}\right) \underline{U}_\mathrm{s} \\ + \left(\underline{r}_2 \mathrm{e}^{-\underline{\gamma}(l-z_\mathrm{s})} + \mathrm{e}^{\gamma(l-z_\mathrm{s})}\right) \underline{I}_\mathrm{s} \underline{Z}_\mathrm{c}\Big] \\ \underline{I}_1(z) = \frac{\mathrm{e}^{-\underline{\gamma} l}(-\mathrm{e}^{\underline{\gamma} z} + \underline{r}_1 \mathrm{e}^{-\underline{\gamma} z})}{2\left(\underline{Z}_\mathrm{c}(1 - \underline{r}_1 \underline{r}_2 \mathrm{e}^{-2\underline{\gamma} l})\right)} \Big[\left(\underline{r}_2 \mathrm{e}^{-\underline{\gamma}(l-z_\mathrm{s})} - \mathrm{e}^{\underline{\gamma}(l-z_\mathrm{s})}\right) \underline{U}_\mathrm{s} \\ + \left(\underline{r}_2 \mathrm{e}^{-\underline{\gamma}(l-z_\mathrm{s})} + \mathrm{e}^{\underline{\gamma}(l-z_\mathrm{s})}\right) \underline{I}_\mathrm{s} \underline{Z}_\mathrm{c}\Big]\end{aligned} \tag{2.37}$$

And finally, for the right-side $z > z_\mathrm{s}$ yields:

$$\begin{aligned}\underline{U}_2(z) = \frac{\mathrm{e}^{-\underline{\gamma} l}(\mathrm{e}^{\underline{\gamma}(l-z)} + \underline{r}_2 \mathrm{e}^{-\underline{\gamma}(l-z)})}{2\left(1 - \underline{r}_1 \underline{r}_2 \mathrm{e}^{-2\underline{\gamma} l}\right)} \Big[\left(\mathrm{e}^{\underline{\gamma} z_\mathrm{s}} - \underline{r}_1 \mathrm{e}^{-\underline{\gamma} z_\mathrm{s}}\right) \underline{U}_\mathrm{s} \\ + \left(\mathrm{e}^{\underline{\gamma} z_\mathrm{s}} + \underline{r}_1 \mathrm{e}^{-\gamma z_\mathrm{s}}\right) \underline{I}_\mathrm{s} \underline{Z}_\mathrm{c}\Big] \\ \underline{I}_2(z) = \frac{\mathrm{e}^{-\underline{\gamma} l}(\mathrm{e}^{\underline{\gamma}(l-z)} - \underline{r}_2 \mathrm{e}^{-\underline{\gamma}(l-z)})}{2\left(\underline{Z}_\mathrm{c}(1 - \underline{r}_1 \underline{r}_2 \mathrm{e}^{-2\underline{\gamma} l})\right)} \Big[\left(\mathrm{e}^{\underline{\gamma} z_\mathrm{s}} - \underline{r}_1 \mathrm{e}^{-\underline{\gamma} z_\mathrm{s}}\right) \underline{U}_\mathrm{s} \\ + \left(\mathrm{e}^{\underline{\gamma} z_\mathrm{s}} + \underline{r}_1 \mathrm{e}^{-\underline{\gamma} z_\mathrm{s}}\right) \underline{I}_\mathrm{s} \underline{Z}_\mathrm{c}\Big]\end{aligned} \tag{2.38}$$

The final solution (2.37) and (2.38) describes the voltage and current distribution along the transmission line. For the calculation, the secondary line constants $\underline{\gamma}$, $\underline{Z}_\mathrm{c}$, $\underline{r}_1$, $\underline{r}_2$ of the transmission line must be known. The next section shows how to calculate the secondary line constants of a power cable.

If the secondary line constants are known, the solution depends only on the arbitrary source signal $\underline{U}_\mathrm{s}$ or $\underline{I}_\mathrm{s}$. Only one of the two sources is used at a time and the other is set to zero. This provides more flexibility for the end user. In the remainder of the dissertation mainly the voltage source is used.

2.3 Calculation of the Propagation Constant of a Power Cable

In order to use the developed transmission line model to simulate the propagation of PD, the propagation constant $\underline{\gamma}$ of the underlying transmission line must first be known. Therefore, in this section, the calculation of $\underline{\gamma}$ for a power cable is derived step by step.

Despite the many publications on this topic, e. g., [27]–[32], a purely analytical, comprehensive and reproducible method for calculating the propagation constant of

a power cable is still missing. Thus, this work provides such a method. The shown calculation of the propagation constant of a power cable is mainly based on the works of [26], [40], [41] and combines and extends their results. The frequency dependency of all primary line constants is considered, which cannot be neglected in the HF range.

At the end of the section, $\underline{\gamma}$ is calculated for an exemplary power cable and validated by measurements. The exemplary power cable used for the validation measurements is a modern single-phase cable with XLPE insulation. The rated voltage is 20 kV, so it is an MV power cable. However, the validation measurement is representative of most XLPE cables, as their structure is always similar. Therefore, the derived method for calculating $\underline{\gamma}$ should be applicable to XLPE cables of all voltage levels.

Subsection 2.3.1 gives an overview of the structure of modern power cables. Then, in Subsection 2.3.2 to Subsection 2.3.5, the calculation of the four primary line constants of a power cable are described one after the other. Subsequently, in Subsection 2.3.6, the secondary line constants of the power cable are calculated. Finally, in Subsection 2.3.7, all calculations are derived against measurements.

2.3.1 Structure of a Power Cable

As shown in Fig. 2.5, power cables typically consist of an inner conductor with radius r_1, an inner semiconducting layer or conductor screen of thickness d_{sc1}, a dielectric insulation layer of thickness d_{ins}, an outer semiconducting layer or insulation screen of thickness d_{sc2}, an outer conductor with inner radius $r_2 = r_1 + d_{\mathrm{sc1}} + d_{\mathrm{ins}} + d_{\mathrm{sc2}}$ and an outer protective sheath. In addition, power cables may have an additional thin, water-swellable semiconducting tape layer between insulation screen and outer conductor.

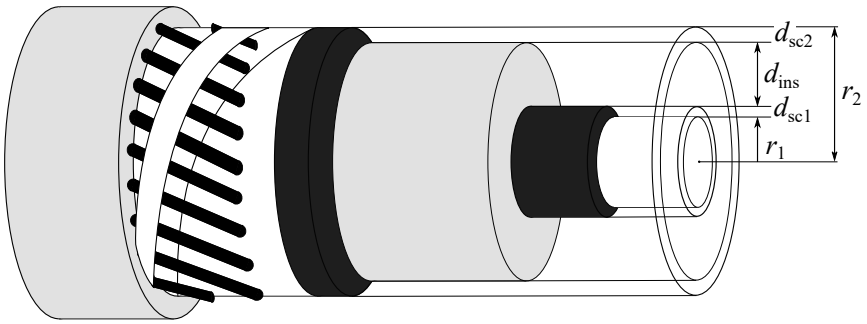

Figure 2.5: Cross-section of a single-phase XLPE power cable. The cable structure is coaxial and consists of several layers. From the cable axis outwards, these are: inner conductor with radius r_1, inner semiconducting layer of thickness d_{sc1}, dielectric insulating layer of thickness d_{ins}, outer semiconducting layer of thickness d_{sc2}, outer conductor with inner radius r_2.

However, such a layer is not included in the example MV cable. The semiconducting layers are used to provide a smooth interface between the conductors and the insulating XLPE layer. This serves to homogenize the electric field and avoid highly stressed areas due to small surface imperfections at the interfaces of the conductors.

To calculate the propagation constant $\underline{\gamma}$ of a power cable, its primary line constants R', L', C' and G' must first be determined. It is assumed that the cable geometry is constant over the entire length. To simplify the calculations, the inner conductor is considered as a solid cylinder and the outer conductor as a solid hollow cylinder. It is also assumed that the cable is straight over its entire length. This implies a homogeneous field distribution and allows the calculation of the primary line constants [26]. The last assumption should be close to reality, since the maximum bending radius of a power cable is quite large.

2.3.2 Conductor Resistance

The resistance per unit length R' of a copper conductor at DC is calculated as follows:

$$R' = \frac{1}{\sigma_{\mathrm{co}} A} \tag{2.39}$$

where $\sigma_{\mathrm{co}} = 58.14 \cdot 10^6 \, \frac{\mathrm{S}}{\mathrm{m}}$ is the electrical conductivity of the copper conductor and A is its cross-section in m^2. The resistance increases with frequency f due to the skin effect (proximity effect is negligible compared to the skin effect). The higher the frequency, the more current flows near the conductor surface. The thickness of this conductive layer is the skin depth δ in m and can be calculated for metallic conductors according to [42]:

$$\delta(\omega) = \sqrt{\frac{2}{\sigma_{\mathrm{co}} \omega \mu_0 \mu_{\mathrm{co}}}} \tag{2.40}$$

where $\mu_0 \approx 1.25664 \cdot 10^{-6} \, \frac{\mathrm{Vs}}{\mathrm{Am}}$ is the vacuum permeability, $\mu_{\mathrm{co}} = 1 - 6.4 \cdot 10^{-6} \approx 1$ is the relative permeability of copper and $\omega = 2\pi f$ is the angular frequency in $\frac{\mathrm{rad}}{\mathrm{s}}$. The skin depth $\delta(\omega)$ indicates the depth, at which the current density $\boldsymbol{J}$ inside of the conductor has decreased to $\frac{1}{\mathrm{e}}$ of its amplitude. In the MHz range, the skin depth for copper is only a few micrometers thick. Thus, the effective cross-section of the conductor for HF signals reduces to about $A_{\mathrm{hf}}(\omega) \approx 2\pi r \delta(\omega)$. Then the conductor resistance can be calculated as follows [26]:

$$R'(\omega) = \frac{1}{\sigma_{\mathrm{co}} A_{\mathrm{hf}}(\omega)} \approx \frac{1}{\sigma_{\mathrm{co}} 2\pi r \delta(\omega)} = \sqrt{\frac{\omega \mu_0 \mu_{\mathrm{co}}}{2\sigma_{\mathrm{co}}}} \frac{1}{2\pi r} \tag{2.41}$$

The total resistance of a power cable is the sum of the resistances of the inner and outer conductor:

$$R'(\omega) = \sqrt{\frac{\omega \mu_0 \mu_{co}}{2\sigma_{co}}} \frac{1}{2\pi} \left(\frac{1}{r_1} + \frac{1}{r_2} \right) \tag{2.42}$$

2.3.3 Conductor Inductance

HF currents generate magnetic fields inside and outside the cable conductors. These magnetic fields change over time and induce an opposite voltage back into the conductors. This behavior is described by the conductor inductance per unit length L'. The influence of the magnetic fields on the conductors themselves, the so-called inner inductance L'_i, decreases with frequency due to the skin effect. Therefore, the inner inductance is negligible at frequencies > 10 kHz. Only the influence of the magnetic field between the conductors, the outer inductance L'_{out}, is relevant for calculating the total inductance of the power cable in the HF range [26]:

$$L' \approx L'_{out} = \frac{\mu_0 \mu_{co}}{2\pi} \ln \frac{r_2}{r_1} \tag{2.43}$$

2.3.4 Insulator Capacitance

The elements R' and L' describe the behavior of the conductors and C' and G' that of the dielectric material between the conductors. This dielectric consists of the main insulation layer and thin semiconducting layers on each side. Each of these layers has a frequency dependent capacitance per unit length $C'(\omega)$.

In general, the capacity of a coaxial cable layer can be calculated as follows [43], [44]:

$$\underline{C}'(\omega) = \frac{2\pi \varepsilon_0 \underline{\varepsilon}(\omega)}{\ln\left(\frac{r_2}{r_1}\right)} \tag{2.44}$$

where $\varepsilon_0 \approx 8.85418 \cdot 10^{-12} \frac{\mathrm{As}}{\mathrm{Vm}}$ is the vacuum permittivity and $\underline{\varepsilon}(\omega) = \varepsilon'(\omega) + \mathrm{j}\varepsilon''(\omega)$ is the complex permittivity of the dielectric layer. This permittivity describes the polarizability of the dielectric and is frequency dependent.

The permittivity of the XLPE insulator layer can be assumed to be constant in the HF range $\underline{\varepsilon}_{ins} = 2.26 + \mathrm{j} \cdot 10^{-3}$ [40], [41]. The permittivity of the semiconducting layers is usually not known from the datasheet of the power cable used. In [41], [45], researchers

measured the permittivity of each layer of a single-phase XLPE power cable. The authors have fitted the following complex permittivity model to their measurements:

$$\underline{\varepsilon}(\omega) = \frac{F_1}{1 + (\mathrm{j}\omega\tau_1)^{(1-\zeta_1)}} + \frac{F_2}{1 + (\mathrm{j}\omega\tau_2)^{(1-\zeta_2)}} + \frac{\sigma_{\mathrm{DC}}}{\mathrm{j}\omega\varepsilon_0} + \varepsilon_\infty \tag{2.45}$$

A detailed description of this model and the measurement method can be found in the referenced articles. The various parameters of the permittivity model are summarized in Table 2.1, separated by conductor screen and insulator screen. If necessary, the parameters of the optional water-swellable semiconducting tape layer are also added. With the values shown in Table 2.1 and (2.45) the permittivity of the two semiconducting layers are calculated.

Table 2.1: Parameters of the Permittivity Model of the Semiconducting Cable Layers.

Parameter	Conductor Screen	Insulator Screen	Tape Layer
F_1	105	95	160
F_2	50	90	48
ζ_1	0.5	0.3	0.5
ζ_2	0.3	0.5	0.7
τ_1	300 ns	100 ns	800 ns
τ_2	0.68 ns	4 ns	15 ns
ε_∞	4	2	1
σ_{DC}	0.15 $\frac{\mathrm{mS}}{\mathrm{m}}$	2.7 $\frac{\mathrm{mS}}{\mathrm{m}}$	32 $\frac{\mathrm{mS}}{\mathrm{m}}$

Then, the capacitance of each layer can be calculated according to (2.44):

$$\underline{C}'_{\mathrm{sc1}}(\omega) = \frac{2\pi\varepsilon_0\underline{\varepsilon}_{\mathrm{sc1}}(\omega)}{\ln\left(\frac{r_1+d_{\mathrm{sc1}}}{r_1}\right)} \tag{2.46}$$

$$\underline{C}'_{\mathrm{ins}} = \frac{2\pi\varepsilon_0\underline{\varepsilon}_{\mathrm{ins}}}{\ln\left(\frac{r_1+d_{\mathrm{sc1}}+d_{\mathrm{ins}}}{r_1+d_{\mathrm{sc1}}}\right)} \tag{2.47}$$

$$\underline{C}'_{\mathrm{sc2}}(\omega) = \frac{2\pi\varepsilon_0\underline{\varepsilon}_{\mathrm{sc2}}(\omega)}{\ln\left(\frac{r_1+d_{\mathrm{sc1}}+d_{\mathrm{ins}}+d_{\mathrm{sc2}}}{r_1+d_{\mathrm{sc1}}+d_{\mathrm{ins}}}\right)} \tag{2.48}$$

The total insulator capacitance of a power cable results from all individual capacities in series:

$$\underline{C}'(\omega) = \frac{1}{\frac{1}{\underline{C}'_{\mathrm{sc1}}(\omega)} + \frac{1}{\underline{C}'_{\mathrm{ins}}} + \frac{1}{\underline{C}'_{\mathrm{sc2}}(\omega)}} \tag{2.49}$$

If necessary, the capacitance of a possible water-swellable semiconducting tape layer is calculated and added in the same way.

2.3.5 Insulator Conductance

In XLPE cables, the influence of the insulator conductance per unit length G' is small compared to the dielectric losses due to polarization caused by $\underline{C}'$. The specific conductivity of the XLPE insulation material σ_{ins} is close to zero. The conductivities of the semiconducting layers are already considered in the used permittivity model (2.45). The XLPE conductance can therefore be neglected or, provided σ_{ins} is known, calculated as follows [44]:

$$G' = \frac{2\pi\sigma_{\mathrm{ins}}}{\ln\left(\frac{r_1+d_{\mathrm{sc1}}+d_{\mathrm{ins}}+d_{\mathrm{sc2}}}{r_1}\right)} \tag{2.50}$$

2.3.6 Secondary Line Constants

Now all primary line constants of the power cable are determined and thus its physical behavior is completely described. Next, the corresponding secondary line constants can be calculated. First the complex series impedance of the transmission line can be calculated:

$$\underline{Z}'(\omega) = R' + \mathrm{j}\omega L'(\omega) \tag{2.51}$$

Second, the complex shunt admittance of the transmission line can be calculated as follows:

$$\underline{Y}'(\omega) = G' + \mathrm{j}\omega\underline{C}'(\omega) \tag{2.52}$$

Finally, the propagation constant $\underline{\gamma}(\omega)$ of the power cable can be calculated according to (2.14). In addition, the characteristic impedance $\underline{Z}_{\mathrm{c}}(\omega)$ of the transmission line can be calculated according to (2.17).

2.3.7 Validation of the Calculated Propagation Constant

To validate the calculation method shown in Subsection 2.3.2 to Subsection 2.3.6, the propagation constant $\underline{\gamma}$ is calculated for an exemplary power cable and validated against measurements. The rated voltage of the example cable is 20 kV, so it is an MV power cable. The cable type is N2XS2Y from Suedkabel GmbH, a modern single-phase XLPE-insulated power cable. Some relevant parameters of this cable type are listed in Table 2.2. The piece of cable used is $l = 10\,\mathrm{m}$ long. It should be mentioned that the cable length has no influence on the calculation of $\underline{\gamma}$, as it depends only on the cable geometry and material.

Table 2.2: Parameters of the XLPE Power Cable Used.

Parameter	Value
conductor material	copper
rated voltage U_r	20 kV
inner conductor cross-section	50 mm^2
outer conductor cross-section	16 mm^2
r_1	4 mm
d_{sc1}	0.3 mm
d_{ins}	5.5 mm
d_{sc2}	0.6 mm
r_2	10.4 mm

For validation, the propagation constant γ of the exemplary power cable is also measured with a vector network analyzer (VNA). The measurement setup can be seen in Fig. 2.6a. With the help of a VNA, the scattering ($\boldsymbol{S}$) parameters of any linear electrical network can be measured (each transmission line can be interpreted as a linear two-port network). The measuring device used is a VNA of the type *DG8SAQ VNWA 3E* from the manufacturer SDR-Kits. This device is used to measure the $\boldsymbol{S}$-parameters of the exemplary power cable with a frequency sweep from 0.1 to 250 MHz.

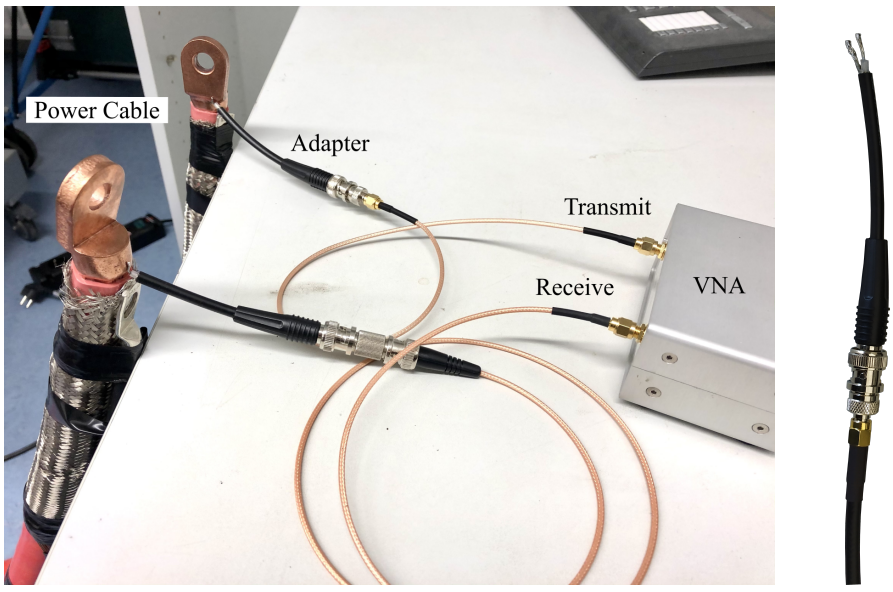

(a) **(b)**

Figure 2.6: Left: Measurement setup for measuring the propagation constant of a power cable with a VNA. Two adapters are used to connect the inner conductor and shielding of both ends of the power cable to the SMA ports of the VNA.
Right: Detailed view of the adapter needed to connect the power cable to the VNA.

To measure the propagation constant $\underline{\gamma}$ of the power cable, both of its ends must be connected to the VNA, as shown in Fig. 2.6a. So one end of the power cable is connected to the transmit output of the VNA and the other to the receive input. The connections are made with shielded coaxial cables of SMA type. To connect the SMA cables to the much larger power cable, adapters are required, which are shown in detail in Fig. 2.6b. The adapters connect the inner and outer conductor of the SMA cable with those of the power cable. This is done by cutting the coaxial cable of the adapter and partially removing the protective jacket and insulation so that its inner conductor and shielding are exposed and can be separated. The separated ends can now be soldered directly to the inner conductor and shielding of the power cable. Care must be taken to keep the unshielded portion of the adapters as short as possible to avoid unwanted parasitic inductance in the network.

Before the measurements, the VNA must first be properly calibrated. Calibration ensures that the measurement setup (coaxial cables, adapters, etc.) does not influence the actual measurement of the power cable. Therefore, a so-called SOLT-calibration is performed, which consists of four individual calibration measurements named Short, Open, Load, and Through. The calibration scheme is shown in Fig. 2.7.

Figure 2.7: Before the VNA can be used, it must be calibrated. During calibration, the power cable is not connected to the adapters. The figure shows the calibration scheme using the adapters.

For calibration, all SMA cables and adapters are connected to the VNA inputs (Port 1, Port 2), but without the power cable in between. For Short calibration, both ends of the adapter connected to the transmit port are soldered together. For Open calibration, both ends of the adapter connected to the transmit port are kept in an open state. For Load calibration, a 50 Ω SMD resistor is soldered between the ends of the adapter that is connected to the transmit port. For Through calibration, the ends of both adapters are soldered together so that the transmit and receive ports of the VNA are connected.

At each of the four steps, the VNA performs a calibration measurement with a frequency sweep from 0.1 to 250 MHz and stores the results in the VNA software. The calibration data are then used by the software to eliminate any interference caused by the measurement setup, i. e., from the SMA cables and adapters, so that they do not affect the actual measurement. After calibration, the power cable is placed between the adapters as shown in Fig. 2.6a and the measurement of its $\boldsymbol{S}$-parameters can begin.

The relationship between the measured $\boldsymbol{S}$-parameters and the propagation constant $\underline{\gamma}$ of a transmission line is [36], [46]:

$$\underline{\gamma}(\omega) = \frac{1}{l} \cosh^{-1}\left(\frac{1 - \underline{S}_{11}^2(\omega) + \underline{S}_{21}^2(\omega)}{2\underline{S}_{21}(\omega)}\right) \tag{2.53}$$

Fig. 2.8 compares the calculated and measured propagation constant $\underline{\gamma}$ of the exemplary power cable, separated into its real part α and imaginary part β. The attenuation constant is converted to $\frac{\mathrm{dB}}{\mathrm{m}}$, see the comment to (2.14) on page 14. Calculation and measurement of $\underline{\gamma}$ are very similar.

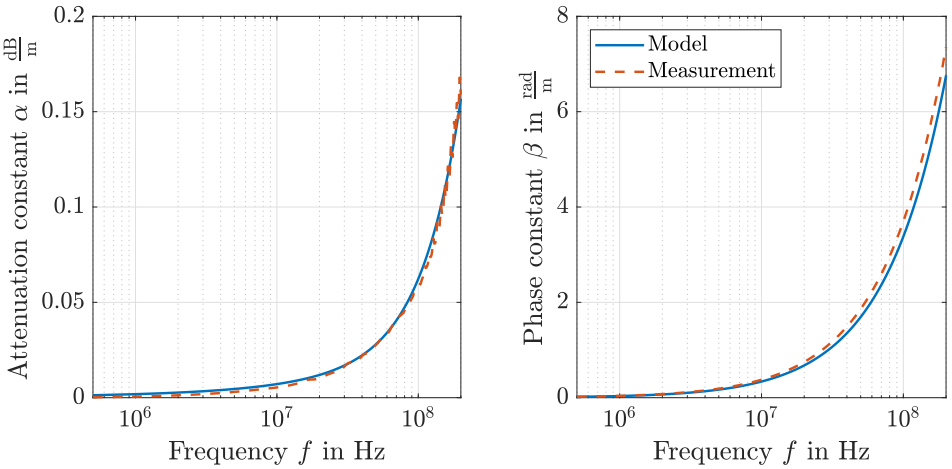

Figure 2.8: Comparison of the calculated and measured propagation constant $\underline{\gamma}$ of the exemplary power cable. Left: its real part, the attenuation constant α. Right: its imaginary part, the phase constant β.

It can be concluded that the propagation constant of the exemplary power cable is calculated correctly. Thus, the calculation method presented in this section is valid and can be used to calculate the propagation constant $\underline{\gamma}$ of any power cable, provided it has the same structure as shown in Fig. 2.5 on page 19. Since most of today's single-phase MV and HV power cables are of that structure, the method presented should cover almost all modern XLPE power cables.

2.4 Quick Guide for Using the Transmission Line Model

To summarize briefly: In the first Section 2.1 of this chapter it was described how PD pulses are modeled in the time and frequency domain. Section 2.2 then showed how to simulate the propagation of such PD signals on a transmission line. To use the derived transmission line model, only the propagation constant $\underline{\gamma}$ of the underlying transmission line needs to be known. Therefore, Section 2.3 showed how to calculate the propagation constant of power cables. At this point, the modeling is finished and everything needed to simulate the propagation of PD pulses on power cables has been derived. This section briefly explains how to bring everything together and use the transmission line model for simulations before validating it in the next Section 2.5.

To use the transmission line model, first the propagation constant $\underline{\gamma}$ and the characteristic impedance $\underline{Z}_\mathrm{c}$ of the underlying transmission line are calculated according to (2.14) and (2.17). Then, the reflection coefficients $\underline{r}_1$ and $\underline{r}_2$ are calculated based on the termination impedances $\underline{Z}_1$ and $\underline{Z}_2$ at both ends of the line according to (2.18).

Next, the initial PD signal must be specified, i. e., the voltage or current signal of the initial PD is required (or from any other HF signal). For the simulations in the following section, the measured 100 pC voltage pulse of the PD calibrator from Fig. 2.2 on page 10 is used. For this, $u_\mathrm{PD,cal}$ is measured with an oscilloscope as described in Section 2.1. Then, the Gaussian PD model $u_\mathrm{PD,mod}$ of (2.1) is fitted to this measurement using the described least squares algorithm. Afterwards $U_\mathrm{PD,mod}$ is calculated according to (2.3) and used as input $\underline{U}_\mathrm{s}$ of the transmission line model, while $\underline{I}_\mathrm{s} = 0$. If the initial PD signal is measured with a current probe instead, proceed the same way, while $\underline{U}_\mathrm{s} = 0$.

Now, (2.37) and (2.38) can be calculated depending on the transmission line length l and PD source location z_s. In this way, the propagation of PDs or any other signals on a given transmission line can be simulated.

2.5 Validation Measurements

To validate the final transmission line model of (2.37) and (2.38), measurements are made using the exemplary power cable described in Section 2.3.7 (type N2XS2Y of Suedkabel GmbH). Therefore, two example measurements are shown in this section. In the first measurement, a PD source is located at the beginning of the power cable and the measurement is performed at the other end, see Subsection 2.5.1. The second validation measurement assumes a more realistic scenario where the PD source is located in the middle of the power cable, see Subsection 2.5.2.

2.5.1 Measurement Setup with PD Source at the Beginning of the Power Cable

The measurement setup is shown schematically in Fig. 2.9. The exemplary power cable with a length of $l = 10\,\mathrm{m}$ is connected on one side to the PD calibrator and on the other side to an oscilloscope. Thus, a PD pulse is injected at one end of the cable and the remaining voltage signal is measured at the other end. An oscilloscope with a bandwidth of 200 MHz and a sampling rate of 2.5 $\frac{\mathrm{GS}}{\mathrm{s}}$ is used (Tektronix MDO4024C). The transmitted voltage pulse u_2 is measured at an input channel with an input resistance of $R_{\mathrm{sc}} = 50\,\Omega$. Passive probes on high-impedance input channels would falsify the HF measurements due to their capacitive behavior.

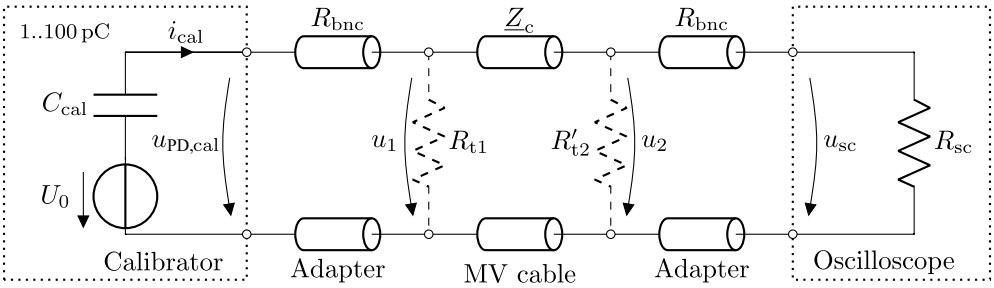

Figure 2.9: First measurement setup to validate the transmission line model. The PD source is located at the beginning of the power cable and the measurement is performed at the end of the cable.

Adapters similar to those in Section 2.3.7 are used to connect the power cable to the other devices, see Fig 2.10. The adapters are made of coaxial cable with a characteristic impedance of $R_{\mathrm{bnc}} = 50\,\Omega$. The separated ends of the adapters are soldered directly to the inner conductor and shielding of the power cable.

Figure 2.10: PD calibrator with adapter to connect to the power cable. An optional resistor R_{t1} can be soldered between the separated conductors to adjust the termination resistance $\underline{Z}_1$ of the power cable if necessary. The oscilloscope is connected in a similar way.

At these connection points, the conductors are unshielded. Unshielded cable sections add parasitic inductance to the measuring setup. This leads to unwanted low-pass behavior and thus to a falsified measurement. However, VNA measurements of the adapter's $\boldsymbol{S}$-parameters show that its low-pass behavior is negligible up to 100 MHz if care is taken to keep the unshielded conductor section as short as possible. The adapters can therefore be considered loss-free in the HF range. Thus, $u_{\mathrm{PD,cal}} \approx u_1$ and $u_{\mathrm{sc}} \approx u_2$.

Optional SMD-resistors R_{t1} and R'_{t2} can be soldered between the two unshielded wires of the adapters to adjust the termination impedance of the power cable at its beginning (PD calibrator side) and at its end (oscilloscope side):

$$\underline{Z}_1 = R_{\mathrm{t1}} \tag{2.54}$$

$$\underline{Z}_2 = R_{\mathrm{t2}} = R_{\mathrm{sc}} \parallel R'_{\mathrm{t2}} \tag{2.55}$$

These impedances determine the reflection coefficients at the beginning $\underline{r}_1$ and at the end $\underline{r}_2$ of the power cable according to (2.29) and (2.30). If the termination impedance matches the characteristic impedance $\underline{Z}_{\mathrm{c}}$ of the transmission line, reflections are minimized. $\underline{Z}_{\mathrm{c}}$ can be calculated with (2.17) or with the help of the measured $\boldsymbol{S}$-parameters. For the power cable used, $\underline{Z}_{\mathrm{c}} \approx 35.5\,\Omega$, is almost purely ohmic and nearly constant up to 1 GHz.

The amplitude of the generated calibrator pulse $u_{\mathrm{PD,cal}}$ depends on the termination resistor R_{t1} connected to its terminals. In Section 2.1, the 100 pC calibrator voltage pulse was measured directly at a 50 Ω input channel of an oscilloscope. For simplicity, this impedance-matched voltage pulse of the calibrator was recorded. The following relationship applies between the impedance-matched voltage pulse $u_{\mathrm{PD,cal,50\Omega}}$ and the actual pulses at other R_{t1}:

$$u_{\mathrm{PD,cal}} = u_{\mathrm{PD,cal,50\Omega}} \frac{R_{\mathrm{t1}}}{R_{\mathrm{sc}}} \tag{2.56}$$

Thus, before each validation measurement, the initial calibrator PD pulse $u_{\mathrm{PD,cal}}$ is calculated for the given R_{t1} according to (2.56). Then, the Gaussian pulse model parameters are fitted to $u_{\mathrm{PD,cal}}$ with the least squares optimizer to get $u_{\mathrm{PD,mod}}$. Subsequently, (2.3) is calculated with these PD model parameters. The obtained VSD $\underline{U}_{\mathrm{PD,mod}}$ is then used as PD source $\underline{U}_{\mathrm{s}}$ of the transmission line model (in the figures, the VSD is plotted on a logarithmic scale – mind the index dB). Now (2.37) or (2.38) can be solved for the given power cable. The resulting VSD $\underline{U}_2$ can now be transferred back into the time domain by inverse Fourier transform in order to obtain the voltage u_2 at the right end of the power cable. This simulated voltage can now be compared with the measurement on the oscilloscope.

Fig. 2.11 shows an example result. For this, the termination resistor $R_{t1} = 35\,\Omega \approx \underline{Z}_c$ is chosen to avoid reflections. At the other side no additional resistor R'_{t2} is used, i. e., $R_{t2} = 50\,\Omega$. 100 pC pulses are generated by the calibrator. Furthermore, $z_s = 0$, $z = l = 10\,\text{m}$, and $\underline{I}_s = 0$ applies.

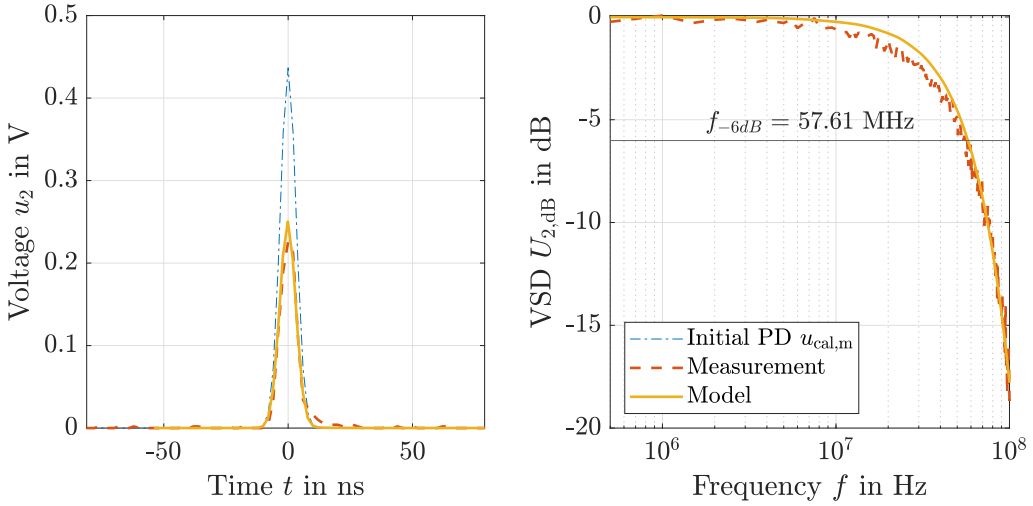

Figure 2.11: First measurement to validate the transmission line model: 100 pC impulse after propagation on a 10 m long power cable in the time and frequency domain with $R_{t1} = 35\,\Omega$ and $R_{t2} = 50\,\Omega$.

Transmission line model and measurement are similar in time and frequency domain. The remaining deviation can be explained by minor reflections that occur at the discontinuities between the power cable and the adapters. The characteristic impedance changes there from approximately $\underline{Z}_c = 35.5\,\Omega$ to $R_{bnc} = 50\,\Omega$ and minor reflections will occur. The transmission line model does not account for these reflections. However, the reflections should be minor, because $\underline{Z}_c$ and R_{bnc} do not differ much.

Another explanation of the deviation between measurement and model is that the adapters are unshielded at the connection points to the power cable. This adds a small parasitic inductance to the measurement setup, resulting in additional low-pass behavior. Apart from these minor deviations, the model is able to predict the transmission behavior of the power cable with high accuracy.

As expected, the amplitude of the initial PD pulse decreases due to attenuation. In the time domain the decrease of the PD amplitude can be calculated as follows:

$$u_{\text{dec}} = \frac{\hat{u}_2}{\hat{u}_{\text{cal,m}}} \tag{2.57}$$

After 10 m the PD amplitude $\hat{u}_2$ in Fig. 2.11 has decreased to about $u_{\mathrm{dec}} = 0.48$ of its initial value $\hat{u}_{\mathrm{cal,m}}$ (50 percent is the theoretical maximum). The cut-off frequency $f_{-6\,\mathrm{dB}}$ has dropped from the initial 62.72 MHz to about 57.61 MHz.

2.5.2 Measurement Setup with PD Source in the Middle of the Power Cable

This time the calibrator is connected between two pieces of the exemplary power cable, each 10 m long. The measurement setup is shown schematically in Fig. 2.12. The transmission line model is only applicable if both power cable sections have a similar characteristic impedance $\underline{Z}_{\mathrm{c1}} \approx \underline{Z}_{\mathrm{c2}}$. Due to the great similarity in construction, this assumption should be true for most XLPE power cables.

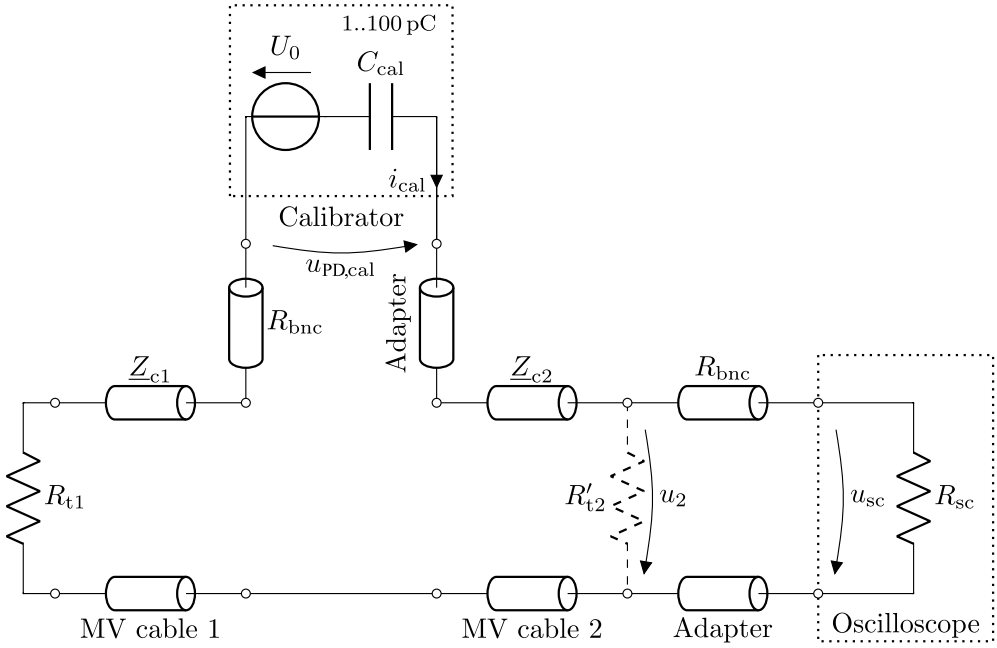

Figure 2.12: Second measurement setup to validate the transmission line model. The PD source is located in the middle of two power cables and the measurement is performed at one end.

If the calibrator is connected in series between two power cables, then $u_{\mathrm{cal}} \approx u_{\mathrm{cal,50\Omega}}$ applies and (2.56) is not needed. The rest of the measurement procedure remains the same.

For the example measurement the terminating resistors $R_{\mathrm{t1}} = R_{\mathrm{t2}} = 33\,\Omega$ are chosen to minimize reflections, i. e., an additional resistor $R'_{\mathrm{t2}} = 100\,\Omega$ is implemented in parallel to $R_{\mathrm{sc}} = 50\,\Omega$. Then, (2.37) and (2.38) are solved with $z_{\mathrm{s}} = 10\,\mathrm{m}$, $z = l = 20\,\mathrm{m}$, and $\underline{I}_{\mathrm{s}} = 0$. The result is shown in Fig. 2.13.

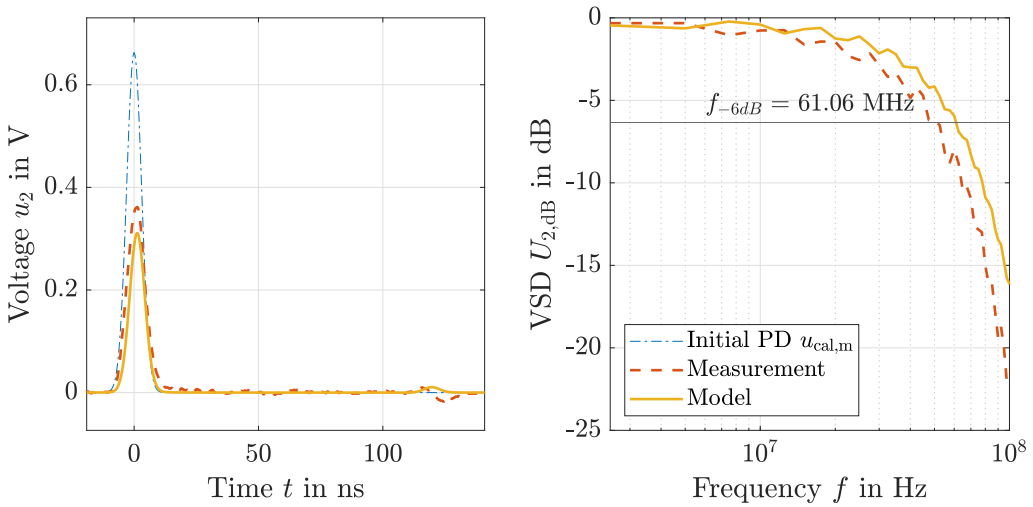

Figure 2.13: Second measurement to validate the transmission line model: 100 pC impulse in the middle of 20 m of power cable in the time and frequency domain with $R_{\mathrm{t1}} = R_{\mathrm{t2}} = 33\,\Omega$.

Again, the results of the transmission line model and measurement are similar in both time and frequency domain. Minor reflections occur at R_{t1} and are measured on the oscilloscope after about 120 ns, which corresponds to about 22 m propagation distance. These reflections due to impedance mismatch are low because the terminating resistors are approximately equal to $\underline{Z}_{\mathrm{c}}$. In the frequency domain, the measurement shows a stronger low-pass behavior compared to the model. This is probably due to longer unshielded cable sections, which could not be avoided in this test setup. All unshielded connections should be kept as short as possible to avoid parasitic inductance. In conclusion, the model predicts the transmission behavior of the power cable well.

The validation results look very promising. Overall, it can be concluded that the developed transmission line model predicts the propagation of PD signals on XLPE power cables with sufficient accuracy. Thus, the transmission line model can be used to simulate the propagation of any HF signal on a power cable. Presumably, the model is also valid for any other transmission line, provided its propagation constant is known in detail, but this needs to be further verified. In the next section, the transmission line model is used to study the PD propagation process on power cables.

2.6 Simulation Results

Power cables are excellent for transmitting large amounts of energy at a frequency of 50 Hz over long distances, but are not well suited for transmitting HF signals. They

therefore behave like a low-pass filter. Possible PD pulses are thus subject to attenuation and dispersion. The longer the transmission distance, the more the initial PD signal is distorted. Accordingly, the bandwidth of the PD signal decreases. The remaining bandwidth at the end of the power cable can be investigated using the transmission line model. The following section presents the results of such simulations.

In Section 2.6.1, attenuation and bandwidth of PD signals are studied as a function of the transmitted distance. Section 2.6.2 investigates the influence of the semiconducting cable layers on its propagation constant. In addition, Section 2.6.3 shows the influence of cable joints and end terminations on PD transmission.

For all simulations, the exemplary cable type from Section 2.3.7 is used again. It is representative for most modern XLPE cables as they are all similar in structure.

2.6.1 Remaining PD Bandwidth at the End of a Power Cable

In order to investigate the relationship between PD attenuation/dispersion and the transmitted distance, the simulation shown in Section 2.5.1 is performed for various power cable lengths. In addition, the PD pulse width is varied in the simulations by adjusting the parameter c (cf. (2.2) on page 10). The results for three PDs with different pulse widths are shown in Fig. 2.14. The decrease of the pulse amplitude in the time domain is calculated with (2.57).

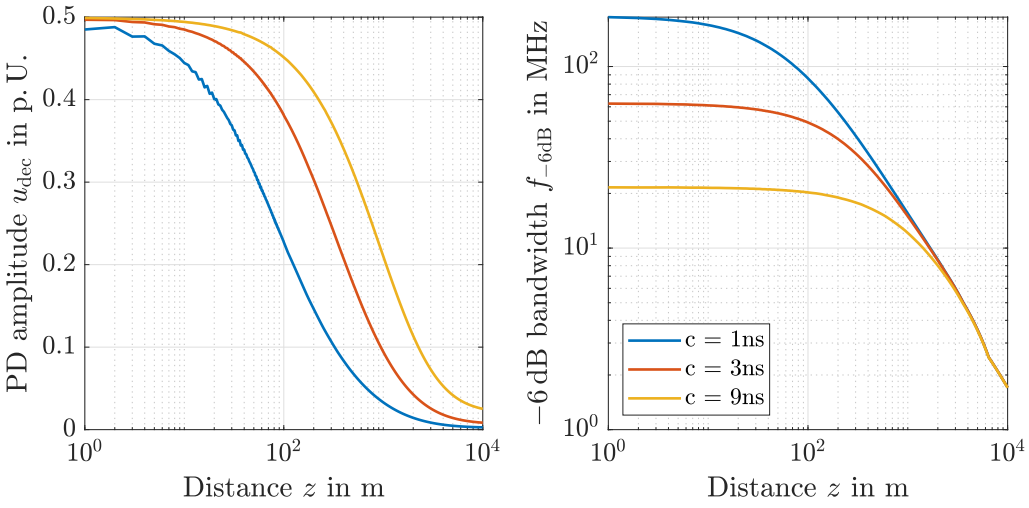

Figure 2.14: Normalized PD amplitude and bandwidth as a function of transmission distance z.

The shorter the pulse width of the initial PD, the more its amplitude is attenuated during transmission. This can be seen from the normalized amplitude plot. The amplitude

of the shortest pulse of duration $c = 1$ ns drops to 20 percent after about 120 m, while the $c = 9$ ns pulse travels about 1040 m for the same attenuation. The bandwidth also decreases with increasing transmission distance z, especially for PD with short pulse duration. The bandwidth of the $c = 1$ ns pulse has already decreased by more than 50 percent after 100 m. After about 400 m, the bandwidth of the red marked PD is < 30 MHz, i. e., within the HF range. After 1 km of transmission, the bandwidths of all three PD almost coincide at about 10 MHz.

It can be concluded that bandwidths > 30 MHz can be expected only for PD with short pulse widths $c < 6$ ns, provided their transmission distance is short. Moreover, the shorter the pulse width, the faster the pulse amplitude decreases. Therefore, PD pulses with frequency content in the VHF range > 30 MHz are hardly measurable on power cables. The measurement bandwidth of a PD sensor should rather cover the HF range < 30 MHz. This frequency range should be sufficient to cover the full bandwidth of most PDs. It also covers large parts of the bandwidth of possible VHF pulses (only the highest frequency components are neglected).

The results also show that it is important to keep the PD transmission distance as short as possible. For successful PD detection, the power cables should therefore always be monitored at both ends. The more sensors are installed, the more likely the PDs will be detected. Therefore, the cost per sensor should be as low as possible.

2.6.2 Influence of the Semiconducting Layers of the Power Cable

The PD attenuation depends on the propagation constant $\underline{\gamma}$ of the power cable. Fig. 2.15 shows the attenuation constant α and the phase velocity v_p of the exemplary power cable. To show the influence of the semiconducting layers of the cable, the propagation constant is calculated once for the whole cable and once neglecting the semiconducting layers.

It can be seen that most of the attenuation is due to the semiconducting layers. More precisely, the $\underline{\gamma}$ depends highly on the thickness of these two layers d_{sc1} and d_{sc2}. The thinner they are, the better HF signals are transmitted. It can be concluded that most of the low-pass behavior of a power cable is due to the semiconducting layers.

2.6.3 Influence of Cable End Terminations and Joints

During the validations, it was found that the measurements are always slightly more attenuated than the transmission line model results. The reason is that the model is based on a completely shielded cable. In reality, the cables are not shielded over their entire length. Cable end terminations are attached to each end of the power cables (cf.

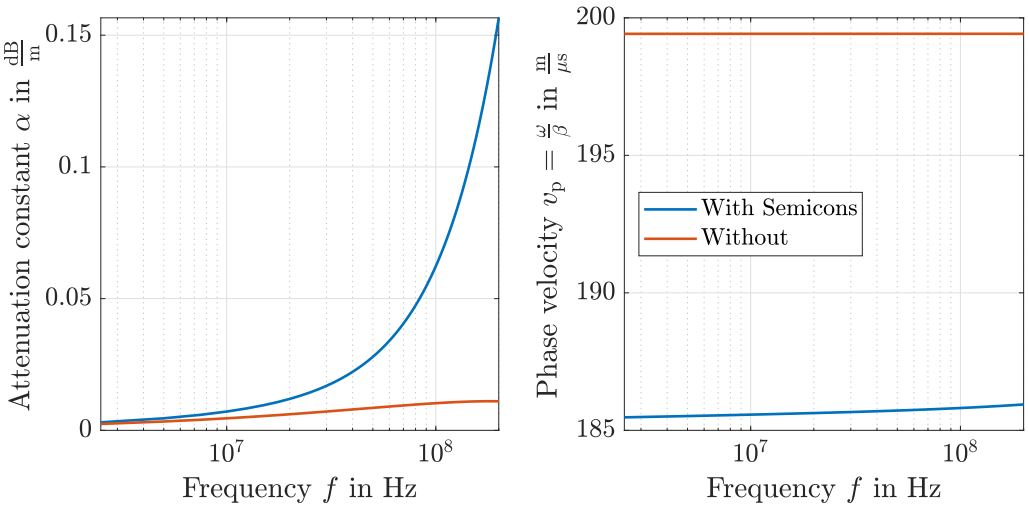

Figure 2.15: Attenuation constant and phase velocity of the exemplary power cable with and without semiconducting layers.

Fig. 3.2 on page 39). At these points, the inner and outer conductors are separated from each other, i. e., these section of the power cable are not shielded. This leads to parasitic inductance and additional low-pass behavior, which is not considered in the transmission line model.

To show the effects of a cable end termination, measurements similar to those in Section 2.5.1 are made for a 10 m long power cable with an end termination installed at one end. This adds about 0.5 m of unshielded cable to this end. The additional low-pass behavior resulting from this cable end termination can be seen in Fig. 2.16 in comparison with a measurement of a fully shielded power cable of the same length.

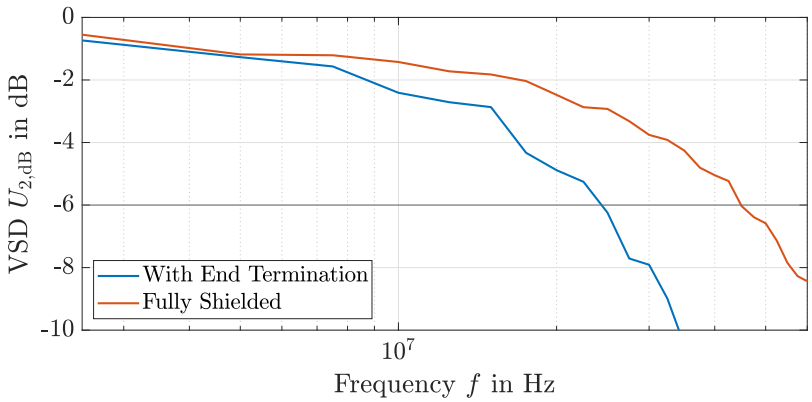

Figure 2.16: VSD of a 100 pC pulse after propagation on a 10 m long power cable. The cable is equipped once with an end termination and once without (fully shielded).

As expected, the bandwidth of the PD pulse decreases with increasing parasitic inductance, i. e., due to the installation of the cable end termination. Thus, the transmission line model always overestimates reality and its results should be considered as the best possible result. With this in mind, the determined measurement bandwidth of 30 MHz still seems to be unnecessarily high. Fig. 2.16 shows that the cable end termination reduces the bandwidth of the PD pulse by additional $\approx$ 20 MHz compared to the fully shielded measurement. To account for this extra low-pass, the PD sensor should therefore only be optimized for a bandwidth of 10 MHz. A similar bandwidth for PD measurements on power cables is recommended by [25].

Furthermore, real cable systems often consist of many different types of cables. Any discontinuity in the characteristic impedance leads to small reflections and further reduction of the PD bandwidth. This circumstance is not considered in the transmission line model. However, since most modern power cable types are similar in construction and their characteristic impedance is similar, reflections at the joints are low [47]. The entire cable section can thus be treated as a single cable, provided that the joints are installed correctly.

3 High-Frequency Current Transformer Design

To detect PDs on power cables, a sensor with a measurement bandwidth of about 10 MHz is needed. The sensor should be installed at the ends of the power cables, but without contacting their HV potential, i. e., the sensor should be galvanically isolated from the power cable circuit to enable online monitoring. Furthermore, the sensor should be as cheap as possible so that DSOs can monitor as many cables as possible. Based on these requirements, a PD sensor with maximum sensitivity is developed in this chapter.

PD sensors operating in the HF range are usually based on inductive or capacitive coupling between sensor and device under test. For PD measurements on power cables, the inductive approach using current transformers is the most suitable, as they can be easily installed on existing cables. Current transformers specially designed for measuring HF signals, such as PDs, are referred to as high-frequency current transformers (HFCT). HFCTs are inexpensive, the coupling between sensor and device under test is galvanically isolated, and they are therefore inherently suitable for online monitoring (as long as their core is not magnetically saturated). An alternative inductive sensor is the coreless Rogowski coil, which is immune to magnetic saturation but much less sensitive in the HF range compared to HFCTs [11], [43]. Since the PD signals to be measured are very weak, HFCTs are preferable to Rogowski coils, even though they are susceptible to magnetic saturation during online monitoring (Chapter 4 will address this issue).

Hence, this chapter is about HFCT design and is organized as follows. The operating principle of HFCTs is explained first in Section 3.1. Second, the magnetic properties of ferrite materials are investigated in Section 3.2. Third, a model for calculating the transfer function of HFCTs is presented in Section 3.3. Afterwards, Section 3.4 presents a method for measuring the transfer function of HFCTs. Subsequently, the developed HFCT model is validated against measurements in Section 3.5. Finally, in Section 3.6, an HFCT for online power cable monitoring is optimized based on the above requirements. Parts of this chapter have been published in [48], [49].

3.1 Overview and Operating Principle of HFCTs

The construction of an HFCT is simple and is essentially based on a magnetic core and a secondary winding with n_2 turns wound around this core, see Fig. 3.1a. The core is usually toroidal and made of a ferromagnetic material. The measurement bandwidth of an HFCT depends primarily on the selected core material. For good coupling in the HF range, ceramic ferrite materials are best. The resulting frequency response of such an

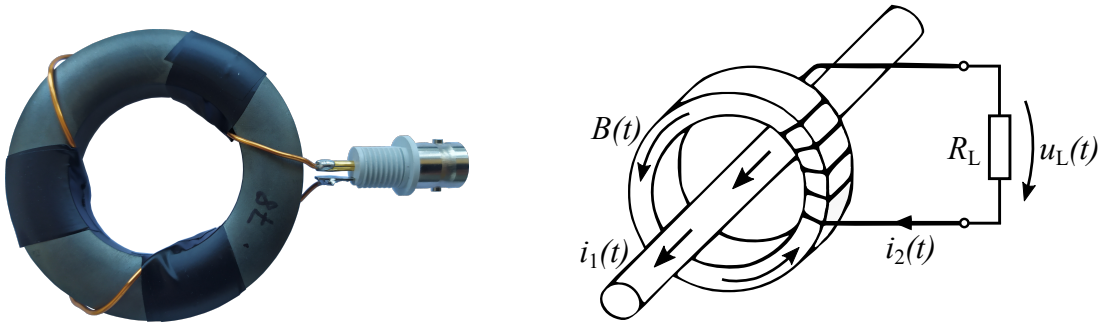

(a) (b)

Figure 3.1: Left: An HFCT is made of a copper winding with n_2 turns wound on a ferrite toroid. Right: Schematic representation of the operation of an HFCT.

HFCT sensor is that of a wideband band-pass. To flatten/linearize the band-pass, a load resistor R_L (burden) is usually connected to the secondary winding.

The operating principle is shown in Fig. 3.1b. The toroid is placed around an electrical conductor to measure the current $i_1(t)$ flowing through it. This primary current flow causes a magnetic field $H(t)$ around the conductor. Assuming that the primary conductor is straight and centered in the HFCT, the magnetic field $H(t)$ can be calculated as follows [34]:

$$H(t) = \frac{i_1(t)}{2\pi r_\mathrm{c}} \tag{3.1}$$

where r_c is the distance between the center of the primary conductor and the HFCT in m. For a toroidal HFCT core with outer radius $r_\mathrm{c,out}$ and inner radius $r_\mathrm{c,in}$, the mean radius can be used, yielding:

$$r_\mathrm{c} = \frac{r_\mathrm{c,out} + r_\mathrm{c,in}}{2} \tag{3.2}$$

The magnetic field $H(t)$ magnetizes the ferrite core. Provided that the core material has a constant permeability μ_c, the resulting magnetic flux density $B(t)$ in the core can be calculated with the following equation:

$$B(t) = \mu_\mathrm{c}\mu_0\, H(t) \tag{3.3}$$

The permeability of ferrites is high and approximately constant as long as the material is not saturated. The magnetic flux density $B(t)$ in the HFCT core induces a reverse current $i_2(t)$ in the secondary winding, which is proportional to the primary current $i_1(t)$:

$$\frac{i_1(t)}{i_2(t)} = \frac{n_2}{n_1} \tag{3.4}$$

where $n_1 = 1$ is the number of turns of the primary winding, which usually consists of only one turn. Again, (3.4) is only valid at constant μ_c, i. e., at unsaturated HFCT

operation. The secondary current $i_2(t)$ then causes a measurable voltage $u_L(t)$ at the HFCT output. The output voltage can be measured with an oscilloscope, for example. In this way, the primary current $i_1(t)$ is inductively coupled and transformed to the secondary side.

The ratio between the HFCT output voltage u_L and the input current i_1 of the primary conductor is the so-called transfer impedance Z_T of the HFCT:

$$Z_T = \frac{u_L}{i_1} \tag{3.5}$$

The transfer impedance is specified in the unit $\frac{V}{A}$ or Ω and is equal to the transfer function of the sensor. The transfer impedance is frequency dependent and depends primarily on the permeability of the core material [12] [50], which will be discussed in more detail in the next section.

To measure the currents flowing in a power cable, the HFCT can be installed at the end termination of the power cable around either the inner or outer conductor (shielding), see Fig. 3.2. Position 2 is the more optimal location because the PD signals are less disturbed. Installing the HFCT at position 1 is less suitable because the earth path acts like a large antenna for noise and interference. Therefore, position 2 is preferred, although the HFCT is then fully exposed to the power cable's operating current. For more insights into this discussion, see [11]. The rest of the dissertation assumes installation at position 2.

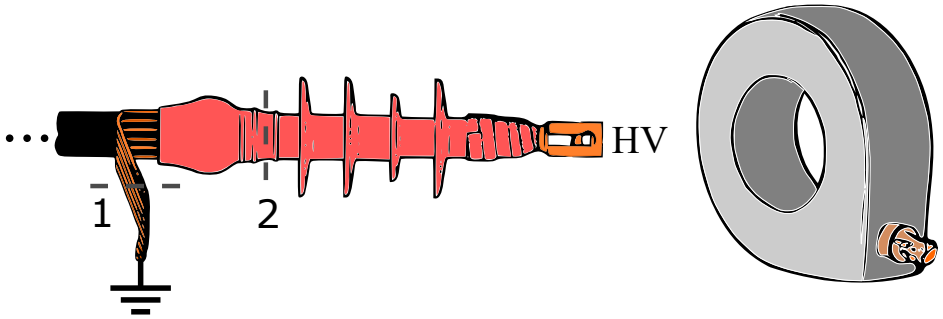

Figure 3.2: Possible installation locations of an HFCT at the end termination of a power cable. Either around the cable shield (1), which is connected to earth/ground potential, or around the insulated part of the inner conductor (2), which is connected to HV potential.

3.2 Magnetic Properties of Ferrite Materials

It has already been mentioned that for measurements in the HF range, such as PD measurements, HFCTs with cores made of ceramic ferrite material are used. The ferrites

usually consist of soft magnetic manganese-zinc (MnZn) or nickel-zinc (NiZn) ceramics. This section takes a closer look at the properties of such ferrite materials.

To study the magnetic properties of a magnetic material, it is best to record the magnetization curve of the material. The magnetization curve shows the relationship between an external magnetic field H and the resulting magnetic flux density B in the material. To measure the B-H curve of an HFCT core, the HFCT is installed around an electrical conductor as shown in Fig. 3.3.

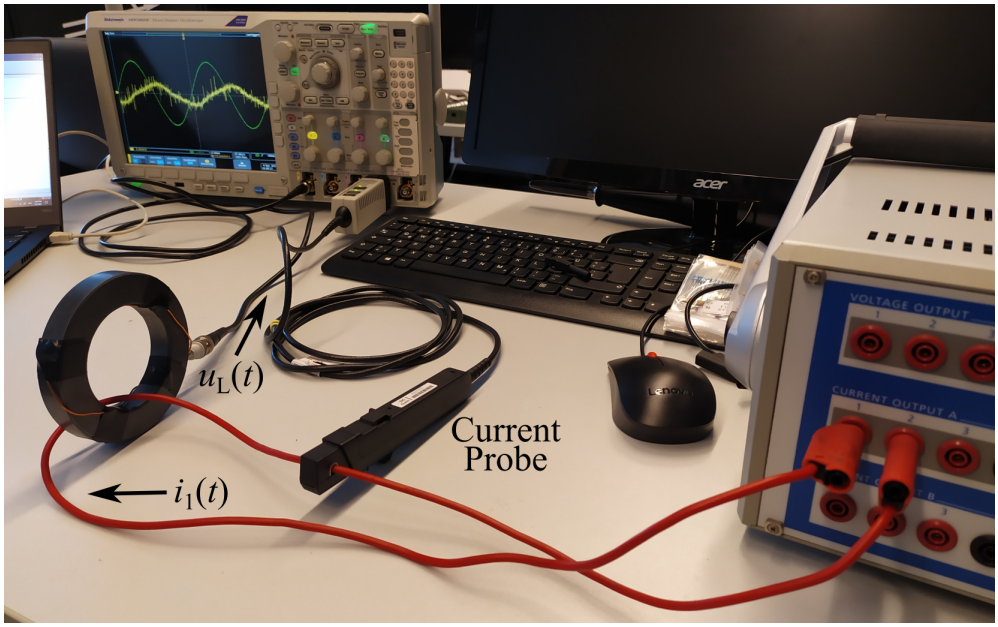

Figure 3.3: Experimental setup for measuring the magnetization curve of an HFCT core. The HFCT is magnetized by an external magnetic field H generated by a sinusoidal input current i_1. Input current and output voltage of the HFCT are measured with an oscilloscope.

The input current is set to a sine with amplitude $\hat{i}_1$ and frequency f to generate an external magnetic field, $i_1(t) = \hat{i}_1 \sin(2\pi f t)$. The output voltage $u_L(t)$ of the HFCT is then measured with an oscilloscope. Afterwards, the H field is calculated using (3.1). The B field is calculated using the following equation [51]:

$$B(t) = \frac{1}{n_2 A_c} \int u_L(t)\, \mathrm{d}t \tag{3.6}$$

For the experimental setup, the input current is generated with a CMC-256-6 from Omicron. The HFCT output voltage is connected to the 50 Ω-input channel of a Tektronix MDO 4024 C oscilloscope ($R_L = 50\,\Omega$). The input current is measured with a TCP0030A current probe on the same oscilloscope.

Fig. 3.4 shows the magnetization curve of an exemplary HFCT core (green curve). The ferrite core is made of material No. 43 from the manufacturer Fair-Rite (NiZn ferrite). For the measurement, the input current of the HFCT is set to a sine with an amplitude of about $\hat{i} = 70\,\mathrm{A}$ and a frequency of $f = 50\,\mathrm{Hz}$.

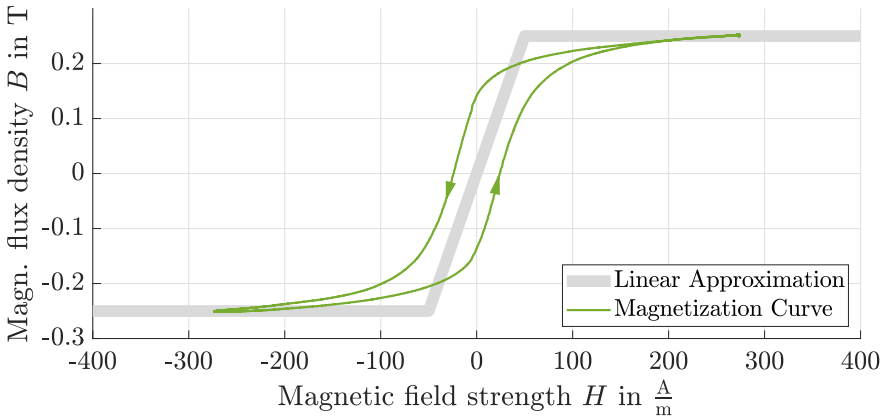

Figure 3.4: Magnetization curve of an exemplary soft-magnetic ferrite material. The green curve is recorded at a sinusoidal magnetizing field H with a frequency of 50 Hz and an amplitude of $\hat{H} \approx 280\,\frac{\mathrm{A}}{\mathrm{m}}$ (corresponds to a primary current with RMS of $I_{1,50\mathrm{Hz}} = 50\,\mathrm{A}$).

It can be seen that the magnetization curve is nonlinear due to hysteresis and saturation. Since the external field H is an alternating field, hysteresis losses occur because the orientation of the core magnetization is constantly changing. Hysteresis losses are equal to the enclosed area of the curve. Ferrites are soft magnetic materials and are characterized by a narrow hysteresis curve. They are therefore easy to demagnetize (low hysteresis losses). The slope of the magnetization curve is equal to the permeability μ_c of the core material. The shape of of the B-H curve depends on the frequency f of the magnetizing field H. As frequency increases, hysteresis losses usually increase and permeability decreases [52].

Since the shape of the B-H curve, and thus the permeability of a ferrite material, is frequency dependent, it is useful to switch to the frequency domain for further considerations. For this purpose, all time domain signals are transformed into the frequency domain by Fourier transform, e. g., $u_\mathrm{L}(t) \overset{\mathcal{F}}{\longrightarrow} \underline{U}_\mathrm{L}(f)$ or $H(t) \overset{\mathcal{F}}{\longrightarrow} \underline{H}(f)$.

Because of hysteresis, it is not possible to write a functional relation $B = f(H)$, since the value of B at any instant depends not only on H at that instant, but also on its prior history. With soft magnetic ferrites, however, the hysteresis effect is quite small and negligible (narrow magnetization curve). Neglecting the hysteresis losses, the magnetization curve can be linearized, as shown in Fig. 3.4. The linear approximation can be divided into

three sections, two of which describe the saturated state at which the permeability μ_c becomes zero (saturation mode). An HFCT should always be operated in the unsaturated state, i. e., in the middle section at which the permeability is approximately constant and much greater than zero $\mu_{c,lin} \gg 0$ (linear operating mode). Provided the HFCT is unsaturated, the linearized core permeability thus depends only on the ferrite material and frequency, $\mu_{c,lin}(f)$. In the remainder of this chapter, it is assumed that the HFCT is always unsaturated. How to avoid saturation and ensure linear HFCT operation in practice is then explained in the next chapter.

To further account for the previously neglected hysteresis losses, it is possible to introduce a complex core permeability [53]:

$$\underline{\mu}_c(f) = \mu_c'(f) - \mathrm{j}\mu_c''(f) \tag{3.7}$$

where the real part corresponds to the already defined linear permeability at a given frequency $\mu_c'(f) = \mu_{c,lin}(f)$, i. e., the slope of the linearized magnetization curve of Fig. 3.4, while the imaginary part $\mu_c''(f)$ describes the magnitude of the hysteresis losses caused by the oscillating magnetic field (increases with frequency). The complex permeability $\underline{\mu}_c(f)$ of a ferrite material can usually be obtained from the manufacturer's website. For the exemplary core of material No. 43, the complex permeability is given in the data sheet [54] and is shown in Fig. 3.5. It can be seen that the imaginary part and thus the hysteresis loss increases with frequency. The real part is constant at the beginning and then decreases continuously from about 2 MHz.

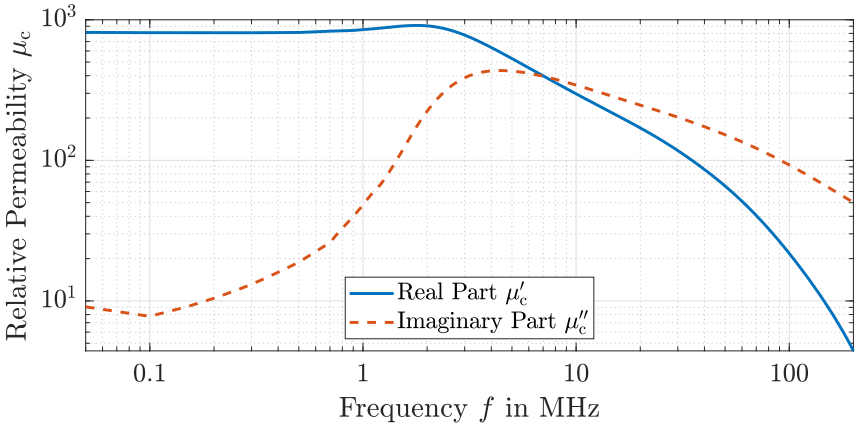

Figure 3.5: Frequency dependent complex permeability of ferrite material No. 43 from Fair-Rite, measured and provided by the manufacturer.

If the complex permeability of the core material is known, the HFCT model derived in the next section can be used to calculate its transfer function.

3.3 HFCT Model

Deriving an analytical HFCT model that is valid up to the HF range is challenging despite their simple construction. There are only a few peer-reviewed publications of high quality that provide some general advice on HFCT design [12], [50], [55], [56], mostly based on measurements, but none of these publications includes a reliable mathematical HFCT model. Therefore, a comprehensive HFCT model for the HF range is derived in this section and validated against measurements in Section 3.5.

3.3.1 Derivation of the HFCT Model

The basic design of an HFCT is not much different from that of a conventional power transformer. Therefore, to derive an HFCT model, the well-known equivalent circuit of a transformer shown in Fig. 3.6 can be used.

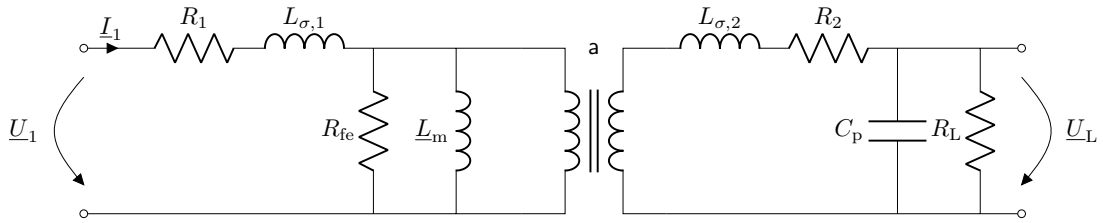

Figure 3.6: Equivalent circuit of an HFCT in the frequency domain.

It consists mainly of two parts, which stand for the primary and secondary windings on the ferrite core. Both sides are coupled by an ideal transformer with a turns ratio of $a = \frac{n_2}{n_1}$, where $n_1 = 1$. The ideal transformer adds no phase shift to the input signal since the model assumes linear or unsaturated HFCT operation, i. e., a is not complex.

The input current $\underline{I}_1$ flowing in the primary winding excites a magnetic flux in the HFCT core. This behavior is represented by the magnetizing inductance $\underline{L}_{\mathrm{m}}$. Core losses due to hysteresis and eddy currents are accounted for by R_{fe}. With ferrite materials, eddy current losses are very low even at high frequencies due to their low conductivity [57]. The hysteresis loss is already included in the imaginary part $\mu_{\mathrm{c}}''(f)$ of the complex permeability of the ferrite material. Therefore, R_{fe} can be neglected when using ferrite toroids as HFCT core material.

The magnetizing inductance is calculated as follows [34]:

$$\underline{L}_{\mathrm{m}}(f) = \frac{\mu_0 \underline{\mu}_{\mathrm{c}}(f) h_{\mathrm{c}} n_1^2}{2\pi} \log \frac{r_{\mathrm{c,out}}}{r_{\mathrm{c,in}}} \approx \frac{\mu_0 \underline{\mu}_{\mathrm{c}}(f) A_{\mathrm{c}} n_1^2}{2\pi r_{\mathrm{c}}} \tag{3.8}$$

where $r_{c,out}$ is the outer radius, $r_{c,in}$ is the inner radius and h_c is the height or thickness of the HFCT ring core in m and A_c is its cross-sectional area in m^2:

$$A_c = (r_{c,out} - r_{c,in}) \cdot h_c \tag{3.9}$$

R_L is the load or burden resistance connected to the output of the HFCT. This resistance is defined by the input of a measuring device and is usually $R_L = 50\,\Omega$.

R_1 and R_2 represent the resistance of the winding material, which leads to thermal losses. The secondary winding is constructed from enameled copper wire of radius r_2 in m. One turn has the length l_2 in m. Taking the skin effect into account, the secondary winding resistance R_2 can be calculated by [26]:

$$R_2(f) = \sqrt{\frac{\omega \mu_0 \mu_{co}}{2\sigma_{co}}} \frac{n_2 l_2}{2\pi r_2} \tag{3.10}$$

It will be shown later that only a few secondary turns are required to build a highly sensitive HFCT sensor, so that in most cases $n_2 \leq 5$. Consequently, in the HF range, $R_2 \ll R_L$ and R_2 can therefore usually be neglected.

The magnetic flux in the core flows through all turns of the two windings. However, due to imperfect coupling, there is also a leakage flux that does not connect all the turns. $L_{\sigma,1}$ and $L_{\sigma,2}$ account for these leakage flux losses. Since toroidal cores have a high magnetic efficiency, which means that the magnetic flux is almost only concentrated in the ferrite core, the leakage flux should be very low [58].

For the same reason, noise from electromagnetic radiation is unlikely to couple into the HFCT ferrite core. Therefore, no additional shielding is required for an HFCT sensor.

The coupling via the electric field is taken into account by the parasitic capacitance C_p. This phenomenon occurs mainly at high frequencies between adjacent turns of the secondary winding. On the primary side, capacitive coupling is negligible since the primary winding consists of only a single turn $n_1 = 1$. For the same reasons, R_1 and $L_{\sigma,1}$ are close to zero and negligible.

For simplicity, it is common to transfer all remaining elements to one side. For this purpose, the magnetizing inductance $\underline{L}_m$ is transferred from the primary side to the secondary side by multiplication with the squared turns ratio:

$$\underline{L}'_m(f) = \underline{L}_m(f) \cdot a^2 = \frac{\mu_0 \underline{\mu}_c(f) h_c n_2^2}{2\pi} \log \frac{r_{c,out}}{r_{c,in}} \approx \frac{\mu_0 \underline{\mu}_c(f) A_c n_2^2}{2\pi r_c} \tag{3.11}$$

The resulting simplified equivalent circuit of an HFCT is shown in Fig. 3.7.

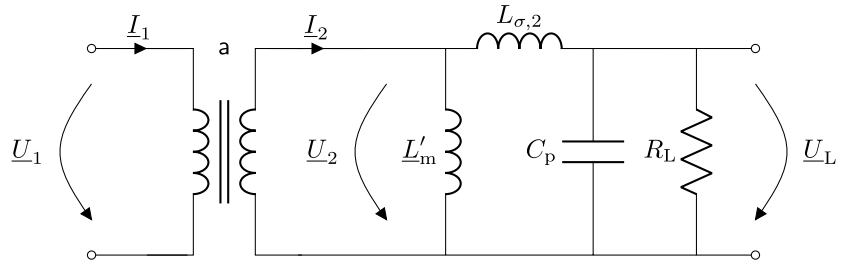

Figure 3.7: Simplified equivalent circuit of an HFCT with all elements transferred to the secondary side.

To determine the transfer function of the HFCT, the impedances of the inductive and capacitive elements must first be calculated:

$$\underline{Z}'_\mathrm{m}(f) = \mathrm{j}\omega\underline{L}'_\mathrm{m}(f) \tag{3.12}$$

$$\underline{Z}_{\sigma,2}(f) = \mathrm{j}\omega L_{\sigma,2} \tag{3.13}$$

$$\underline{Z}_\mathrm{p}(f) = -\mathrm{j}\frac{1}{\omega C_\mathrm{p}} \tag{3.14}$$

Now, the impedance of the elements of the secondary side $\underline{Z}_2$ can be summarized:

$$\underline{Z}_2(f) = \frac{R_\mathrm{L}\cdot\underline{Z}_\mathrm{p}(f)}{R_\mathrm{L}+\underline{Z}_\mathrm{p}(f)} + \underline{Z}_{\sigma,2}(f) = \underline{Z}_\mathrm{Lp}(f) + \underline{Z}_{\sigma,2}(f) \tag{3.15}$$

Then, the total impedance $\underline{Z}_\mathrm{tot}$ of the HFCT model is:

$$\underline{Z}_\mathrm{tot}(f) = \frac{\underline{Z}'_\mathrm{m}(f)\cdot\underline{Z}_2(f)}{\underline{Z}'_\mathrm{m}(f)+\underline{Z}_2(f)} \tag{3.16}$$

Due to Ohm's law, the secondary side voltage $\underline{U}_2$ of the HFCT is:

$$\underline{U}_2(f) = \underline{Z}_\mathrm{tot}(f)\cdot\underline{I}_2(f) \tag{3.17}$$

The HFCT output voltage $\underline{U}_\mathrm{L}$ can then be calculated using the voltage divider rule:

$$\underline{U}_\mathrm{L}(f) = \underline{U}_2(f)\cdot\frac{\underline{Z}_\mathrm{Lp}(f)}{\underline{Z}_2(f)} \tag{3.18}$$

Finally, substituting (3.17) into (3.18) and considering the current transformation ratio $\underline{I}_1(f) = \underline{I}_2(f)\cdot a$ of the ideal transformer, the transfer impedance $\underline{Z}_\mathrm{T}$ of the HFCT can

be calculated according to (3.5):

$$\underline{Z}_{\mathrm{T}}(f) = \frac{\underline{U}_{\mathrm{L}}(f)}{\underline{I}_1(f)} = \underline{Z}_{\mathrm{tot}}(f) \cdot \frac{\underline{Z}_{\mathrm{Lp}}(f)}{\underline{Z}_2(f)} \cdot \frac{1}{a} \tag{3.19}$$

$$\underline{Z}_{\mathrm{T}}(f) = \frac{\mathrm{j}\omega \underline{L}'_{\mathrm{m}}(f) R_{\mathrm{L}}}{R_{\mathrm{L}} + \mathrm{j}\omega(\underline{L}'_{\mathrm{m}}(f) + L_{\sigma,2}) - \omega^2 C_{\mathrm{p}} R_{\mathrm{L}}(\underline{L}'_{\mathrm{m}}(f) + L_{\sigma,2})} \cdot \frac{1}{n_2} \tag{3.20}$$

This equation can now be used to calculate the HFCT transfer function. The result is equal to the frequency dependent HFCT sensitivity.

3.3.2 Ideal HFCT Model

If the parasitic elements $L_{\sigma,2}$ and C_{p} are not known, they can also be neglected and set to 0 to obtain an ideal HFCT model where all losses are neglected. Then, the HFCT transfer function of (3.20) simplifies to:

$$\underline{Z}_{\mathrm{T}}(f) = \frac{\underline{U}_{\mathrm{L}}(f)}{\underline{I}_1(f)} = \frac{\mathrm{j}\omega \underline{L}'_{\mathrm{m}}(f) \cdot R_{\mathrm{L}}}{\mathrm{j}\omega \underline{L}'_{\mathrm{m}}(f) + R_{\mathrm{L}}} \cdot \frac{1}{n_2} = \frac{\mathrm{j}\omega \frac{\underline{L}'_{\mathrm{m}}(f)}{R_{\mathrm{L}}}}{\mathrm{j}\omega \frac{\underline{L}'_{\mathrm{m}}(f)}{R_{\mathrm{L}}} + 1} \cdot \frac{R_{\mathrm{L}}}{n_2} \tag{3.21}$$

Calculating or measuring the parasitic elements of an HFCT is a difficult task. Therefore, no calculation method for determining $L_{\sigma,2}$ and C_{p} is given in this work (part of future research). Instead, the ideal HFCT model from (3.21) is used for all the simulations of the following sections.

3.3.3 Analysis of the HFCT Transfer Function

Equation (3.21) indicates that the ideal HFCT behaves like a high-pass. For better analysis of the transfer function of an ideal HFCT, a Bode plot of (3.21) is shown in Fig. 3.8. For the Bode plot, the magnetizing inductance is set to a constant value of $L'_{\mathrm{m}} = 10\,\mu\mathrm{H}$, while $n_2 = 3$ and R_{L} is varied.

It can be seen that an HFCT behaves like an inductance at low frequencies such as 50 Hz. Then $\mathrm{j}\omega \underline{L}'_{\mathrm{m}}(f) \ll R_{\mathrm{L}}$ holds and the transfer function (3.21) simplifies to:

$$\underline{Z}_{\mathrm{T}}(f) \approx \mathrm{j}\omega \underline{L}'_{\mathrm{m}}(f) \cdot \frac{1}{n_2} \tag{3.22}$$

Due to the inductive behavior at low frequencies, the HFCT gives a differential output signal that requires additional integration to obtain an output voltage proportional to the

measured primary current. Accordingly, the phase response shows plus 90° at such low frequencies.

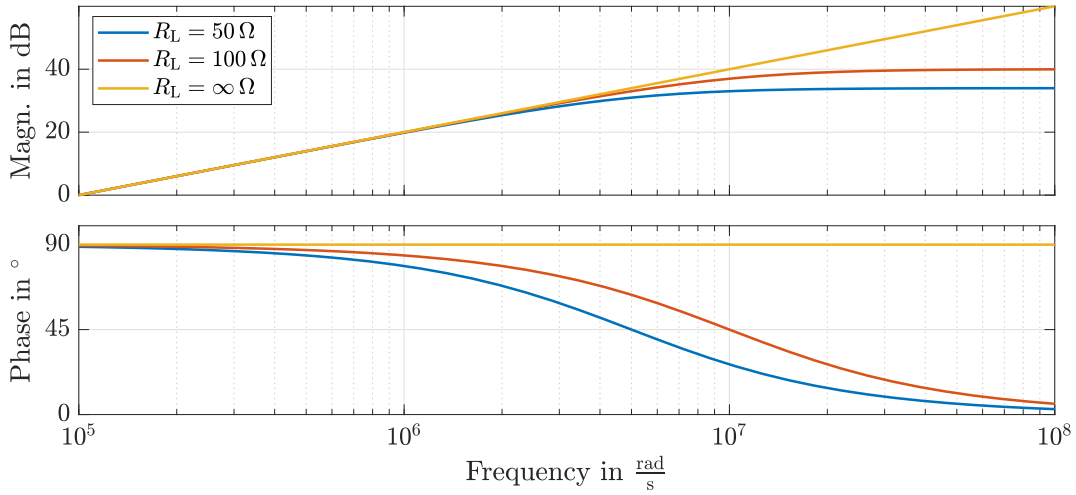

Figure 3.8: Bode plot using the transfer function of the ideal HFCT model (3.21). The behavior of the ideal HFCT is that of a high-pass filter. For the calculations, $n_2 = 3$, $L'_m = 10\,\mu\text{H}$, while R_L is varied.

At high frequencies, the HFCT behaves more like a resistor (see blue and red lines in Fig. 3.8). Then $j\omega\underline{L}'_m(f) \gg R_L$ holds and the transfer function (3.21) simplifies to:

$$\underline{Z}_T(f) \approx \frac{R_L}{n_2} \tag{3.23}$$

Due to the resistive behavior at high frequencies, the HFCT gives an output voltage that is proportional to the measured primary current (phase response is 0°).

Fig. 3.8 shows that the amplitude response is limited to the value of (3.23). In this way, the load resistor R_L flattens the frequency response of the HFCT at high frequencies. If the HFCT is operated with a high impedance $R_L \to \infty$ (open-circuit; see yellow line), it would behave like an inductance even in the HF range and the output voltage would theoretically rise to infinity (recall that the ideal model is studied at the moment, i. e., parasitic effects are neglected).

The load resistor is thus necessary to obtain a flat frequency response over a wide frequency range. Since the load resistance of most measuring devices is preset to $R_L = 50\,\Omega$, the amplitude of the plateau of the HFCT transfer function (3.23) depends mainly on the secondary winding number n_2. To achieve high HF sensitivity, the number of secondary turns n_2 thus has to be small.

Assuming a constant magnetizing inductance, the lower cut-off frequency of the high-pass (phase response is 45°) is determined by [26], [43]:

$$f_{\text{low}} = \frac{R_{\text{L}}}{2\pi L_{\text{m}}} \tag{3.24}$$

Since $R_{\text{L}} = 50\,\Omega$ is given, the lower limit of the HFCT bandwidth is determined only by the magnetizing inductance of the secondary coil, which in turn is proportional to the core permeability μ_{c} and n_2 (cf. to (3.11) on page 44).

In contrast to the ideal HFCT model, which behaves like a high-pass, the real HFCT behaves like a band-pass. This is partly due to the complex and frequency dependent magnetizing inductance $\underline{L}'_{\text{m}}(f)$ of the ferrite material, but mainly due to additional losses caused by the parasitic inductance $L_{\sigma,2}$ and capacitance C_{p} of the secondary winding. To study the influence of these parasitic elements on the HFCT transfer function, Fig. 3.9 shows some exemplary simulations using (3.20).

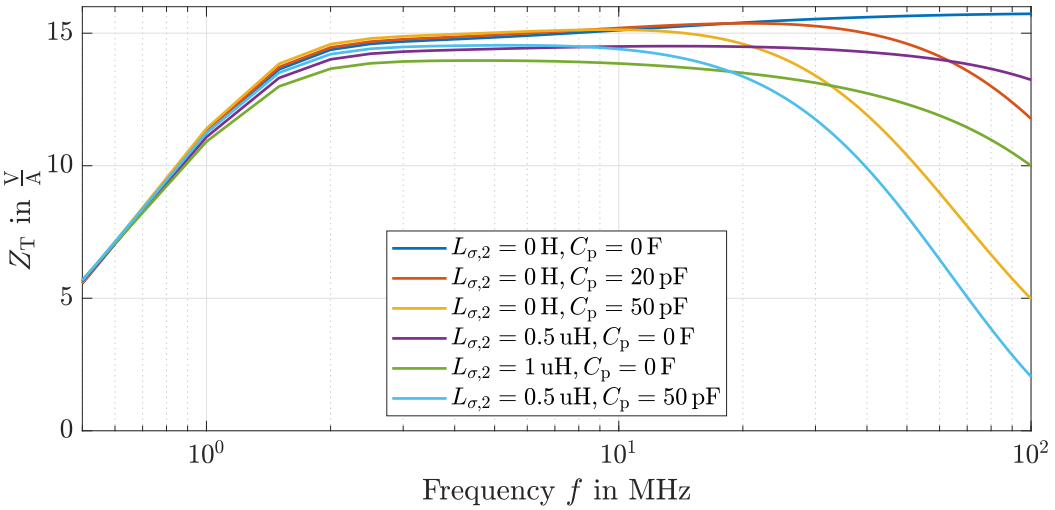

Figure 3.9: Impact of parasitic inductance $L_{\sigma,2}$ and capacitance C_{p} on the HFCT transfer function. The dark blue line neglects all parasitic losses (ideal HFCT model). The transfer functions are calculated with $R_{\text{L}} = 50\,\Omega$, $n_2 = 3$, and $\underline{L}'_{\text{m}}(f)$ is calculated according to (3.11) using the complex permeability of Fig. 3.5 and core sizes $r_{\text{c,in}} = 63.5\,\text{mm}$, $r_{\text{c,out}} = 102.6\,\text{mm}$, $h_{\text{c}} = 15.9\,\text{mm}$.

It can be seen that the parasitic capacitance C_{p} mainly determines the upper cut-off frequency of the band-pass (compare blue, red, and yellow lines), while the parasitic inductance $L_{\sigma,2}$ leads to a lower amplitude of the plateau (compare blue, purple, and green lines). A combination of both parasitic elements, as shown in the cyan curve, is probably closest to reality.

In the next section, a method for measuring the transfer impedance of an HFCT is presented. Then, the model is validated against measurements from various self-manufactured HFCTs.

3.4 Method for Measuring the Transfer Impedance

The developed HFCT model should be validated against measurements. Therefore, a method for measuring the transfer impedance of an HFCT is needed. For this purpose, the VNA described in Section 2.3.7 is used again. Any unsaturated HFCT can be interpreted as a linear electrical network with two ports. Accordingly, with a VNA it is possible to measure the scattering parameters $\boldsymbol{S}$ of an HFCT. The HFCT transfer function can then be calculated based on these measured $\boldsymbol{S}$ parameters.

Various example HFCTs are manufactured to validate the developed HFCT model. Different core materials and core sizes are chosen for these prototypes and the number of secondary turns n_2 is varied. An overview of the design parameters of all manufactured prototypes relevant to this thesis can be found in Table 3.1.

Table 3.1: Overview of the Self-Manufactured HFCT Sensor Prototypes.

Inventory Number	Material	Number of Sec. Turns n_2	Core Size in mm $r_{\mathrm{c,in}} \times r_{\mathrm{c,out}} \times h_{\mathrm{c}}$
01	No. 43 NiZn	3	$35.6 \times 61.0 \times 12.7$
02	No. 43 NiZn	4	$35.6 \times 61.0 \times 12.7$
03	No. 43 NiZn	5	$35.6 \times 61.0 \times 12.7$
05	No. 78 MnZn	3	$35.6 \times 61.0 \times 12.7$
06	No. 52 NiZn	3	$35.6 \times 61.0 \times 12.7$
07	No. 43 NiZn	3	$63.5 \times 102.6 \times 15.9$
08	No. 77 MnZn	3	$35.6 \times 61.0 \times 12.7$
10	No. 43 NiZn	2	$35.6 \times 61.0 \times 12.7$
12	No. 77 MnZn	5	$35.6 \times 61.0 \times 12.7$
13	No. 52 NiZn	2	$35.6 \times 61.0 \times 12.7$
14	No. 43 NiZn	3	$23.0 \times 35.6 \times 12.7$
15	No. 52 NiZn	4	$35.6 \times 61.0 \times 12.7$

The ferrite cores are all purchased from the manufacturer Fair-Rite. An exemplary prototype can be seen in Fig. 3.1a on page 38, which shows the self-made HFCT sensor No. 05 without housing.

To measure the transfer function, the HFCTs must be connected to the VNA. For better understanding, Fig. 3.10a shows a picture of the measurement setup.

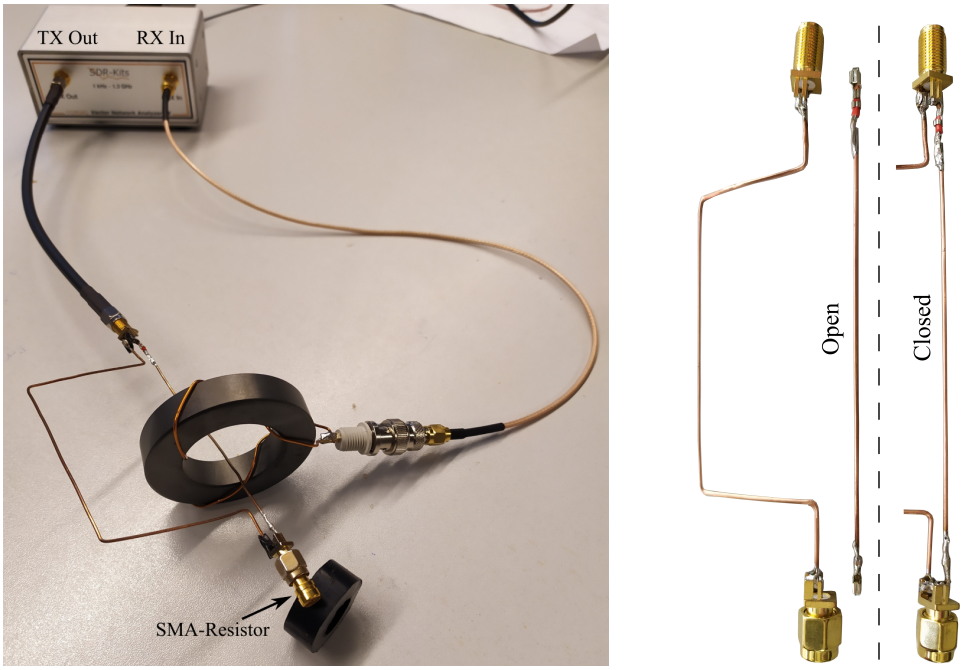

Figure 3.10: Left: Setup for measuring the transfer function of an HFCT using a VNA. Right: Adapter for coupling the TX signal of the VNA into the HFCT sensor, shown in open and closed state. All connections of the adapter are pluggable for easy installation around an HFCT.

The receive (RX) port of the VNA is connected to secondary winding of the HFCT to measure its output voltage. The signal from the transmit (TX) port of the VNA forms the input current of the HFCT. Since all wiring is made with shielded coaxial cables and no magnetic fields occur outside their shielding, the adapter circuit of Fig. 3.10b is required to couple the VNA signal into the HFCT. It is made of 1 mm thick copper wire and is used to separate the inner conductor and shielding of the coaxial cable from each other. The TX signal of the VNA is thus unshielded inside the adapter and can be coupled into the HFCT. All connections of the adapter are pluggable, so that it can be opened for installation around the HFCT. During the measurement, the adapter is terminated with the characteristic impedance of the coaxial cable (50 Ω) to avoid reflections on the line. The screwed-in resistor in SMA design can be seen at the bottom of Fig. 3.10a.

To ensure that the measurement setup (coaxial cables, adapter, etc.) does not influence the actual measurement, a calibration of the entire measuring circuit must be performed. This calibration is performed with the help of the VNA software before the actual measurements begin. For better understanding of the process, part of the calibration is shown in Fig. 3.11.

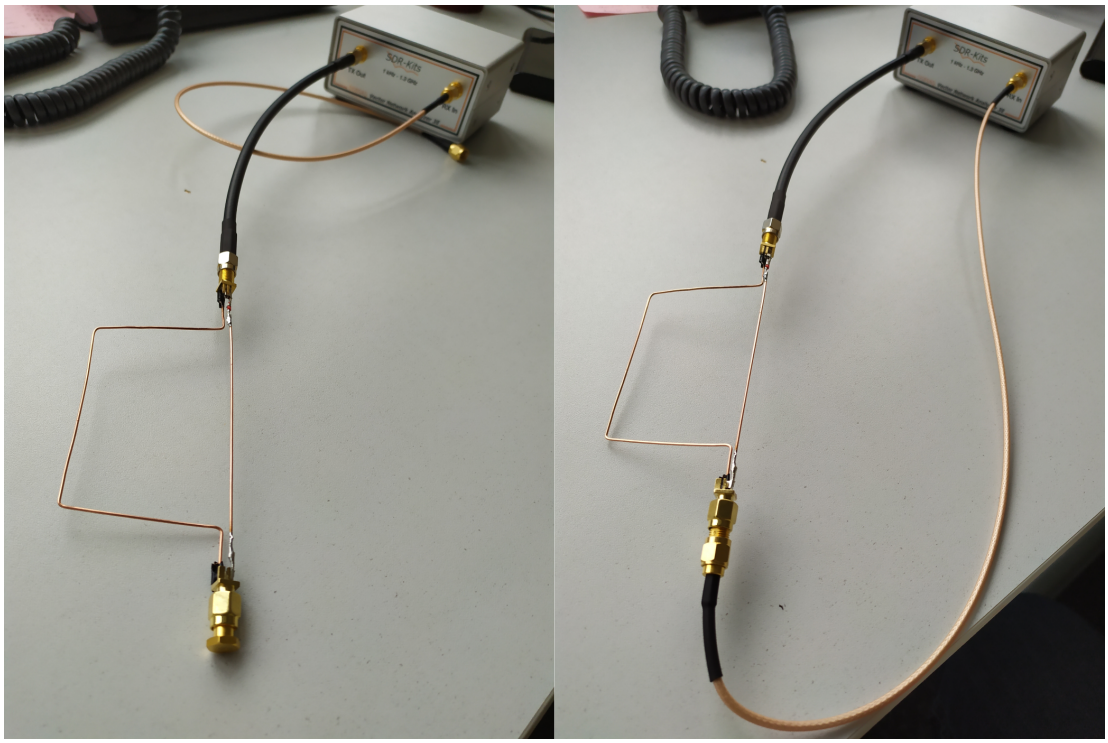

Figure 3.11: Setup for calibration. Short calibration is shown on the left and Through calibration on the right. For Short calibration, the corresponding short termination of an SMA calibration kit is screwed into the end of the adapter.

For calibration, the coaxial cables and the adapter are connected to the VNA, but without including an HFCT. Then, a SOLT-calibration (short, open, load, through) is performed with the help of the VNA software.

For short-circuit, open-circuit and load calibration the TX output is terminated accordingly, see Fig. 3.11 left. For this purpose, the corresponding parts of an SMA calibration kit are screwed into the end of the adapter. The SMA calibration kit used in this work is from the manufacturer Rosenberger. Detailed instructions on how to use the calibration kit and how to improve the calibration quality are included in the data sheet [59].

For the through calibration, TX and RX outputs are connected to each other, see Fig. 3.11 right. For this purpose, the output of the adapter is connected to the RX cable via an SMA female-to-female adapter, which is also part of the calibration kit. After successful calibration, the interferences of the measurement setup are compensated, so that only the HFCT behavior is measured precisely.

All measurements with the VNA are performed with a frequency sweep from 0.1 to 60 MHz to cover the entire HF range and a little above. At frequencies above 60 MHz, VNA calibration could no longer be performed with sufficient quality. However, this is

high enough since the expected signal bandwidth for PDs on power cables is expected to be less than 10 MHz. During the sweep the complex values $\underline{S}_{11}(f)$ and $\underline{S}_{21}(f)$ are measured and stored. The following equation can be used to calculate the HFCT transfer impedance:

$$Z_{\mathrm{T}}(f) = \left| \frac{\underline{S}_{21}(f) \cdot Z_{11}}{1 - \underline{S}_{11}(f)} \right| \tag{3.25}$$

where Z_{11} stands for the terminating impedance at the adapter. In our case the used resistor in SMA design has a resistance of $Z_{11} = 48.43\,\Omega$. This value should be measured as accurately as possible. The real value always slightly deviates from the nominal value of $50\,\Omega$.

As an alternative to the VNA measurement, the HFCT transfer impedance can also be measured directly with a sinusoidal signal generator and oscilloscope to obtain i_1 and u_{L}, see for example [50]. However, such measuring methods are only suitable for low frequencies, since the measuring circuit cannot be calibrated. This means that the measurement setup falsifies the results. For example, the parasitic inductance of the adapter leads to unwanted low-pass behavior. Accordingly, the measurement results are already distorted and unusable at frequencies of a few MHz. A properly calibrated VNA measurement is therefore always preferable.

3.5 HFCT Model Validation

The developed HFCT model is validated in this section using the self-manufactured prototypes. For this purpose, the simulated and measured transfer impedances $Z_{\mathrm{T}}(f)$ of the HFCTs are compared and presented. As it was not possible to accurately calculate/measure the parasitic inductance and capacitance of the HFCT prototypes, the simulations are calculated using the ideal HFCT model, where $L_{\sigma,2} = 0$ and $C_{\mathrm{p}} = 0$.

Fig. 3.12 shows the validation results for six selected HFCTs, which are a representative cross-section of all manufactured prototypes. The blue solid lines are the measured Z_{T} using the method from the previous Section 3.4. The red dashed lines are from simulations with the ideal HFCT model from Section 3.3.2. For the simulations, $\underline{Z}_{\mathrm{T}}$ is calculated according to (3.21) and its magnitude is plotted. The HFCTs shown are made of three different core materials, and the manufacturer's frequency recommendation is different for each material. Material No. 43 is recommended for frequencies of $f < 10\,\mathrm{MHz}$, material No. 52 for $f < 20\,\mathrm{MHz}$ and material No. 77 for $f < 1.5\,\mathrm{MHz}$ [54]. The x-axes in Fig. 3.12 are limited according to the manufacturer's frequency recommendation for the respective core material.

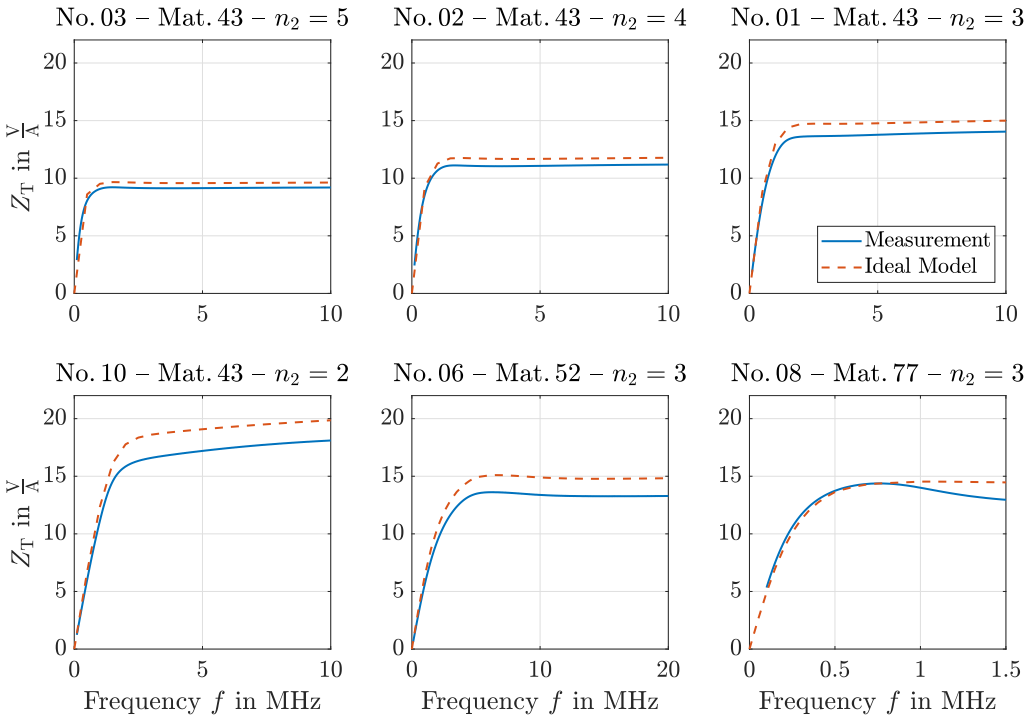

Figure 3.12: Comparison of the measured and calculated transfer impedance of six exemplary HFCT prototypes. The sensors are made of three different core materials from the manufacturer Fair-Rite and have a different number of secondary turns n_2.

Within the recommended frequency range, the Z_T prediction of the ideal model agrees well with the measurement. For the HFCT with core material No. 77, No. 43 and No. 52, the mean deviations for different secondary winding numbers can be found in Table 3.2. The numbers express the percentage by which the ideal HFCT model overestimates reality.

Table 3.2: Mean Deviation Between Simulation and Measurement.

	$n_2 = 5$	$n_2 = 4$	$n_2 = 3$	$n_2 = 2$
Material No. 77	2 %	–	2 %	–
Material No. 43	4 %	5 %	7 %	9 %
Material No. 52	–	8 %	10 %	13 %

A comparison of the different prototypes shows that the deviation between simulated and measured Z_T increases with decreasing secondary winding number n_2. It can also be seen that the deviation is greatest when material No. 52 is used and least when material No. 77 is used. Thus, the higher the usable bandwidth of the core material, the greater the overestimation error of the simulation. However, deviations of more than 10 % are only

to be expected for $n_2 < 3$, which is probably rarely the case. For $n_2 \geq 3$, the simulation results are close to the measured values. Accordingly, the model overestimation for most HFCT designs should be in the range of only a few percent.

At higher frequencies than shown in Fig. 3.12, the deviation between simulation and measurement increases with frequency, but this is irrelevant since the use of the materials in these frequency ranges is not recommended anyway. Above the recommended maximum bandwidth, magnetization losses in the core increase and the HFCT sensitivity would decrease (band-pass behavior).

The reason for the remaining deviation between simulation and measurement is due to the use of the ideal model. The two neglected parasitic parameters lead to an additional low-pass behavior. Their neglect is responsible for the remaining difference. Therefore, the ideal model overestimates the actual transfer impedance Z_T by a few percent. With this in mind, the ideal model can predict the achievable transfer impedance of an HFCT with sufficient accuracy.

3.6 Optimal HFCT Design

At the end of the previous chapter it was concluded that the bandwidth of most PD signals on power cables is < 10 MHz. For accurate PD measurements, an HFCT should therefore be sensitive within this frequency band. Of course, some of the PD reach higher bandwidths. However, measurement of the 0 – 10 MHz spectrum is also sufficient for their detection (neglecting higher frequency components only slightly reduces the measured PD amplitude – detection is still possible).

Therefore, in the following section, the developed HFCT model is used to find the optimal HFCT design for the measurement bandwidth of 0 – 10 MHz. To this end, the first three subsections investigate the influence of core material, secondary winding number, and core size on HFCT sensitivity. The best HFCT design, which has the highest sensitivity to detect PD on power cables, is then presented in Subsection 3.6.4.

3.6.1 Influence of Core Material

First, the influence of different core materials on the transfer impedance is investigated. Fig. 3.13 shows the measured sensitivities of HFCTs made of four different ferrite materials. For comparability, the secondary winding number for all four HFCT is $n_2 = 3$ and the size of their core is identical.

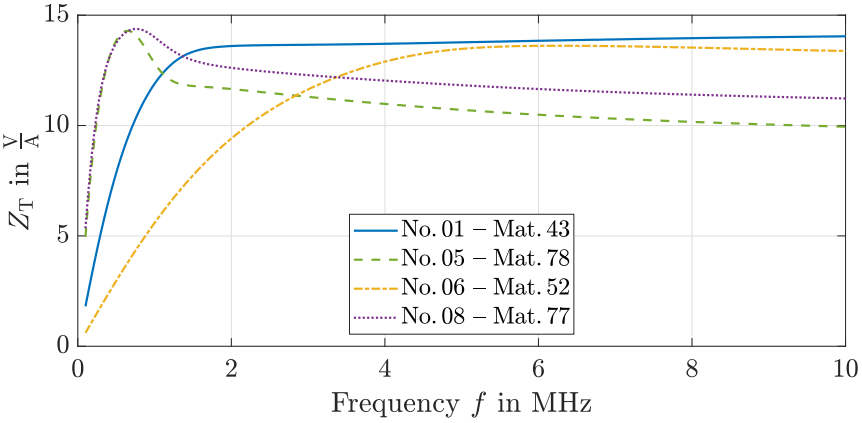

Figure 3.13: Comparison of different ferrite core materials. The secondary winding number is $n_2 = 3$ for all four HFCT shown. The cores are of equal size.

The core material has a great influence on the bandwidth of an HFCT. Each ferrite material has its own complex permeability, which determines the frequency response of the sensor. The measurement bandwidth of an HFCT is thus primarily determined by selecting the core material. Selection should be based on the manufacturer's recommended frequency range of the ferrite material (recommended bandwidth: No. 43 for $f < 10\,\text{MHz}$, No. 52 for $f < 20\,\text{MHz}$, No. 77/78 for $f < 1.5\,\text{MHz}$).

If no recommendation is given for the bandwidth, the rule of thumb is that the higher the initial permeability μ' at 0 Hz, the narrower the material bandwidth (Mat. 52: μ'=250; Mat. 43: μ'=800; Mat. 77: μ'=2000; Mat. 78: μ'=2300) [60]. Therefore, the lower the bandwidth of the signals to be measured, the higher the permeability of the core should be. Precise information on permeability is usually available in the data sheets.

The optimized PD sensor for power cables should be sensitive to frequencies $< 10\,\text{MHz}$. Of the materials tested here, material No. 43 seems to be the most suitable for this purpose. It produces a flat frequency response of the transfer impedance over the desired frequency band.

3.6.2 Influence of Secondary Winding Number

Second, the influence of the number of turns of the secondary winding n_2 on the transfer impedance is investigated. Fig. 3.14 shows the measured sensitivities of four HFCT made of the same core material No. 43. Their number of secondary turns varies between two and five. The toroidal core is the same size in all four prototypes.

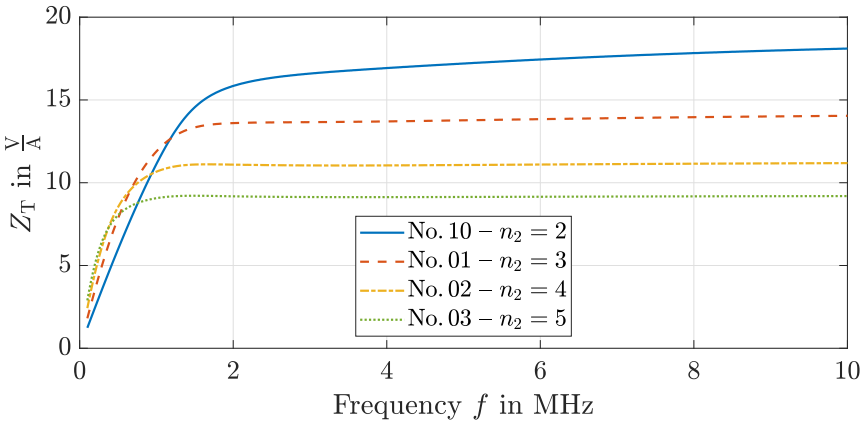

Figure 3.14: Comparison of different secondary winding numbers n_2. The cores of all four HFCT are made of material No. 43 and are the same size.

The secondary winding number has a great influence on the sensitivity of an HFCT. It can be seen that the fewer turns the secondary winding has, the higher the maximum sensitivity of the sensor (flat plateau). This behavior is reasonable because the maximum sensitivity is proportional to $\frac{1}{n_2}$ as can be seen in (3.23). On the other hand, according to (3.11), the magnetizing inductance of the HFCT is proportional to n_2 and thus the lower cut-off frequency (3.24) increases as the number of secondary turns decreases ($n_2 = 5$: 180 kHz; $n_2 = 4$: 250 kHz; $n_2 = 3$: 400 kHz; $n_2 = 2$: 800 kHz). This means that the measurement bandwidth is reduced from the lower end. Similar results were obtained by [12], [56]. For the optimized PD sensor, $n_2 = 3$ is a good compromise between maximum sensitivity and bandwidth.

3.6.3 Influence of Core Size

Third, the effect of core size on transfer impedance is investigated. Fig. 3.15 shows the measured sensitivities of HFCT from three different core sizes. All three are made of material No. 43 and the secondary winding number is $n_2 = 3$.

The core size has only a small influence on the bandwidth of an HFCT. According to (3.11), with a larger core, the magnetizing inductance of the HFCT and thus its sensitivity in the lower frequency range increases slightly, i. e., the lower cut-off frequency decreases as indicated by (3.24). This means that the measurement bandwidth of the HFCT widens downward with increasing core size. Similar results were obtained by [50]. However, the core size has only little effect on the transfer impedance of the sensor. Furthermore, the core size is usually predetermined by the diameter of the power cable, so it cannot be chosen arbitrarily. The core should be large enough for the primary conductor to fit

through, but not much larger or installation will be difficult. Furthermore, the larger the core, the heavier and more expensive the HFCT. For the optimized PD sensor, the large core of Fig. 3.15 is used. With an inner radius of $r_{c,in} = 63.5\,\text{mm}$ this core should fit around most power cables.

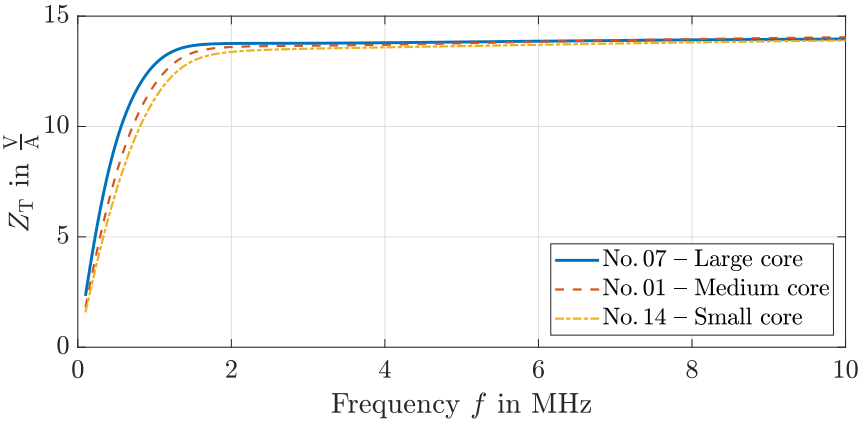

Figure 3.15: Influence of core size on the transfer impedance. The secondary winding number is $n_2 = 3$ for all three HFCT shown. The cores are made of material No. 43.

3.6.4 Optimized HFCT Design

The optimized HFCT can be seen in Fig. 3.16. It is built on a toroidal ferrite core with three windings on the secondary side. The core is made of a NiZn ferrite from the manufacturer Fair-Rite (material No. 43) with a size of $r_{c,in} = 63.5\,\text{mm}$, $r_{c,out} = 102.6\,\text{mm}$, $h_c = 15.9\,\text{mm}$. The output of the secondary winding can be connected to a measuring device via a BNC connector.

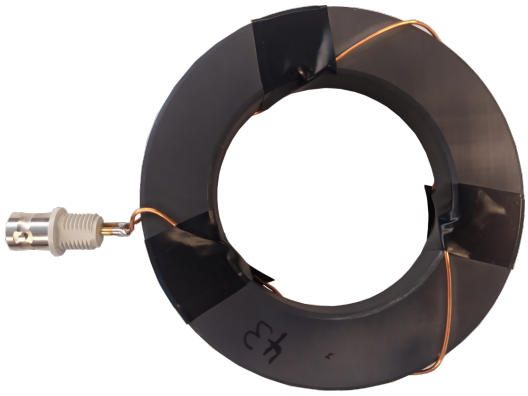

Figure 3.16: Optimized HFCT prototype for measuring PD on power cables. Secondary winding with three turns on a toroidal ferrite core made of Fair-Rite's No. 43 material.

The measured transfer impedance $Z_T(f)$ of the optimized HFCT can be seen in Fig. 3.17. Up to 10 MHz the frequency response is that of a high-pass with a lower cut-off frequency of 400 kHz. In the HF range, the transfer impedance is flat with a constant value of $Z_T \approx 14\,\Omega$.

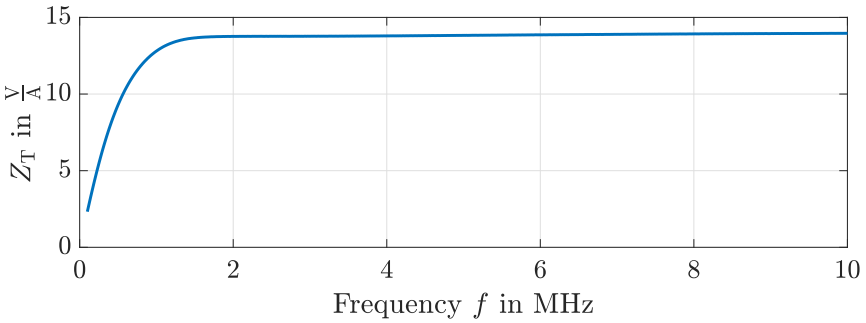

Figure 3.17: Measured transfer impedance of the optimized HFCT prototype. The ferrite core is free of saturation.

Additional shielding of the sensor is not required, since uniformly wound toroidal coils are inherently immune to magnetic interference fields [58]. Nevertheless, the sensor should be well suited for permanent outdoor installation. An insulating, waterproof housing should be provided for this purpose. Such a housing made of insulating material has almost no influence on the sensitivity of the sensor [50].

So far, only closed toroids have been considered as HFCT cores. A disadvantage of closed cores is that they cannot be installed without opening the electrical circuit of the primary conductor. In addition, they are prone to magnetic saturation, especially when used to monitor power cables online. For this reason, split-cores are used. With an air gap length of 0 mm, they have about the same sensitivity as a closed toroidal core. If the air gap length is increased, the saturation capability of the HFCT increases at the expense of sensitivity [12], [14]. The next chapter takes a detailed look at saturation and split-cores.

4 Dealing with Saturation when Using HFCTs for Online Monitoring of Power Cables

In the previous chapter, an HFCT with a measuring bandwidth of 10 MHz was developed to measure PD signals on power cables. The HFCT design was optimized under the assumption that the HFCT is free of saturation (linear operating mode). If only PD pulses are measured, this assumption is always fulfilled, since their signal amplitudes are weak (mA range). With online monitoring, however, the PD pulses are superimposed on the 50 Hz operating current of the power cables, which are in the range of several tens to hundreds of Amperes. During the PD measurement, the PD sensors are therefore exposed to strong magnetic fields caused by this operating current. Most HFCTs are less suitable for such online monitoring because the strong magnetic fields of the 50 Hz current drive them into magnetic saturation. At saturation, the HFCT is operated at all points of the nonlinear magnetization curve, so that the core permeability can no longer be assumed to be constant, but its nonlinearity must be considered. As a result, the shape of the measured output voltage no longer matches the original input current and accurate measurements are no longer possible. Therefore, saturation should be avoided as much as possible.

To avoid saturation during online PD monitoring and to ensure linear HFCT operation, air gaps are inserted into the ferrite core of the sensor. The longer the air gaps of such a split-core HFCT, the less prone it is to saturation [52]. This is common knowledge, but finding the optimal air gap length for a given HFCT design is a complicated task. It depends on both the material of the ferrite core (with nonlinear material properties) and the amplitude of the 50 Hz operating current of the power cable, which is not constant. If the air gap is too short, the saturation is not reduced sufficiently; if the air gap is too large, the sensitivity of the HFCT is unnecessarily reduced. There is no simple equation to calculate the optimal air gap length of a split-core HFCT, and almost no scientific literature on the subject has been published in high-quality peer-reviewed journals. Only [12], [52], [56] are partly related to the topic and show some experimental data for HFCTs at different air gaps. However, all of these measurements are only side results, and none of the publications focus on air gap optimization. Therefore, the optimal air gap length of the developed HFCT is determined experimentally in this chapter. Based on the results, an analytical split-core model is then derived and validated, which can be used to quickly calculate the optimal air gap length of any HFCT.

The chapter is structured as follows. In Section 4.1, it is shown what happens when an HFCT is used at saturation. Section 4.2 then presents the construction of split-core HFCTs. Subsequently, a method for quantifying the saturation level of an HFCT core is introduced in Section 4.3. Then, all measurements needed to experimentally determine

the optimal air gap length of a split-core HFCT are presented in Section 4.4. Finally, the analytical split-core model is derived and validated in Section 4.5. Parts of this chapter have been published in [49], [61].

4.1 Operation of HFCTs at Saturation

HFCTs are installed at power cables to detect PDs. However, the current in power cables is dominated by the 50 Hz operating current. These currents and their magnetic fields are usually strong enough to drive the HFCT core into saturation. At saturation, the HFCT is no longer operated only in the middle section of Fig. 3.4 and thus the permeability can no longer be assumed to be linear. Consequently, (3.7) and (3.8) are no longer applicable and the HFCT model from the previous chapter cannot be used anymore.

At saturation, linear measurements are no longer possible. For an exemplary 50 Hz operating current, this process is shown in detail in Fig. 4.1.

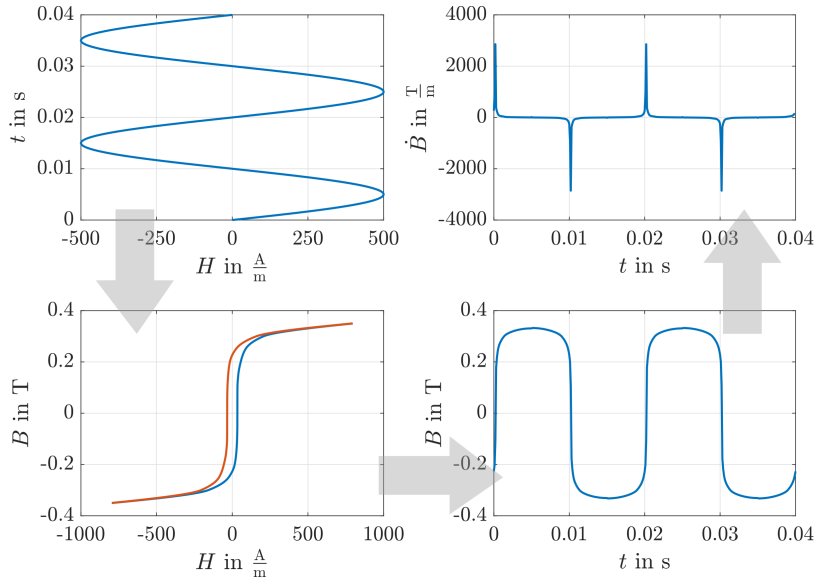

Figure 4.1: Due to the high 50 Hz current of the power cable (top left), the HFCT magnetization curve is operated in the nonlinear region. Therefore, the output voltage (proportional to $\dot{B}$) is distorted and not sinusoidal (top right).

Since the amplitude of the sinusoidal input field H is too high for linear HFCT operation, the nonlinear part of the magnetization curve is also processed. As a result, the magnetic flux density B in the ferrite core is non-sinusoidal. The current induced in the secondary winding of the HFCT is proportional to the derivative of B with respect to time $\dot{B}$.

Accordingly, the HFCT output signal contains voltage peaks (harmonic distortion [62]). Thus, due to nonlinearity, the shape of the measured HFCT output voltage u_L and the original input current i_1 no longer match (nonlinear measurement).

To show the influence of saturation on the developed HFCT prototype, measurements are performed. For this purpose, the experimental setup from Fig. 4.2 is used.

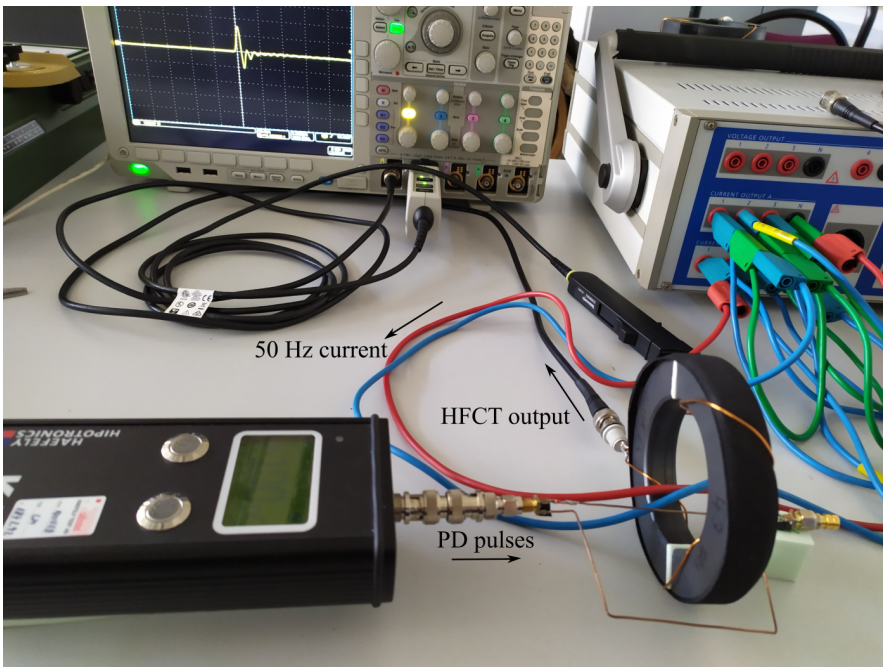

Figure 4.2: Experimental setup for most of the HFCT measurements in this chapter. A 50 Hz current generator and/or a PD generator are available to generate the HFCT input current i_1.

The HFCT is installed around three conductors. Two of them are connected to a 50 Hz current generator (Omicron CMC-256-6), which can generate currents with amplitude up to $I_{1,50\mathrm{Hz}} = 75\,\mathrm{A}$ RMS. The third conductor is connected to a PD calibrator (Haefely KAL9511) which generates realistic PD pulses of 100 pC. Both currents are simultaneously coupled by the HFCT and its output voltage u_L is measured using a wideband oscilloscope (Tektronix MDO4024C) with an input impedance of $R_L = 50\,\Omega$.

At first, only the 50 Hz current is increased to show the effect of core saturation. Fig. 4.3 shows the results for input currents with RMS values $I_{1,50\mathrm{Hz}}$ of 2, 10, and 50 A. At $I_{1,50\mathrm{Hz}} = 2\,\mathrm{A}$, the measured output voltage u_L is sinusoidal, which means that the input current is measured correctly (linear operation). As the current increases, the measured output voltage becomes more and more non-sinusoidal, i. e., its harmonic distortion

increases (nonlinear operation). This nonlinear measurement is caused by increasing core saturation.

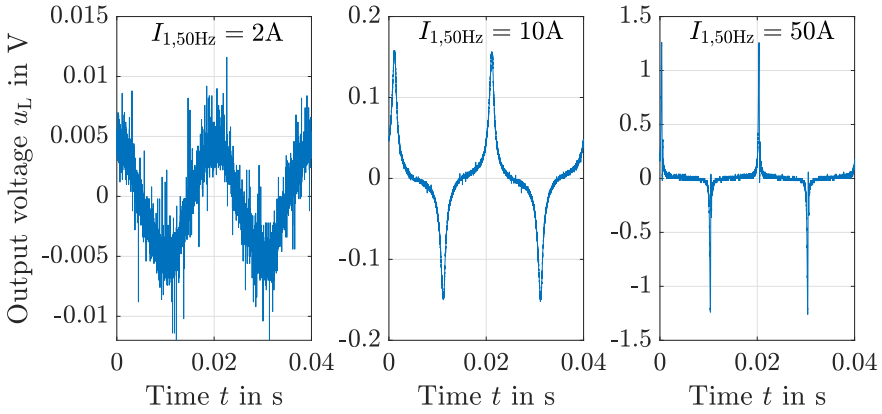

Figure 4.3: Output voltage of the HFCT prototype measured at increasing 50 Hz input current with RMS values of 2, 10, and 50 A.

The starting point for nonlinear measurements depends on the selected core material. For ferrite material No. 43, nonlinear operation starts at about $I_{1,50Hz} > 2.5$ A. The higher the 50 Hz input current, the higher the level of core saturation, and the amplitude of the output voltage peaks increases. These voltage peaks not only falsify the measurement results, but can also potentially damage the electronics connected to the HFCT output.

Next, the effect of core saturation on PD measurements should be shown. For this purpose, the HFCT measures 100 pC PD pulses, while at the same time the amplitude of the superimposed 50 Hz current is continuously increased. The measurement results are shown in Fig. 4.4.

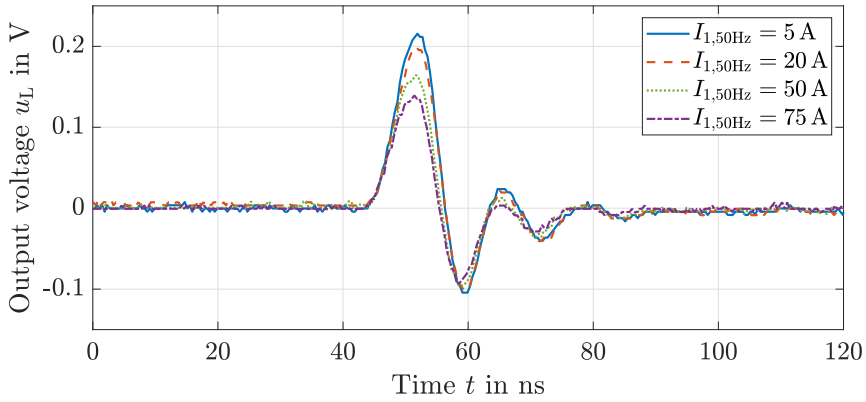

Figure 4.4: HFCT measurements of a 100 pC PD signal. At the same time, an increasing 50 Hz current is superimposed on the PD pulses to saturate the sensor.

It can be clearly seen that the sensitivity of the HFCT decreases with increasing core saturation. A sensitivity loss cannot be accepted since the weak PD signals are difficult to detect anyway. Saturation must therefore be avoided as much as possible to ensure maximum PD sensitivity.

4.2 Advanced HFCT Prototype with Split-Core

The measurements of Fig. 4.3 prove that the developed HFCT is not yet suitable for online monitoring of power cables. Saturation must be avoided for all operating currents of a power cable, not only for $I_{1,50\mathrm{Hz}} < 2.5\,\mathrm{A}$. The most common method to increase the saturation capability of an HFCT is to insert air gaps into the ferrite core [52]. Thus, to improve the HFCT prototype, its core is split in half to create two air gaps. The modified split-core HFCT can be seen in Fig. 4.5. The length of each air gap d_{air} can be adjusted as desired by inserting plastic pieces of different thickness (plastic has about the same permeability as air).

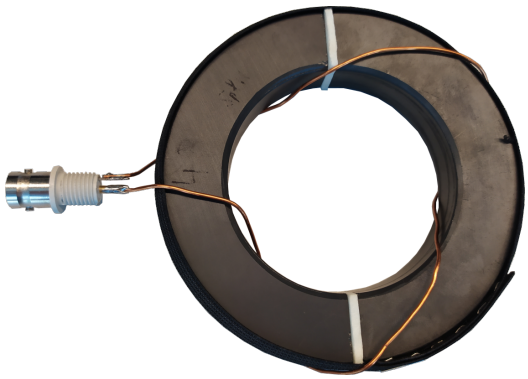

Figure 4.5: Improved HFCT prototype. This is the same sensor as in Fig. 3.16, but with a split-core. The two halves of the core are held together with a rubber band.

Inserting an air gap changes the magnetization curve of the HFCT ferrite core, as shown in Fig. 4.6. The figure shows *B*-*H* measurements of the split-core HFCT at increasing air gap length. The input current i_1 for the measurements is set again to a 50 Hz sine.

It can be seen that the magnetization curves are stretched as the air gap length d_{air} increases. Accordingly, saturation sets in at higher i_1, i. e., the magnetic flux density B_{Sat} at which saturation starts now requires a higher input field H_{Sat}. This means that the HFCT can be operated at higher 50 Hz currents without core saturation. It can also be seen that the longer the air gap, the more linear the magnetization curve (hysteresis becomes negligible). This ensures linear operation of the HFCT even at high 50 Hz input currents.

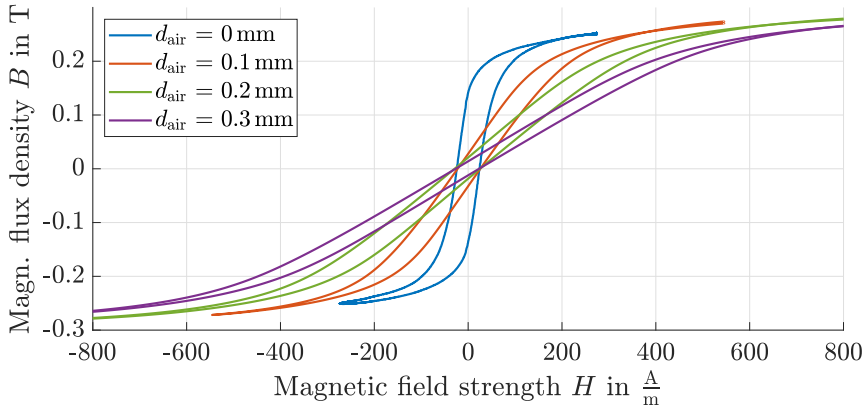

Figure 4.6: Influence of an air gap d_{air} on the magnetization curve of the HFCT. Due to the air gap, the curve is stretched and saturation sets in at higher H. For clarification: d_{air} = 0.1 mm means that each of both air gaps has a length of 0.1 mm.

On the other hand, it can be seen that the slope of the linear part of the magnetization curve, and thus the permeability $\mu_{c,lin}$, decreases due to the air gap. According to (3.24), the lower cut-off frequency of the HFCT transfer function increases with decreasing core permeability. Consequently, the bandwidth of the HFCT band-pass becomes narrower from the lower end. A loss of bandwidth results in a loss of sensitivity, which can be seen in Fig. 4.7. For this figure, the split-core HFCT is used to measure 100 pC PD pulses while continuously increasing the length of its air gap.

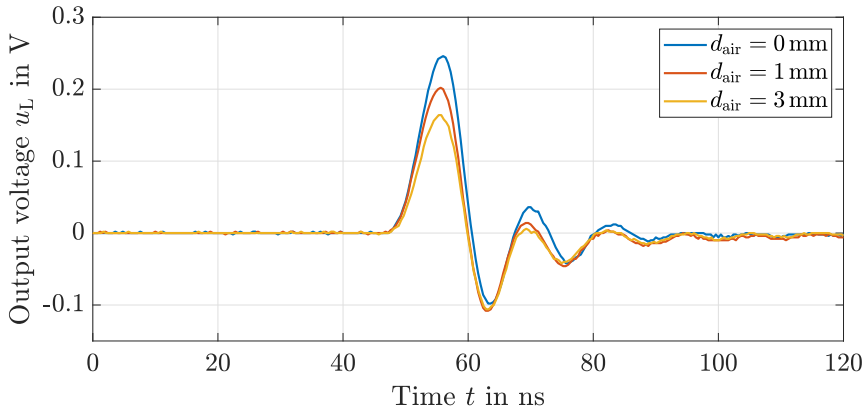

Figure 4.7: Measurement of a 100 pC PD pulse with the split-core HFCT while the length of its air gaps d_{air} is increased. With increasing air gap length, the PD sensitivity decreases. The 50 Hz current is switched off for this measurement, $I_{1,50Hz}$ = 0 A.

Thus, increasing the air gap length leads to less core saturation, but at the expense of PD sensitivity [12]. The air gap should therefore be as long as necessary to avoid saturation, but as short as possible.

4.3 Calculation of the Level of Core Saturation

Since harmonic distortion increases with core saturation, calculating the total harmonic distortion (THD) of the measured HFCT output voltage u_L is a good measure for determining the saturation level of its core. If the output voltage is sinusoidal, the THD approaches 0, which means the HFCT core is free of saturation. To calculate the THD, the Fourier transform of the measured voltage must first be calculated, i. e., $u_\mathrm{L}(t) \overset{\mathcal{F}}{\longrightarrow} \underline{U}_\mathrm{L}(f)$. Then the THD value can be calculated as follows [63]:

$$\mathrm{THD} = \frac{|\underline{U}_{\mathrm{L},2}|^2 + |\underline{U}_{\mathrm{L},3}|^2 + \cdots |\underline{U}_{\mathrm{L},25}|^2}{|\underline{U}_{\mathrm{L},1}|^2} = \frac{\sum_{i=2}^{\mathrm{n}=25} |\underline{U}_{\mathrm{L},i}|^2}{|\underline{U}_{\mathrm{L},1}|^2} \tag{4.1}$$

where $\underline{U}_{\mathrm{L},i}$ is the i^{th} harmonic (150 Hz, 250 Hz, ...) and $\underline{U}_{\mathrm{L},1}$ is the fundamental component of the HFCT output voltage spectrum (50 Hz). The THD calculation is performed only up to the 25^{th} harmonic ($f_{25} = 2450$ Hz) to suppress the influence of the omnipresent measurement noise on the the result. Such high-frequency noise can be seen, for example, in Fig. 4.3 at 2 A on the left. For a given split-core HFCT, the THD value depends on both the amplitude of the 50 Hz input current and the air gap length, $\mathrm{THD} = f(I_{1,50\mathrm{Hz}}, d_\mathrm{air})$.

Applying (4.1) to the measured output voltages $u_\mathrm{L}(t)$ of Fig. 4.3 gives the following THD values:

$$\begin{aligned}\mathrm{THD}(2\,\mathrm{A}, 0\,\mathrm{mm}) &= 0.0077\\ \mathrm{THD}(10\,\mathrm{A}, 0\,\mathrm{mm}) &= 0.3129\\ \mathrm{THD}(50\,\mathrm{A}, 0\,\mathrm{mm}) &= 2.3985\end{aligned}$$

It can be seen that the THD content increases with the amplitude of the 50 Hz operating current. Recall, that the measurements are recorded with an HFCT made of ferrite material No. 43, which starts to saturate at 50 Hz currents of about $I_{1,50\mathrm{Hz}} > 2.5$ A. The calculated THD value for currents $I_{1,50\mathrm{Hz}} \leq 2.5$ A is approximately 1 % or less. Ideally, the THD value would drop to 0, but this is unrealistic due to possible harmonics in the 50 Hz current of the power cable and the omnipresent measurement noise. For the laboratory environment of this thesis, 1 % is a good threshold to clearly detect saturation while ensuring sufficient robustness against noise. Accordingly, in this thesis, linear HFCT operation is defined by $\mathrm{THD} \leq 0.01$, and values above 1 % indicate nonlinear HFCT operation. This threshold applies to HFCTs made of all ferrite materials and is not unique to material No. 43 of the example measurements.

4.4 Experimental Determination of the Optimal Air Gap Length

The effect of different air gap lengths on the HFCT output voltage u_{L} can be seen in Fig. 4.8. For this figure, the 50 Hz input current is set to $I_{1,50\mathrm{Hz}} = 100\,\mathrm{A}$. Then, the air gap length of the split-core is increased.

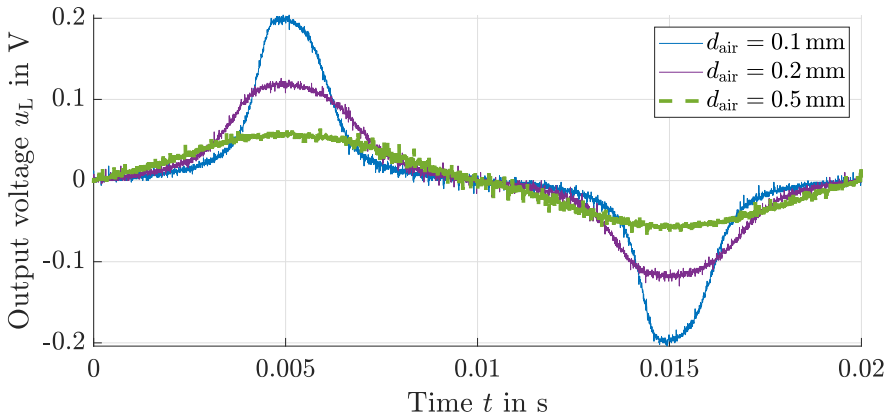

Figure 4.8: Output voltage of the split-core HFCT measured at a constant 50 Hz input current of $I_{1,50\mathrm{Hz}} = 100\,\mathrm{A}$ while increasing the length of its air gap d_{air}.

It can be clearly seen that the level of core saturation decreases as the air gap length d_{air} increases, which can be seen from the fact that the measured HFCT output voltage u_{L} becomes more and more sinusoidal. At $d_{\mathrm{air}} = 0.5\,\mathrm{mm}$, the core is free of saturation, i. e., u_{L} is a sine.

This can be confirmed by calculating the THD of the measurements according to (4.1):

$$\begin{aligned}\mathrm{THD}(100\,\mathrm{A}, 0.1\,\mathrm{mm}) &= 0.553\\ \mathrm{THD}(100\,\mathrm{A}, 0.2\,\mathrm{mm}) &= 0.162\\ \mathrm{THD}(100\,\mathrm{A}, 0.5\,\mathrm{mm}) &= 0.01\end{aligned}$$

At a 50 Hz current of $I_{1,50\mathrm{Hz}} = 100\,\mathrm{A}$, an air gap length of $d_{\mathrm{air}} = 0.5\,\mathrm{mm}$ (on both sides) is required to avoid saturation (based on the 1 % criterion), i. e., until the output voltage is sinusoidal. In other words, at an operating current of 100 A, the optimal air gap length is 0.5 mm on both sides.

In the same way, the optimal air gap length $d_{\mathrm{air,opt}}$ can be determined at various other 50 Hz currents. For this purpose, the input current of the HFCT is varied between 2 – 600 A RMS and the air gap length between 0 – 3 mm on each side. The THD of the HFCT output voltage u_{L} is then calculated for all measurements according to (4.1). The results are shown in Fig. 4.9.

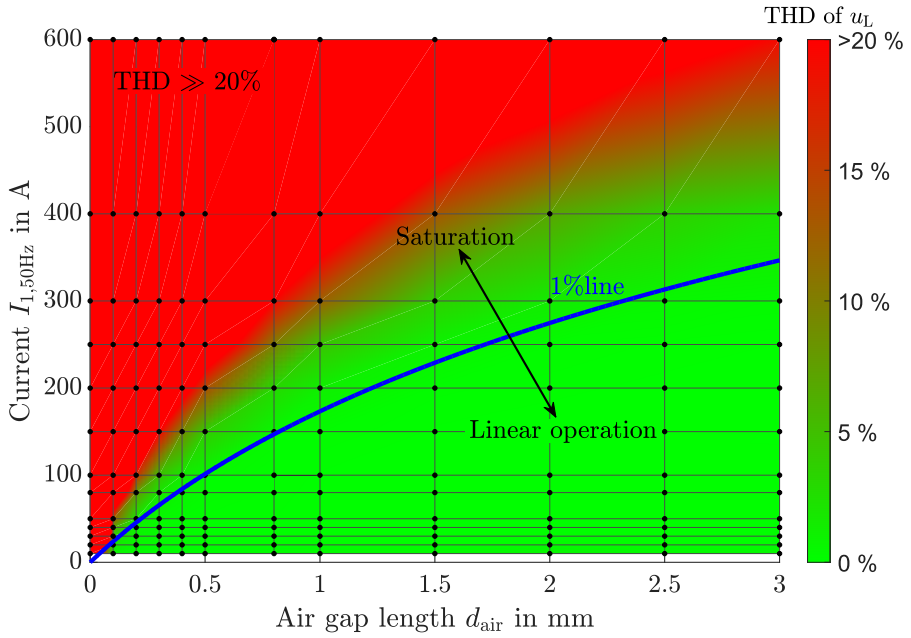

Figure 4.9: THD value of the measured output voltage of the split-core HFCT at various air gap lengths and input currents. The 1 %-line marks the minimum air gap that ensures linear operation. Although the scale of the z-axis is limited to 20 %, the THD value increases continuously towards the upper left corner. The dots mark the individual measurements.

It can be seen that the higher the 50 Hz input current, the higher the THD of the HFCT output voltage u_L due to saturation. It can also be seen that the air gap has a positive influence on the THD value. The longer the air gap, the later the HFCT enters saturation mode (based on the 1 % criterion). For example, an air gap of $d_{air} = 3$ mm ensures linear operation up to a 50 Hz current of about 350 A, while with an air gap of 1 mm saturation already starts at about 170 A. Thus, as expected, with increasing air gap length, the HFCT can withstand higher 50 Hz currents without leaving its linear mode of operation.

The 1 %-line marks the border between the two modes, i. e., the minimal air gap length to ensure linear HFCT operation. Since the air gap should only be as long as necessary, the minimum air gap length is equal to the optimal air gap length $d_{air,opt}$. The optimal length depends on the 50 Hz input current and on the core material of the HFCT. For material No. 43 of the HFCT split-core used, the 1 %-line can be fitted to the following mathematical function:

$$d_{air,opt}\left(I_{1,50Hz}\right) = e^{\frac{I_{1,50Hz}}{250}} - 1 \tag{4.2}$$

If the 50 Hz operating current of the power cable on which the HFCT is installed is known, this function can be used to optimally set its air gap. However, the operating

current of a power cable is usually not constant over time, but varies between 0 and a maximum permissible value $I_{1,50\text{Hz,max}}$. Accordingly, $d_{\text{air,opt}}$ is not constant, but varies with the load of the power cable. Setting the air gap based on the maximum permissible current of the power cable is also not a good idea, as the air gap would be unnecessarily large at any lower current (sensitivity loss).

To further investigate the influence of the air gap on HFCT sensitivity, the PD measurements shown in Fig. 4.7 have been extended to various 50 Hz currents and air gap lengths. For this purpose, the HFCT measures 100 pC PD pulses, while the 50 Hz input current is varied between 2 – 75 A RMS and the air gap length between 0 – 3 mm on each side. The measurement results are shown in Fig. 4.10. The amplitude of the measured PD pulse $\hat{u}_{\text{L}}(t)$ is plotted on the z-axis, normalized to the measured PD amplitude at 0 mm and 0 A (offline measurement value). The optimum air gap length function of the split-core HFCT from (4.2) is plotted along with the measurements (blue line).

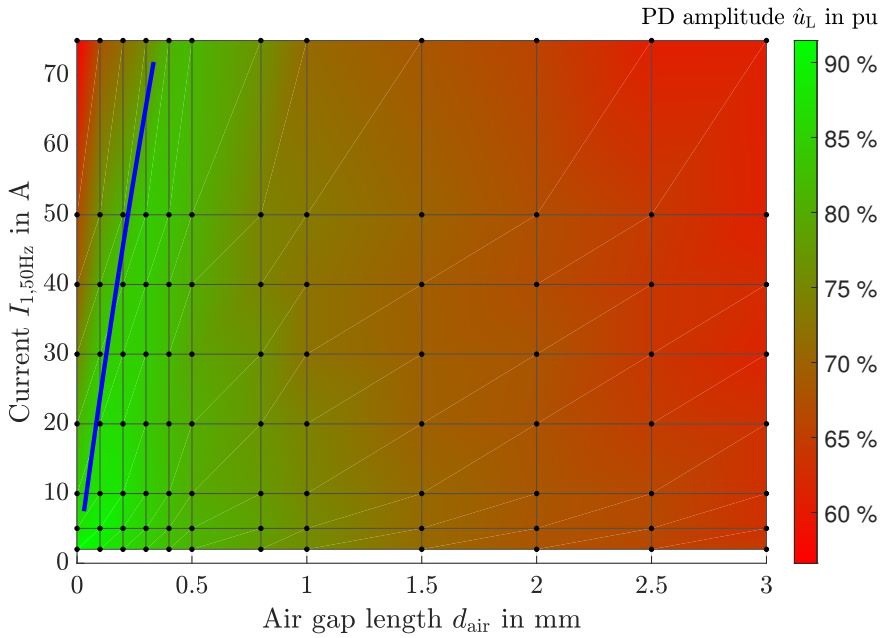

Figure 4.10: PD measurements with the split-core HFCT at various air gap lengths and 50 Hz currents. The PD amplitude of the measured HFCT output voltage $u_{\text{L}}(t)$ has been normalized and plotted on the z-axis. The blue line is the optimal air gap length function of the HFCT according to (4.2).

It can be seen that the maximum HFCT sensitivity is always reached near the blue line. If the air gap is shorter than the optimum, the sensitivity of the HFCT decreases sharply as it is operated under saturation. If the air gap is longer than the optimum, the sensitivity also decreases, but more slowly (unnecessarily large air gap). The air gap length should therefore always be close to the optimal length for maximum PD sensitivity.

4.5 Analytical Split-Core HFCT Model for Calculating the Optimal Air Gap Length

The experimental determination of the optimal air gap length function of a given HFCT, as demonstrated in Fig. 4.9, is very time consuming (more than 200 individual measurements are required for each core material). To speed up this process, this section derives an analytical split-core HFCT model to simulate the optimal air gap length function of HFCTs with cores of any ferrite material. The model is derived in the first Subsection 4.5.1 and validated in the following Subsection 4.5.2.

4.5.1 Derivation of the Split-Core HFCT Model

The split-core model is derived based on the magnetization curve of the ferrite material used. Fig. 4.11 shows the B-H curve of ferrite material No. 43 measured at input currents with RMS values $I_{1,50\mathrm{Hz}}$ of 2, 5, 20 and 50 A. All four magnetization curves are recorded at a frequency of 50 Hz and at an air gap length of 0 mm.

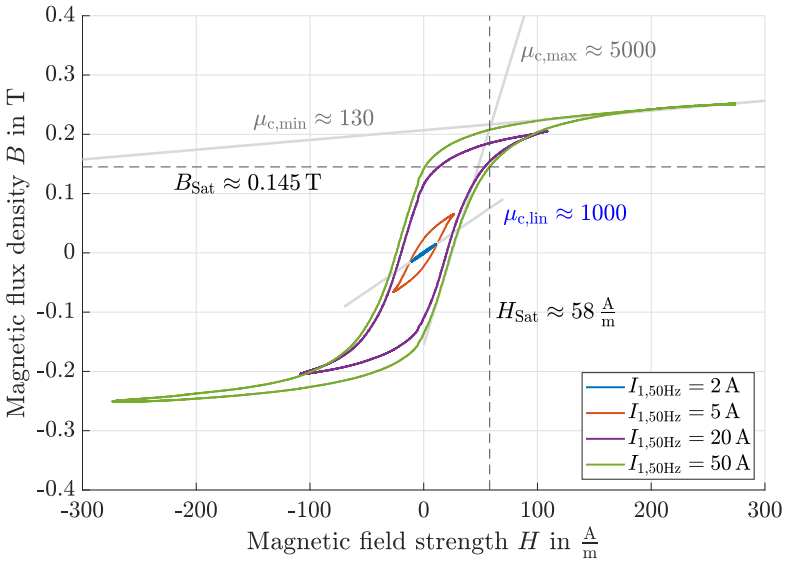

Figure 4.11: Magnetization curve of ferrite material No. 43, which is used for the HFCTs developed in this work. The curves are recorded at various 50 Hz input currents. The intersection of the tangents of the maximum $\mu_{\mathrm{c,max}}$ and minimum $\mu_{\mathrm{c,min}}$ permeability marks the saturation point H_{Sat} of the ferrite material.

It can be seen that the magnetization curve is linear at $I_{1,50\mathrm{Hz}} = 2\,\mathrm{A}$ with a permeability of $\mu_{\mathrm{c,lin}} \approx 1000$ (equivalent to offline measurement). From about $I_{1,50\mathrm{Hz}} = 2.5\,\mathrm{A}$ the curve becomes increasingly nonlinear due to hysteresis. At currents $I_{1,50\mathrm{Hz}} > 15\,\mathrm{A}$ or

$H > H_{\mathrm{Sat}}$, the second stage of nonlinearity due to saturation begins. At this point, the core material is saturated, and further increase of the exciting magnetic field H only slightly increases the magnetic flux density B in the core. After the saturation point H_{Sat}, the permeability thus decreases rapidly. The saturation point of the B-H-curve can be found by the intersection of the tangents of the maximum $\mu_{\mathrm{c,max}}$ and minimum $\mu_{\mathrm{c,min}}$ permeability, which marks the level of H_{Sat}. If the core is not driven to saturation, the permeability reaches high values. The magnetic flux density at saturation B_{Sat} is material-specific and constant. For the ferrite material No. 43 of the developed HFCT, it is about 0.145 T.

When the air gap length of a split-core is increased, the magnetization curve becomes more linear and saturation becomes the main source of nonlinearity (see Fig. 4.6). For the following model, it is therefore assumed that the influence of hysteresis as a source of nonlinearity is negligible.

Under this assumption, the saturation point is equal to the point where nonlinear operation starts. For input fields between 0 and H_{Sat}, linear HFCT operation with constant permeability can be assumed accordingly (cf. linear approximation of Fig. 3.4 on page 41). This linear model permeability $\mu_{\mathrm{c,mod}}$ is determined only by the saturation point of the core material. Using the measurements from Fig. 4.11 and (3.3), the following value is calculated for the ferrite material No. 43:

$$\mu_{\mathrm{c,mod}} = \frac{B_{\mathrm{Sat}}}{H_{\mathrm{Sat}}(0\,\mathrm{mm})\mu_0} = \frac{0.145\,\mathrm{T}}{58\,\frac{\mathrm{A}}{\mathrm{m}} \cdot \mu_0} \approx 2000 \tag{4.3}$$

The magnetization curve used to determine $\mu_{\mathrm{c,mod}}$ should be measured at a frequency of 50 Hz, since saturation can only be expected at this frequency.

The further HFCT model is based on the ideas of the magnetic circuit theory (applicable when the core permeability is constant, as assumed for $\mu_{\mathrm{c,mod}}$). According to this theory, each material has a certain reluctance R_{M} that determines the magnetic flux Φ in that material. If there are different materials in a magnetic circuit, their reluctance can be combined. The total reluctance then determines the magnetic flux in the circuit.

A split-core HFCT forms a magnetic circuit consisting of two different materials in series, the split ferrite core and the two air gaps (since the permeability of the copper of the secondary winding is close to that of air $\mu_{\mathrm{co}} \approx 1$, its influence on the magnetic circuit is negligible). The reluctance of the ferrite core can be calculated as follows [52]:

$$R_{\mathrm{M,c}} = \frac{l_{\mathrm{c}}}{\mu_0 \mu_{\mathrm{c,mod}} A_{\mathrm{c}}} \tag{4.4}$$

where $\mu_{c,mod}$ is the linear model permeability of (4.3). A_c is the cross-section of the toroid and l_c is its magnetic path length. This length corresponds to the mean core length:

$$l_c = (r_{c,Out} + r_{c,In}) \cdot \pi \tag{4.5}$$

The reluctance of the air gaps is calculated in a similar way [52]:

$$R_{M,air}(d_{air}) = \frac{2\,d_{air}}{\mu_0 A_{air}} = \frac{2\,d_{air}}{\mu_0 A_c k_{FF}(d_{air})} \tag{4.6}$$

where $2\,d_{air}$ accounts for the total air gap length of both air gaps of the split-core. A_{air} is the cross-section of the air gaps, i. e., the area where the magnetic flux is located in the air gap.

When calculating the air gap reluctance, the fringing flux phenomenon must be considered. Each air gap in a magnetic circuit is a source of fringing flux. Fringing means that the magnetic flux spreads not only across the cross-section of the core, but also in the adjacent volume outside the core. The effective cross-section of the air gap A_{air} is therefore not equal to the core cross-section A_c but increases due to fringing flux. Accordingly, the reluctance of the air gap decreases compared to the fringing-flux-free state, i. e., the fringing flux 'shortens' the air gap. To account for this phenomenon, a fringing flux factor can be calculated [52]:

$$k_{FF}(d_{air}) = 1 + \frac{2\,d_{air}}{\sqrt{A_c}} \ln\left(\frac{2\,r_{c,in}}{d_{air}}\right) \tag{4.7}$$

This factor depends only on the length of the air gap. Without air gap, k_{FF} is equal to 1 and increases with the air gap length.

The total reluctance of the split-core HFCT is the sum of the split-core and air gap reluctance:

$$R_{M,tot}(d_{air}) = R_{M,c} + R_{M,air}(d_{air}) \tag{4.8}$$

The ferrite material has a high permeability and therefore a low reluctance. In comparison, the air gap reluctance is very high even for small air gap lengths, $R_{M,air} \gg R_{M,c}$. Thus, controlling the air gap is equivalent to controlling the overall HFCT reluctance.

Using the following approach, an effective permeability $\mu_{c,eff}$ can be defined for the magnetic circuit of the split-core HFCT:

$$R_{M,tot}(d_{air}) = \frac{1}{\mu_0 A_c}\left(\frac{l_c}{\mu_{c,mod}} + \frac{2\,d_{air}}{k_{FF}(d_{air})}\right) \stackrel{!}{=} \frac{l_c + 2\,d_{air}}{\mu_0 \mu_{c,eff}(d_{air}) A_c} \tag{4.9}$$

Solving (4.9) for the effective permeability:

$$\mu_{\mathrm{c,eff}}(d_{\mathrm{air}}) = \frac{l_{\mathrm{c}} + 2\,d_{\mathrm{air}}}{\frac{l_{\mathrm{c}}}{\mu_{\mathrm{c,mod}}} + \frac{2\,d_{\mathrm{air}}}{k_{\mathrm{FF}}(d_{\mathrm{air}})}} \tag{4.10}$$

The effective permeability describes the field enhancement in the HFCT core according to (3.3) at different air gap lengths.

The larger the air gap, the later B_{Sat} is reached, compare Fig. 4.6. Since the magnetic flux density for core saturation B_{Sat} is constant and known for a given material, the corresponding maximum input field H_{Sat} at which linear operation is still guaranteed can now be calculated using the effective permeability:

$$H_{\mathrm{Sat}}(d_{\mathrm{air}}) = \frac{B_{\mathrm{Sat}}}{\mu_0 \mu_{\mathrm{c,eff}}(d_{\mathrm{air}})} \tag{4.11}$$

With (3.1), this gives a relationship between $I_{1,50\mathrm{Hz}}$ and d_{air}:

$$I_{1,50\mathrm{Hz}}(d_{\mathrm{air}}) = H_{\mathrm{Sat}}(d_{\mathrm{air}}) \cdot 2\pi r_{\mathrm{c}} \tag{4.12}$$

The result corresponds to the maximum input current at which linear HFCT operation is ensured as a function of the air gap length. The inverse function $d_{\mathrm{air}}(I_{1,50\mathrm{Hz}})$ is equal to the optimal air gap length function of the HFCT.

4.5.2 Validation of the Split-Core HFCT Model

To validate the developed split-core HFCT model, the optimal air gap length functions of three different HFCTs are calculated according to (4.12) and compared to measurements. The design of all three HFCTs is the same as in Fig. 4.5, but with cores made of different ferrite materials. The shape and size of all three ferrite cores is identical.

To use the split-core model with HFCTs made of other ferrite cores, only their magnetization curve at $d_{\mathrm{air}} = 0\,\mathrm{mm}$ needs to be known. For this purpose, the measurements from Fig. 4.11 need to be made for the other two HFCTs to determine B_{Sat} and H_{Sat} of their ferrite core. Then, $\mu_{\mathrm{c,mod}}$ can be calculated according to (4.3). After this, the optimal air gap length function of the split-core can be easily calculated.

The first HFCT is that of ferrite material No. 43, whose optimal air gap length function is given in (4.2). The simulation is based on the magnetization curve of this material, which is shown in Fig. 4.11 on page 69.

The second HFCT consists of a ferrite material suitable for the HF range, but of unknown origin. The magnetization curve of this material is shown in Fig 4.13 on page 75 for an air gap of 0 mm. The simulation results are compared to the measurements shown in Fig. 4.14. The optimal air gap length function of this HFCT is obtained from these measurements and is as follows:

$$d_{\mathrm{air,opt}}(I_{1,50\mathrm{Hz}}) = \mathrm{e}^{\frac{I_{1,50\mathrm{Hz}}}{330}} - 1 \tag{4.13}$$

The core of the third HFCT is made of material No. 78 from the manufacturer Fair-Rite, which is a MnZn ferrite and is more suitable for lower frequencies $< 1.5\,\mathrm{MHz}$. The magnetization curve of this material is shown in Fig. 4.15 on page 76 for an air gap of 0 mm. The simulation results are compared to the measurements shown in Fig. 4.16. The optimal air gap length function of this HFCT is obtained from these measurements and is as follows:

$$d_{\mathrm{air,opt}}(I_{1,50\mathrm{Hz}}) = \mathrm{e}^{\frac{I_{1,50\mathrm{Hz}}}{390}} - 1 \tag{4.14}$$

The validation plot of Fig. 4.12 compares the three optimal air gap length functions obtained from the measurements with those from the simulations using the developed split-core HFCT model.

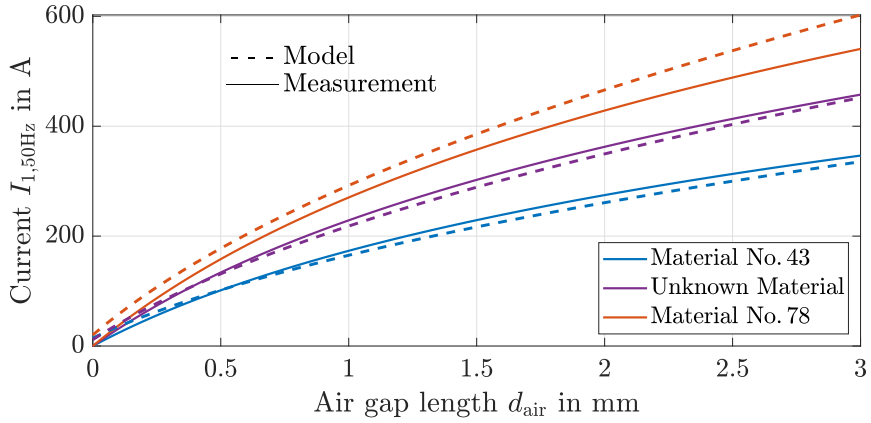

Figure 4.12: Validation of the split-core HFCT model using the optimal air gap length functions of three split-core HFCTs. The comparison of measurement and simulation shows only minor deviations, especially for the NiZn ferrites (Material No. 43 and unknown material).

Looking at the blue curve shows that the split-core model is good at predicting the optimal air gap length of the HFCT made of material No. 43. The deviation between measurement and simulation is minor. For the unknown material, the deviation between measurement and model is also negligible. The deviation is greater for the HFCT made

of material No. 78. Here, the saturation capability of the ferrite material is overestimated by the model by about 10 %, i. e., the simulated air gap length would be too short. An air gap that is too short is unacceptable.

Thus, it can be concluded that the split-core model works accurately for ferrites used in the HF range 3 − 30 MHz (mostly NiZn ferrites). If the recommended frequency range of the ferrite is lower than this (mostly MnZn ferrites), the model becomes less accurate and should not be used. However, since most HFCTs are built on NiZn ferrites to achieve measurement bandwidths in the HF range, the split-core model is a useful tool for computer-aided HFCT design.

It should be noted that the simulation result depends on the graphical construction of B_{Sat} and H_{Sat}. This step should therefore be carried out carefully.

In summary, this chapter has shown two ways to determine the optimal air gap length function of a split-core HFCT sensor, once experimentally and once simulatively. It has further been shown that effective online monitoring of power cables requires an HFCT with variable air gap length. In the next chapter, such an improved HFCT will be presented. When the split-core HFCT is operated at its optimal air gap length, the HFCT model of Subsection 3.3 provides a good approximation of its transfer function $\underline{Z}_{\mathrm{T}}(f)$.

Measurements of the second HFCT of the unknown ferrite material:

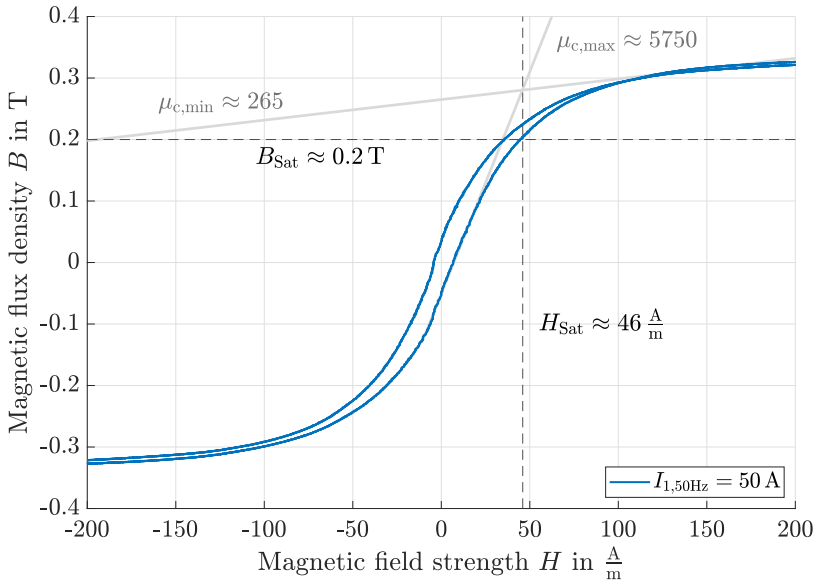

Figure 4.13: Magnetization curve of a split-core HFCT made of an unknown ferrite material suitable for the HF range, measured at 50 Hz.

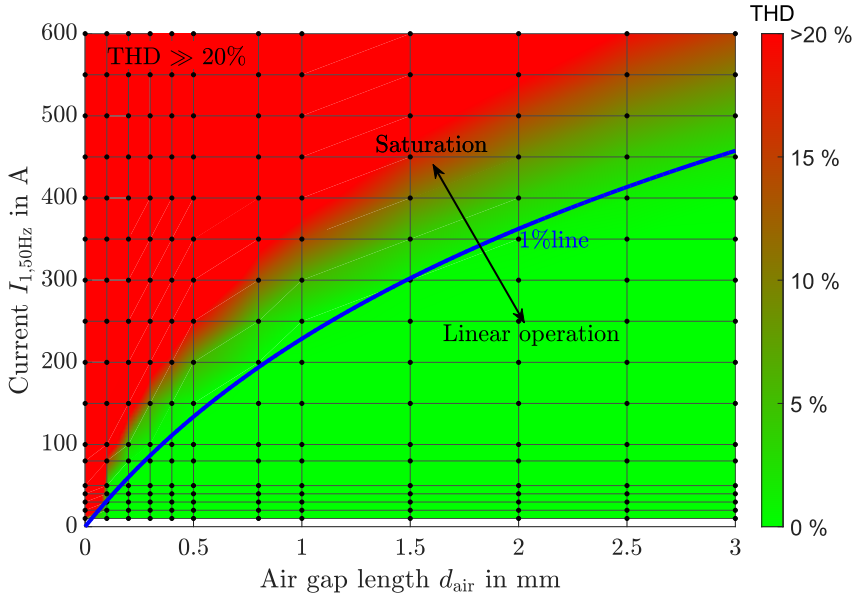

Figure 4.14: THD value of the output voltage of the HFCT with split-core of unknown material. Measurements at different air gaps and input currents. The 1 %-line marks the minimum air gap that ensures linear operation.

Measurements of the third HFCT of ferrite material No. 78:

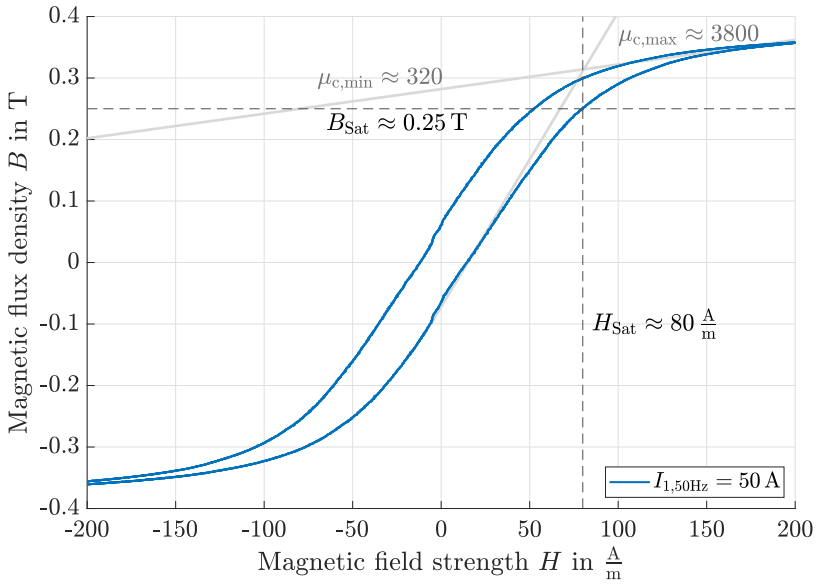

Figure 4.15: Magnetization curve of a split-core HFCT made of ferrite material No. 78 from the manufacturer Fair-Rite, measured at 50 Hz. The recommended frequency range for this material is < 1.5 MHz.

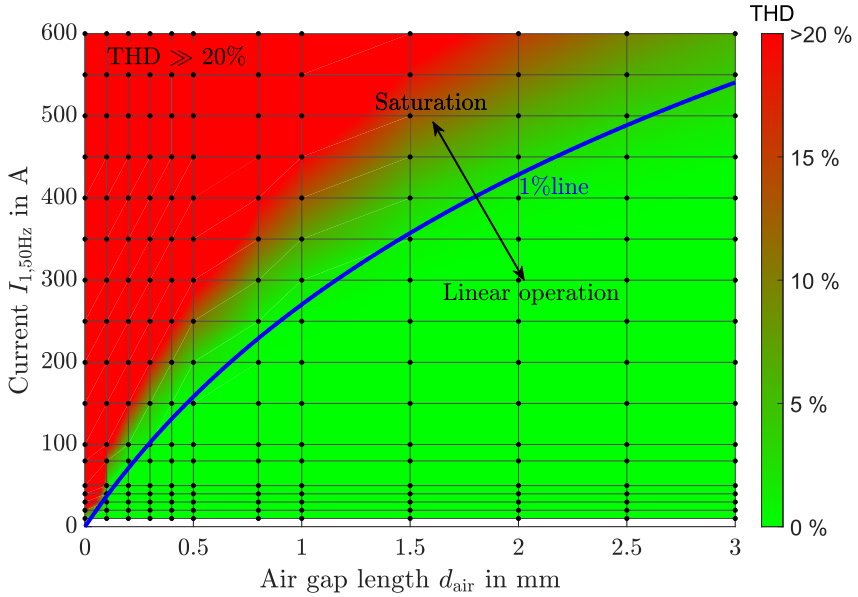

Figure 4.16: THD value of the output voltage of the HFCT with split-core of material No. 78. Measurements at different air gaps and input currents. The 1 %-line marks the minimum air gap that ensures linear operation.

5 Split-Core HFCT with Air Gap Control

The main cause of HFCT saturation in online PD monitoring of power cables is the operating current of these cables. To counteract saturation of the HFCT, a split-core with two air gaps is used. The length of the air gaps should be long enough to avoid saturation, but as short as possible to avoid loss of sensitivity. The optimal air gap length therefore depends on the saturation level of the HFCT and thus varies with the amplitude of the 50 Hz operating current of the power cable. Hence, to always achieve the maximum sensitivity, the HFCT should be able to automatically self-adjust the length of its air gaps to the saturation level. According to today's scientific literature, no such HFCT system exists to date.

Therefore, this chapter presents a concept for an improved split-core HFCT capable of self-adjusting its air gap length. The air gap length is controlled in real-time based on the saturation level of the HFCT core. For this purpose, a microcontroller is used to constantly monitor the HFCT for core saturation. In the event of saturation, the microcontroller controls a servomotor that varies the air gap length of the HFCT. At the same time, a second microcontroller monitors the HFCT output voltage for any PD pulse events.

This chapter is structured as follows. Section 5.1 shows a solution of how an HFCT with a moving split-core can be constructed. Section 5.2 then presents the air gap control strategy of the servomotor. Thereafter, Section 5.3 explains how the sensor performs the HF measurement and how the measured HF signal is subsequently evaluated using a PD detection algorithm.

5.1 Design of an HFCT with Air Gap Control

To change the air gap length of the HFCT during operation, a sensor design must be developed in which the two halves of the split-core are movable relative to each other. To increase the air gap, the core halves must be moved apart; to decrease it, they must be moved together again. For this task, it is sufficient if only one half of the core is movably mounted, while the position of the other half is fixed.

Fig. 5.1 shows a solution how to construct such a device. In this design, the left half of the core is movably mounted on a base plate and is driven by an electric servomotor. The left side of the figure shows the CAD design with the air gap fully closed, while the right side shows a photo of the manufactured prototype with the air gap open by a few mm.

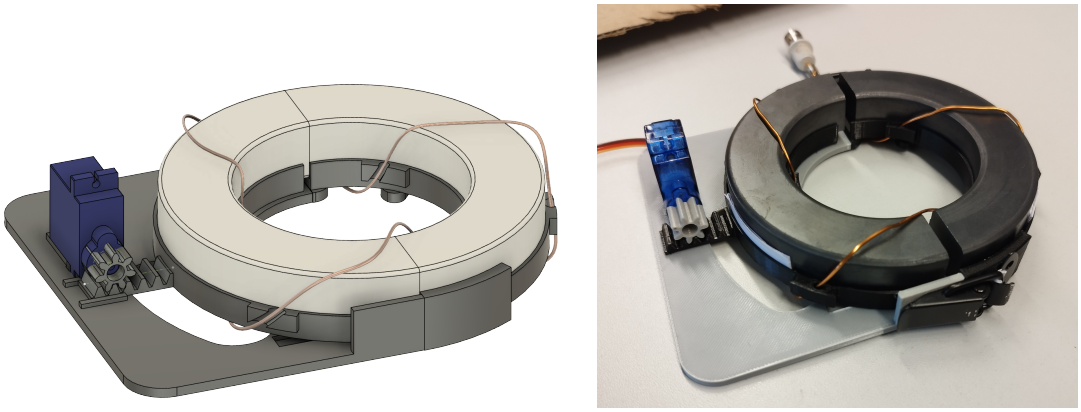

(a) CAD Design **(b)** Manufactured Prototype

Figure 5.1: Design of the HFCT with air gap control. The left half of the split-core can be moved via a servomotor. In this way, the length of the air gap d_{air} can be adjusted in small steps between 0 and 12.4 mm. The motor is controlled by an Arduino microcontroller.

The servomotor used is an MG90S type motor. This type of servo is inexpensive and lightweight, but has a torque of about 1.8 kg/cm at an operating voltage of 5 V, which is sufficient to move one half of the ferrite core (weight of about 175 g). The rotation angle of the servomotor φ can be adjusted between 0 and 180° with a resolution of 1°. An integrated position control loop guarantees high precision. The angle setpoint is specified by a microcontroller, which controls the air gap length in this way. Fig. 5.1 shows how a rotation of the servomotor is converted into a translational movement of the left half of the core. The position of the right half of the core does not change. With this design it is possible to vary the air gap length between 0 and approximately 12.4 mm, which corresponds to changing the rotor angle from 180 to 0°.

The relationship between the air gap length d_{air} of the HFCT and the rotation angle φ of the servomotor is a linear function:

$$d_{\text{air}}(\varphi) \approx -0.0687 \frac{\text{mm}}{1^\circ} \cdot \varphi + 12.366\,\text{mm} \tag{5.1}$$

Thus, the smallest possible step width of ±1° corresponds to a minimum length change of ±0.0687 mm.

All parts of the prototype in Fig. 5.1 are designed using CAD software and then printed using an FDM 3D printer (except for the ferrite core and winding). The construction consists of three individual elements, which can be better seen in Fig. 5.2 on the left. There are two brackets printed from black filament, on which the two halves of the core are mounted. The third element is a base plate printed from gray filament to which one

of the brackets, and thus one half of the core, is attached via a sliding rail system. The rails have the shape of a trapezoid (dovetail). The servomotor is equipped with a printed gear wheel and is mounted on the base plate with a strong super glue. The gear wheel drives a gear rack that moves the bracket along the sliding rails. The two halves of the construction are connected by snap locks so that they can be easily separated at any time for installation. The snap locks are also glued to the printed parts with super glue. During manufacture, all parts are assembled first and the copper winding is attached last. The winding is fed through holes in the printed parts at various points to guide it and hold it in position. Both ends of the winding are connected to a BNC connector where the HFCT output voltage u_{L} can be measured.

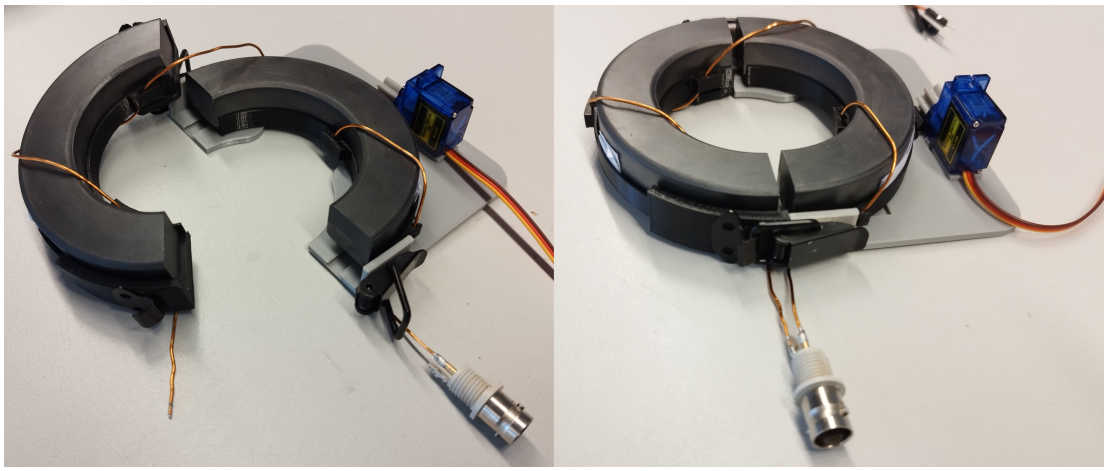

Figure 5.2: The manufactured prototype in open and closed state. The two halves of the sensor are connected by snap locks and can be easily separated. In the photos, the BNC connector is soldered to the winding – a pluggable BNC connector would be better to further facilitate the installation of the sensor around a power cable.

5.2 Servomotor Control

The output voltage of the HFCT winding is connected to two microcontrollers. One measures the 50 Hz component of its output voltage and takes over the control of the servomotor for optimal adjustment of the air gap length. The other measures the HF component of the HFCT output voltage and is responsible for PD detection. In this section, the servomotor control is discussed first.

The optimal air gap length of the developed HFCT $d_{\mathrm{air,opt}}$ depends on the 50 Hz operating current of the monitored power cable $I_{1,50\mathrm{Hz}}$. If the operating current strength were known, the optimal air gap length could be set according to (4.2). Unfortunately, it is not possible to measure $I_{1,50\mathrm{Hz}}$ or calculate it from the HFCT output voltage u_{L} because

the transfer function of an HFCT with air gap control is nonlinear. Any change in air gap length results in a change of the HFCT transfer function, so there is no simple relationship between u_L and $I_{1,50\mathrm{Hz}}$. Instead, the THD value of the 50 Hz component of u_L can be calculated to determine the saturation level of the HFCT core. Then, the air gap length can be controlled to minimize THD and thus saturation. For this task, the 50 Hz component of the HFCT output voltage u_L must be measured continuously.

Since the HFCT is optimized for measuring signals in the HF range, its sensitivity at 50 Hz is very low (cf. Fig. 3.17 on page 58). Accordingly, the amplitude of the 50 Hz component of the measured HFCT output voltage is low and only in the mV range, as shown in Fig. 5.3 on the top. For this figure, the 50 Hz operating current of the power cable $I_{1,50\mathrm{Hz}}$ is increased from 20 to 300 A, while the air gap length of the HFCT is set to its optimum according to (4.2).

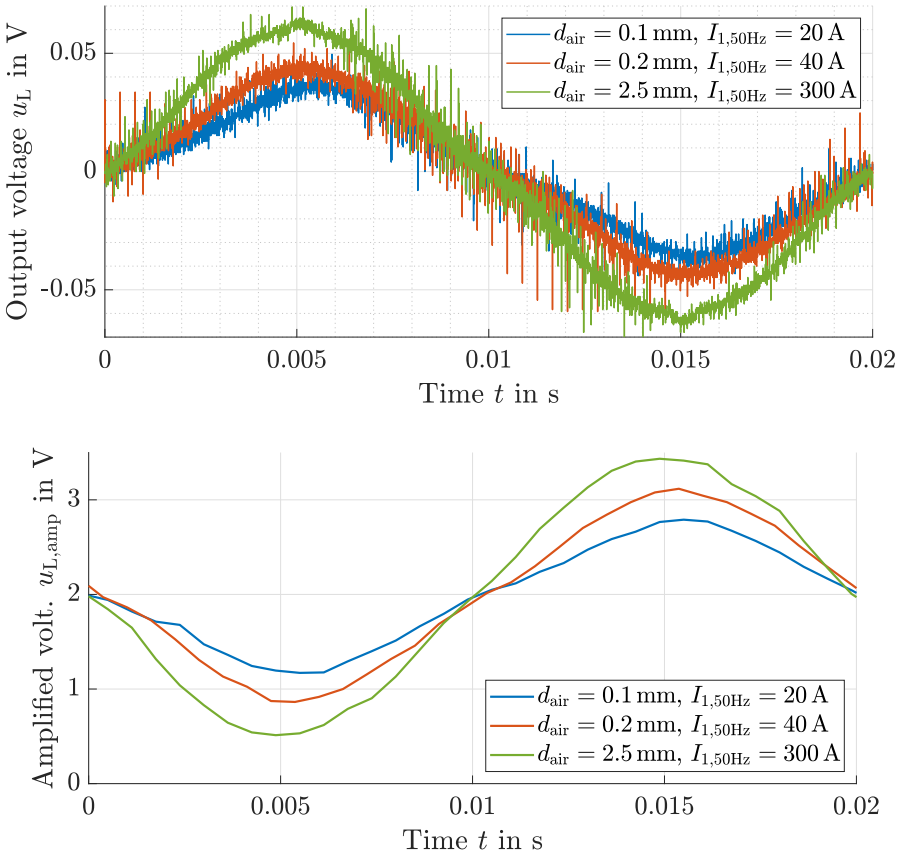

Figure 5.3: Top: 50 Hz component of the HFCT output voltage measured at three optimal operating points. The amplitudes of the measured sines $\hat{u}_\mathrm{L}$ are in a range of about 35 – 60 mV.
Bottom: Amplified HFCT output voltage measured at the same operating points.

With optimal air gap length and thus unsaturated HFCT core, the measured HFCT output voltage is sinusoidal for all operating currents. Although $I_{1,50\mathrm{Hz}}$ is varied over a wide range, the measured voltages look quite similar. Their amplitudes $\hat{u}_\mathrm{L}$ range from about 35 – 60 mV. Thus, at optimal air gap length, the amplitude of the 50 Hz component of the HFCT output voltage is always $\hat{u}_\mathrm{L} < 60\,\mathrm{mV}$ (tested for all operating currents up to $I_{1,50\mathrm{Hz}} < 350\,\mathrm{A}$). Amplitudes larger than $\hat{u}_\mathrm{L} > 60\,\mathrm{mV}$ only occur when the air gap is too short and core saturation occurs.

To measure the 50 Hz component of u_L an Arduino Nano microcontroller is used. This model is very inexpensive due to its widespread use. The Arduino's analog-to-digital converter (ADC) has a default sampling frequency of about $f_\mathrm{s} = 9600\,\mathrm{Hz}$, which is sufficient for accurate measurement of the 50 Hz voltage component. For air gap control, the Arduino must first digitize the HFCT output voltage, then perform a Fourier transform of the measurement, and then calculate its THD. For digitization, the Arduino's ADC maps input voltages between 0 and 5 V into integer values between 0 and 1023.

So, the 50 Hz component of the HFCT output voltage is a sine of about ±60 mV, while the input range of the Arduino's ADC allows for 0 – 5 V. Because of the different voltage levels, the HFCT output voltage u_L is not directly connected to the Arduino, but amplified before. For this task, a low-cost and widely used operational amplifier of type LM324N is used. The amplifier circuit is shown in Fig. 5.4.

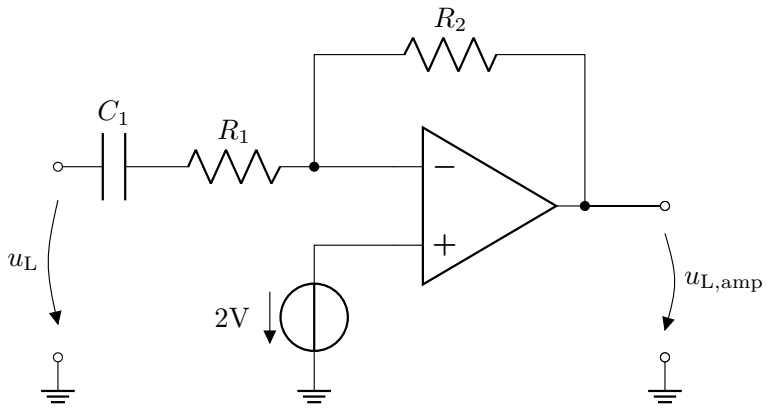

Figure 5.4: Inverting amplifier to amplify the HFCT output voltage u_L before it is digitized by the Arduino microcontroller. For a gain of about 25, the resistors are set to $R_1 = 2.2\,\mathrm{k\Omega}$ and $R_2 = 56\,\mathrm{k\Omega}$. The coupling capacitor has a capacitance of $C_1 = 50\,\mu\mathrm{F}$. The equivalent circuit diagram does not show the power supply connections of the operational amplifier.

The circuit works as an inverting amplifier and provides an additional offset voltage of 2 V. To set the offset, a voltage source is connected to the positive input of the operational

amplifier. The amplified voltage at the output of the operational amplifier circuit can be calculated as follows [64]:

$$u_{\mathrm{L,amp}}(t) \approx -u_{\mathrm{L}}(t) \cdot \frac{R_2}{R_1} + 2\,\mathrm{V} = -u_{\mathrm{L}}(t) \cdot G + 2\,\mathrm{V} \tag{5.2}$$

The gain is set to $G \approx 25$ so that the amplified voltage $u_{\mathrm{L,amp}}$ gives a sine wave oscillating in the range of about 2 V ± 1.5 V (at optimal air gap length). A higher gain factor is not possible, because the operational amplifier is operated from a single supply voltage of 5 V, which is supplied by the Arduino. With this supply voltage, the output voltage of the LM324N operational amplifier is limited to about 0.3 – 3.8 V (it is not a rail-to-rail amplifier). The input signal u_{L} is connected to the operational amplifier via a coupling capacitor C_1.

After amplification, the voltage $u_{\mathrm{L,amp}}$ is connected to an analog input pin of the Arduino Nano and thus to a channel of its ADC. The signal measured by the Arduino is shown in Fig. 5.3 on the bottom. The amplified signal levels now fit well with the input specifications of the Arduino's ADC of 0 – 5 V. The figure also shows that the Arduino measurement is almost free of HF noise due to the low sampling frequency (only the 50 Hz component is measured).

After digitizing and measuring the amplified signal, the Arduino performs a fast Fourier transform (FFT) with the measured data. The spacing between two frequencies of the Fourier transform (frequency resolution) depends on the sampling frequency f_{s} of the ADC and the number of samples N measured (block length):

$$f_{\mathrm{step,FFT}} = \frac{f_{\mathrm{s}}}{N} \tag{5.3}$$

Due to the limited memory of the Arduino, the number of samples of one measurement is limited to $N = 128$ when using FFT commands. Therefore, the default resolution in the frequency domain would be $f_{\mathrm{step,FFT}} = \frac{9600\,\mathrm{Hz}}{128} = 75\,\mathrm{Hz}$. These frequency steps are inadequate because the harmonics of the Fourier transform of a 50 Hz sinusoidal signal are 150 Hz, 250 Hz, and so on. For better resolution in the frequency domain, the sampling frequency is lowered to $f_{\mathrm{s}} = 1600\,\mathrm{Hz}$. The frequency resolution of the Fourier transform is then $f_{\mathrm{step,FFT}} = \frac{1600\,\mathrm{Hz}}{128} = 12.5\,\mathrm{Hz}$. This is a good trade-off to avoid information loss during digitization: 1600 Hz is a sufficient resolution in the time domain and 12.5 Hz is at the same time a suitable step size in the frequency domain.

After the Fourier transform of $u_{\mathrm{L,amp}}$, the THD value of the measurement is calculated according to (4.1). The THD calculation is performed based on the first seven harmonics (150, 250, . . . , 750 Hz). The Fourier transform now contains a DC component which is due to the DC offset of the operational amplifier. This DC component is simply ignored

in all calculations. A pure sine signal would result in a THD factor of 0. Because of the omnipresent measurement noise, the calculated THD value is always somewhat higher than in theory. Earlier in this work, a THD threshold of 1 % was defined to distinguish between saturated and unsaturated HFCT core. This 1 % criterion also holds to measurements recorded with the Arduino, as can be seen in Fig. 5.5. The area without core saturation, below the blue line, is characterized by THD values less than 1 %. Therefore, as soon as a THD value greater than 1 % is calculated, the air gap length must be increased.

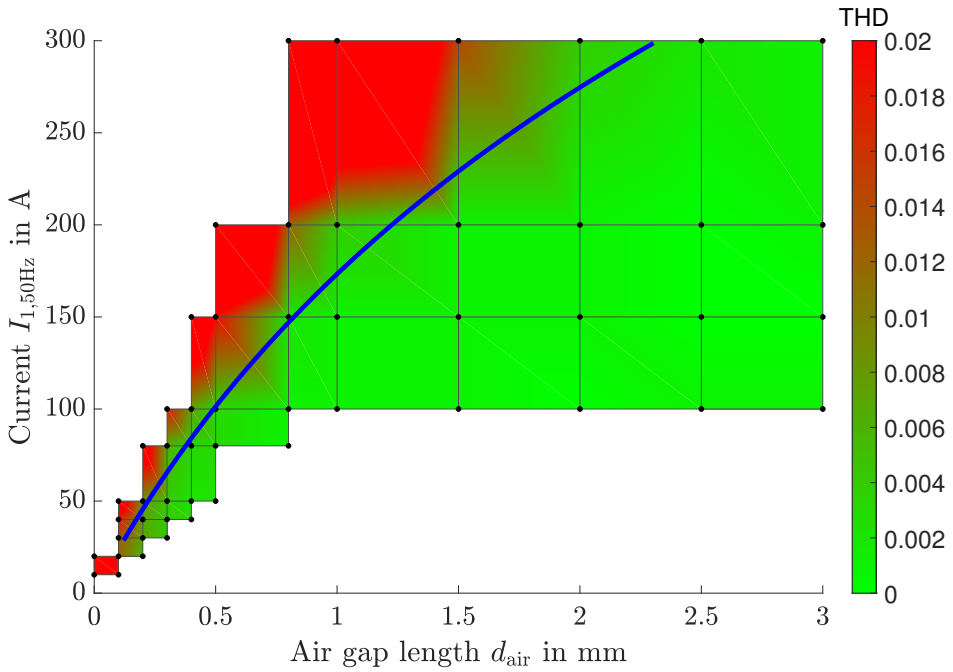

Figure 5.5: Measurements of the amplified HFCT output voltage $u_{\text{L,amp}}$ with the Arduino at different input currents $I_{1,50\text{Hz}}$ and air gap lengths d_{air}. The calculated THD value of the measured signals is shown. The blue line indicates the optimal air gap length according to (4.2).

To better understand the sequence of the Arduino program, see the flowchart in Fig. 5.6. After starting, the ADC of the Arduino is initialized first and its sampling frequency is set to $f_s = 1600\,\text{Hz}$. Then, a measurement of the initial angle φ_0 of the servomotor is performed. The servo has a built-in potentiometer that provides a voltage signal U_{pot} proportional to the current angle of rotation. To measure this voltage, the middle pin of the potentiometer is connected to an analog input pin of the Arduino. By knowing the voltages at the two limits 0 and 180 degrees, U_{pot} can be mapped linearly to the rotation angle φ of the servomotor. At the end of the setup phase, a timer t is initialized and started before the program enters the main loop.

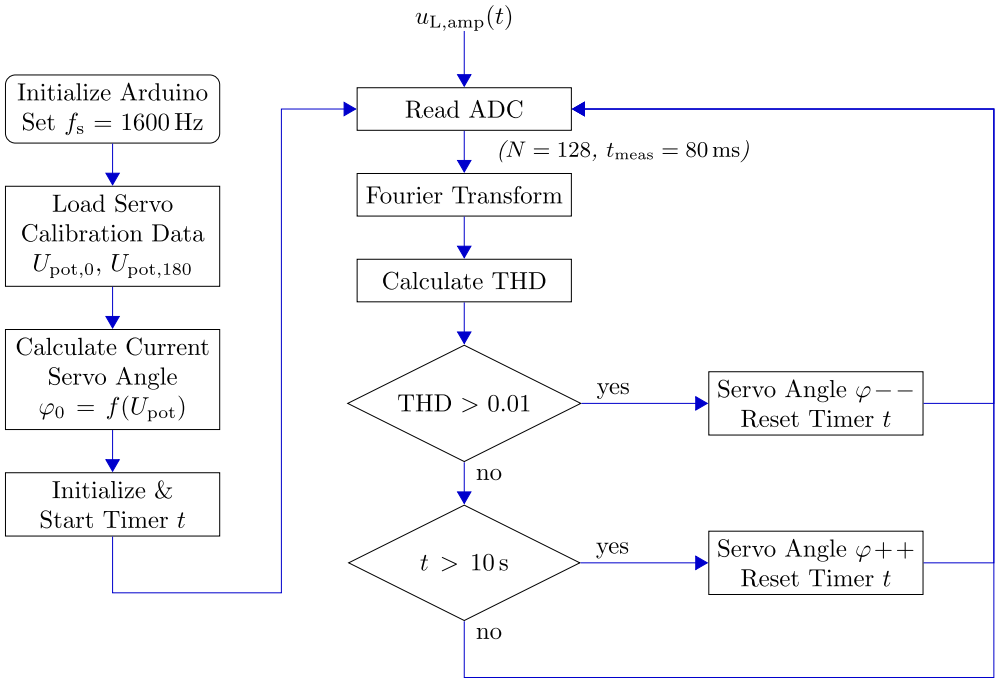

Figure 5.6: Flowchart of the Arduino program (air gap control algorithm).

In the main loop, the Arduino continuously measures the amplified HFCT signal $u_{\mathrm{L,amp}}(t)$ and monitors its THD value. If the THD value is greater than 1 percent, the rotation angle φ of the servomotor is reduced by one degree to open the air gap. If the air gap is large enough, saturation does not occur and the THD value is less than 1 percent. In this case, the rotation angle φ of the servomotor is increased by one degree every 10 seconds to keep the air gap as short as possible, i. e., close to its optimum. Increasing the air gap length has priority over decreasing it, since the air gap should rather be too large than too short. The value of 10 seconds was chosen arbitrarily for the initial testing of the prototype. In a realistic environment, this time value depends on the rate of change of the amplitude of the power cable's operating current. This needs to be further investigated in the future.

Fig. 5.7 shows a schematic representation of all the parts connected to the Arduino microcontroller. So, this schematic shows all the hardware required for air gap control of the split-core HFCT. It is important to use a separate voltage source to supply the servomotor. Powering servos from the 5 V pin of the Arduino is not recommended because the pin cannot supply enough current to the servo, especially under load. In addition, the PWM signal controlling the servomotor distorts the 50 Hz measurement and thus the THD calculation. Thus, for the following measurements, Arduino and servomotor of the prototype are supplied with power by two separate DC voltage sources, both with a supply voltage of 5 V.

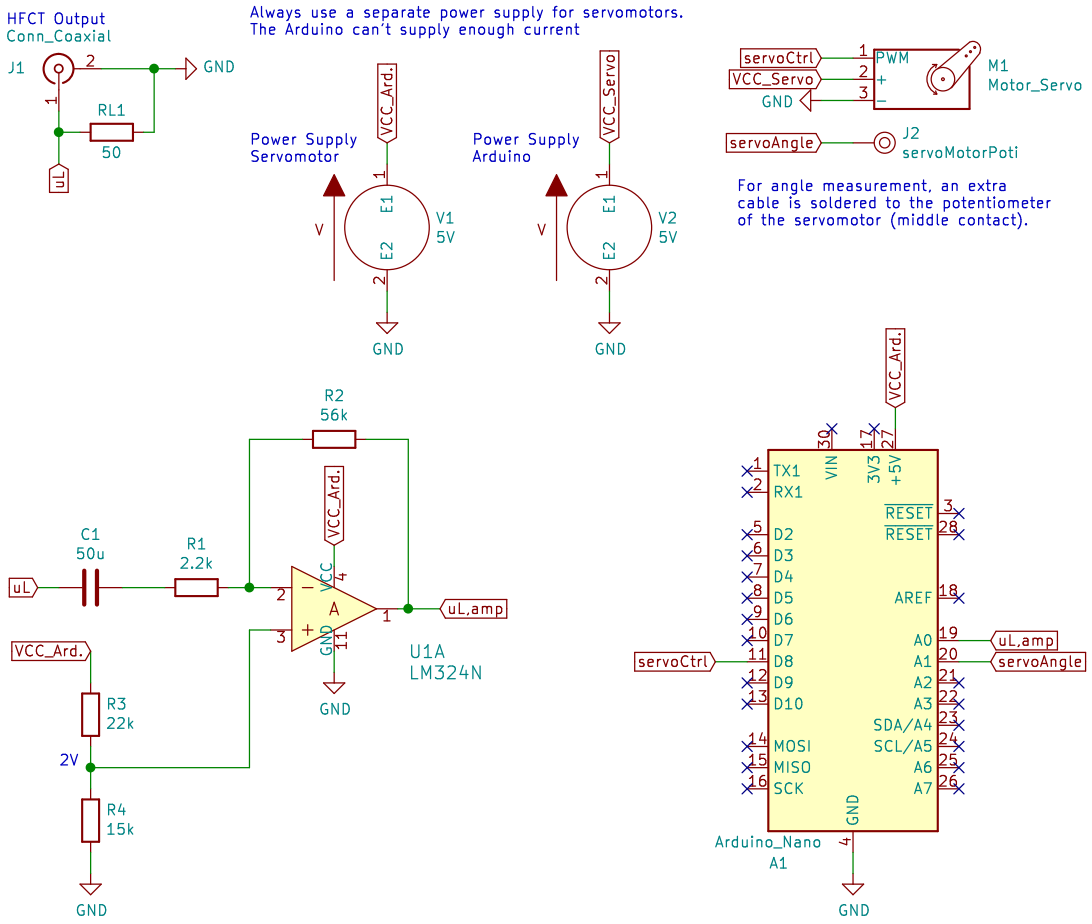

Figure 5.7: Schematic of the control circuit for adjusting the air gap length of the split-core HFCT prototype.

To keep the torque of the servomotor and thus the required current low, all moving parts of the prototype should be well lubricated. However, currents > 100 mA may occur for short times (the stall current of the MG90S servo at 5 V operating voltage is about 500 mA) [65]. Care should therefore be taken to ensure that all connections and cables supplying the servomotor have a sufficient cross-section.

To check whether the servomotor control and thus the developed HFCT prototype works as planned, various measurements have been performed. Fig. 5.8 shows the results of an exemplary test run of about 13 minutes duration. During the test run, the HFCT is subject to an increasing 50 Hz input current $I_{1,50\text{Hz}}$, as shown by the blue line. The dashed red line shows the optimal air gap length $d_{\text{air,opt}}$ of the HFCT according to (4.2). The solid red line shows the actual air gap length set by the servomotor. The test run stops at a current of 180 A, because the current source is then overloaded, so that higher currents cannot be tested with the equipment used (Omicron CMC-256-6).

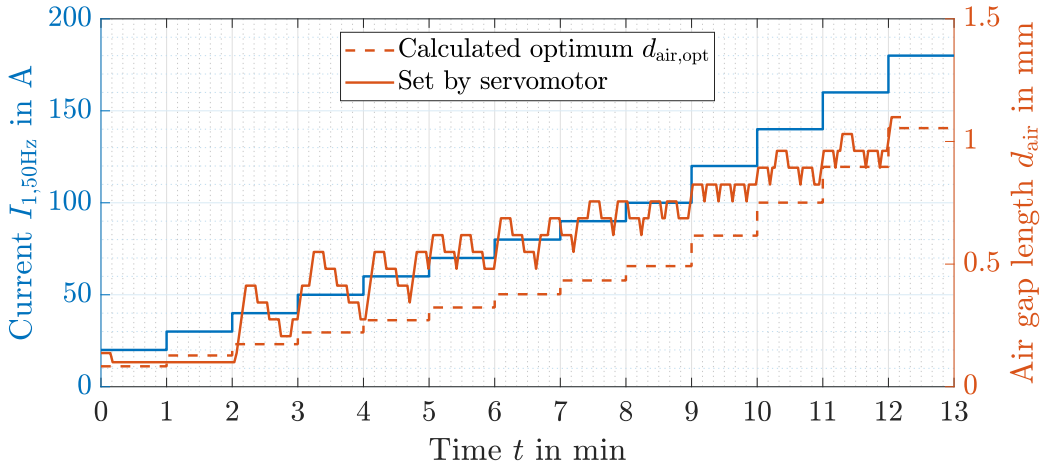

Figure 5.8: Testing the HFCT prototype with increasing 50 Hz input current. The air gap length set by the algorithm is shown in comparison to its optimum.

It can be seen that the set air gap length is often a bit too long compared to the optimum and how the algorithm constantly tries to shorten the air gap every 10 seconds.

Fig. 5.9 shows the results of another similar test run with a much longer duration of about 47 minutes. For this exemplary long-term test, it is useful to include the moving average of the set air gap length in the figure.

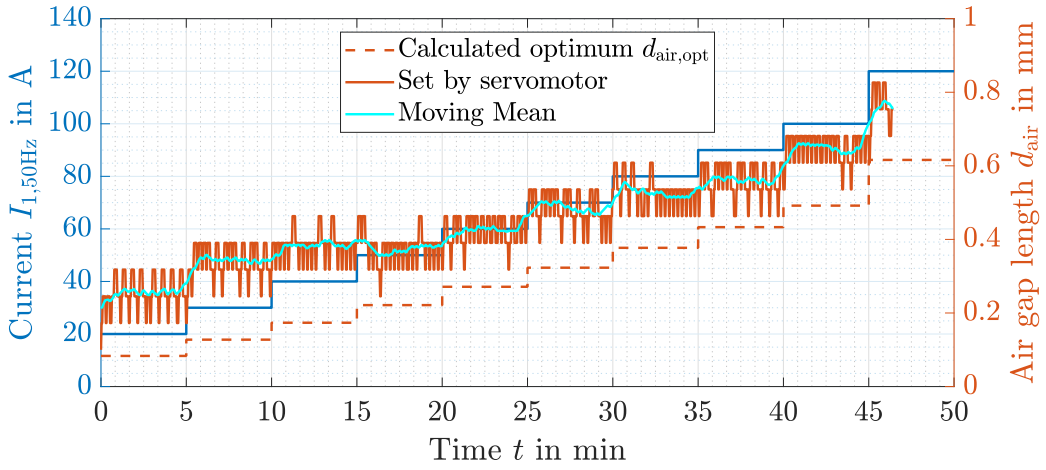

Figure 5.9: This test is similar to the one in Fig. 5.8, but over a much longer duration. The cyan curve shows the moving average of the set air gap length.

It can be seen that the shape of the moving average is similar to the calculated optimum plus an additional offset of about 0.2 mm at all times. So the air gap control works as intended, but the experiments show a constant deviation.

This systematic deviation can be observed in all test runs performed. To better quantify the deviation, the data of all the test runs performed are averaged with respect to the air gap length set by the servo motor. The result is shown in Fig. 5.10 together with the optimal air gap length function of the HFCT according to (4.2).

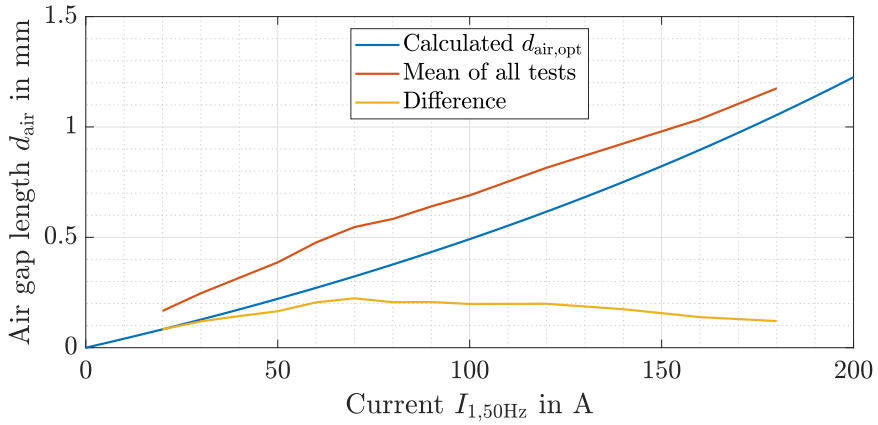

Figure 5.10: The air gap length set by the algorithm is close to the calculated optimum. The yellow curve shows the mean deviation between the air gap control algorithm and the optimal value.

It can be clearly seen that the actual air gap is always slightly longer than the optimum, to be precise 0.1 – 0.2 mm longer. This systematic deviation is mainly due to noise in the measured $u_{\mathrm{L,amp}}$ signal, which affects the calculated THD level. A higher THD level results in a longer air gap than necessary. Two main sources of noise can be identified. First, general noise in the voltage signal and due to the measurement process. The level of this noise should be almost the same for all air gaps and is compensated by the 1 % THD threshold value. Second, it was observed that the moving part of the prototype tends to vibrate with short air gaps $d_{\mathrm{air}} < 1$ mm due to magnetic forces. This vibration introduces additional noise into the voltage measurement. As d_{air} increases, the vibrations decrease and the signal-to-noise ratio of $u_{\mathrm{L,amp}}$ improves. Thus, for higher currents $I_{1,50\mathrm{Hz}}$, the deviation between the set and optimal air gap length becomes smaller. The impact of the vibrations is strongest between about 50 – 100 A. To better avoid the vibrations and thus reduce the systematic deviation, the sensor design should be further improved in the future (mechanical redesign). Overall, however, both curves are close to each other, proving that the algorithm is working correctly. The developed HFCT design and the servomotor control thus work as intended.

With the help of the developed control strategy, the air gap length of the HFCT prototype is set close to optimal at all times and the sensor can be used for online monitoring of power cables. Since no magnetic saturation occurs, the HFCT sensor always operates close to its highest possible sensitivity.

5.3 HF Measurement and PD Detection

To turn the HFCT into a PD sensor for online monitoring, the HF component of the HFCT output voltage must be continuously measured and monitored for PD signals. For this task, the HFCT output u_L is connected to a second microcontroller running a PD detection algorithm. For a better overview of the overall sensor system, see Fig. 5.11. The Arduino handles all tasks related to the automatic air gap control of the split-core HFCT, while the other microcontroller continuously monitors u_L for PDs. This section discusses all blocks related to PD measurement.

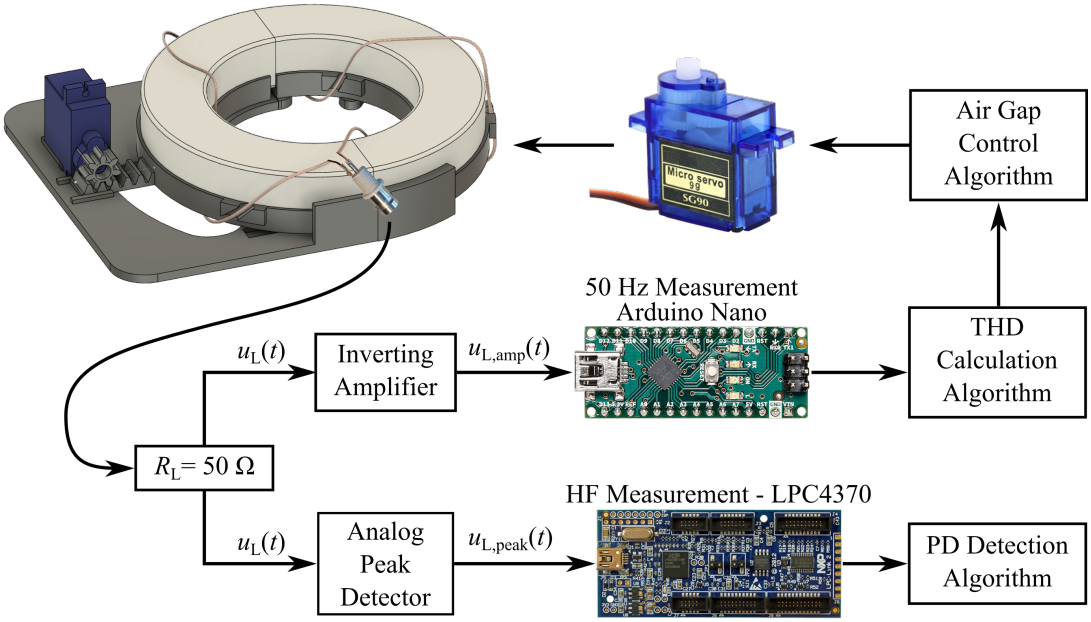

Figure 5.11: Overview of the complete PD sensor system based on a split-core HFCT with air gap control. The air gap length of the HFCT is controlled by the Arduino, while the LPC4370 microcontroller monitors the power cable for PDs.

Before the analog output signal of the HFCT u_L can be processed by a PD detection algorithm, it must first be digitized. The ADC of a microcontroller is to be used for this task. The sampling frequency of the ADC must be high enough to avoid information loss. Since the spectrum of PD pulses contains signal components up to the HF range, the ADC used must be very fast. It has been shown that successful online monitoring of power cables requires at least an HFCT bandwidth of 10 MHz to detect the majority of PDs. Therefore, the sampling frequency of the ADC must be at least greater than $f_s > 20\,\text{MHz}$ (for accurate peak detection it should be much higher). This task cannot be handled by most microcontrollers because their ADCs are much too slow. Of the low-cost microcontrollers, only the LPC4370 from the manufacturer NXP is capable

of measuring HF signals. The LPC4370 is equipped with a high-speed ADC with a maximum sampling frequency of f_s = 80 MHz and sampling resolution of 12-bit (bit depth) [66]. The controller is available as a development board called LPC-Link 2, which is used in the prototype for HF measurement and PD detection.

Measuring u_L at a sampling frequency of 80 MHz is possible with the LPC4370 microcontroller, but the amount of data recorded is very large. The measured data stream would generate about 120 Megabytes of data every second. Although the LPC4370 is equipped with a 204 MHz fast dual-core processor, it cannot process this large amount of data in real-time. Therefore, to achieve continuous online PD monitoring, the sampling frequency must be significantly reduced without losing information. For this purpose, the analog signal u_L is preprocessed using an analog peak detector circuit, which can be seen in Fig. 5.12.

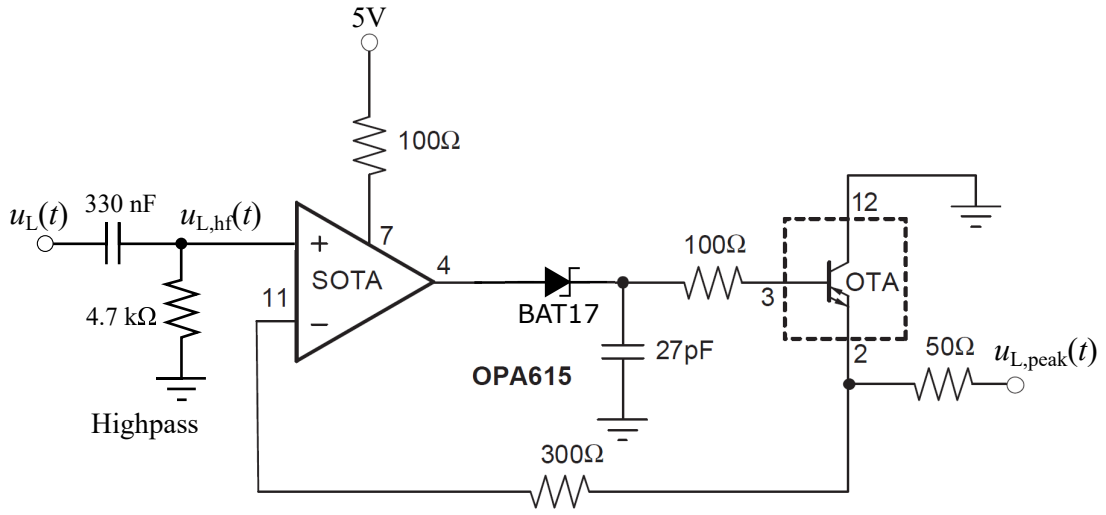

Figure 5.12: Analog peak detector circuit based on the OPA615 IC from Texas Instruments. This circuit diagram is based on the manufacturer's data sheet of the IC, but optimized for PD measurements [67]. A high-pass filter is connected in front of the peak detector to suppress the 50 Hz component of u_L.

This circuit is based on an OPA615 IC from Texas Instruments, which can be used as peak detector for nanosecond pulses. Peak detection is performed by charging a capacitor via a diode. Because of the diode, only positive peak values can be measured with the circuit shown. The same circuit with reversed diodes can be used to measure negative pulses. To improve the response time of the circuit, Schottky diodes should be used as they react much faster than conventional diodes. Furthermore, it is important to set the hold Control Pin 7 of the circuit to 5 V (high) to enable continuous monitoring. More information on this topic can be found in [68]–[70].

A high-pass filter is connected in front of the OPA615 IC to filter out any 50 Hz component from the HF measurement. The high-pass consits of a capacitor $C = 330\,\text{nF}$ and a resistor $R = 4.7\,\text{k}\Omega$, resulting in a cut-off frequency of $f_{-3\,\text{dB}} \approx 100\,\text{Hz}$.

Fig. 5.13 shows the operation of the peak detection circuit using an exemplary input signal $u_\text{L}(t)$. The figure is based on simulations with LTSpice. The input signal contains various PD like impulses.

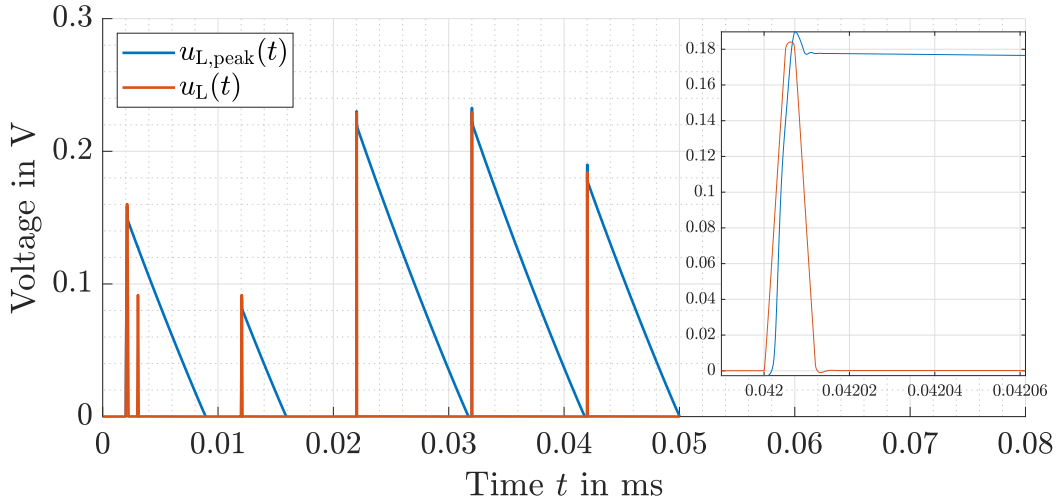

Figure 5.13: Input and output voltage of the peak detection circuit. It can be seen how the peak value of the input signal is stored by the capacitor for a certain time. The storage effect can be better seen in the zoom on the right side. The storage time is limited by the self-discharge rate of the capacitor.

It can be seen that the output signal $u_{\text{L,peak}}(t)$ follows the highest value of the input voltage by charging the capacitor. In this way, the capacitor stores the pulse amplitude information of the input signal. This can be clearly seen in the zoomed view on the right side of the figure. Over time, the capacitor discharges again and is ready to capture the next pulse. The choice of capacitor is a compromise between a small capacitance that can quickly follow the input signal and a larger capacitance that stores the information longer but responds more slowly. A capacitance of 27 pF is well suited for measuring nanosecond pulses. From the simulations, the self-discharge rate of the capacitor is about 23 $\frac{\text{V}}{\text{ms}}$ or 23 000 $\frac{\text{V}}{\text{s}}$.

The output signal $u_{\text{L,peak}}(t)$ is now much easier to digitize, since the signal bandwidth has been significantly reduced compared to $u_\text{L}(t)$. The ADC sampling frequency f_s can thus be greatly reduced without losing much amplitude and time information of the PD pulses. Only the information about the exact pulse shape is lost during signal preprocessing, but this is not a problem for pulse detection.

For further demonstration, Fig. 5.14 shows the analog signal $u_{\mathrm{L,peak}}(t)$ out of Fig. 5.13 and the same signal sampled at two different frequencies, 4 MHz and 2 MHz.

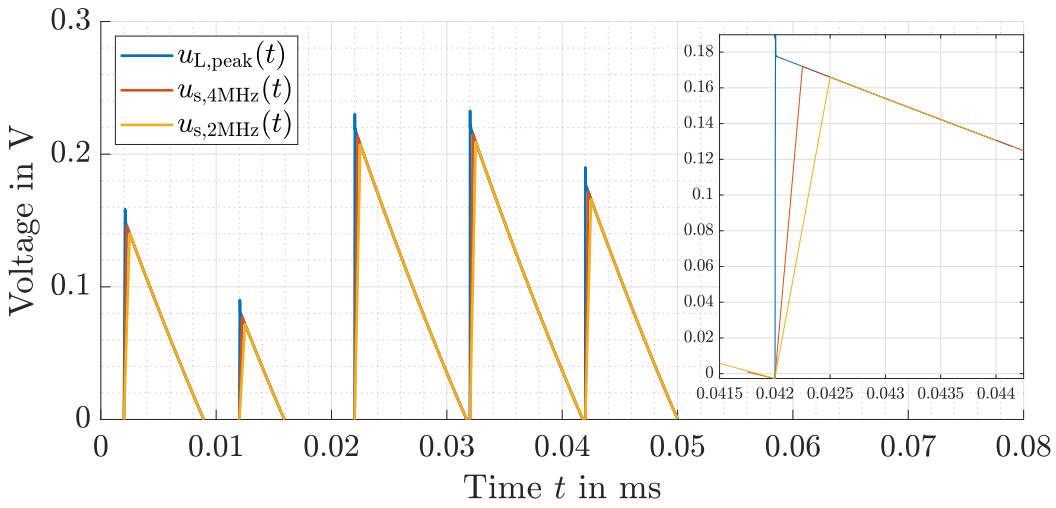

Figure 5.14: The blue line shows the output voltage of the peak detection circuit. This voltage is digitized by an ADC. For the red line the ADC sampling frequency is set to 4 MHz and for the yellow line to 2 MHz. Both sampling speeds are sufficient to digitize the signal with good quality. Only the amplitude is a bit reduced.

It can be seen that both sampling frequencies are sufficient to digitize $u_{\mathrm{L,peak}}(t)$ with good quality. Only the captured amplitudes are slightly lower than those of the original signal, which can be seen better in the zoom on the right side. Sampling $u_{\mathrm{L,peak}}$ with a frequency of $f_{\mathrm{s}} = 2\,\mathrm{MHz}$ results in a maximum amplitude error of about 11 mV. Compared to 80 MHz, the sampling frequency can be reduced by a factor of 40, freeing up large processor resources that can be used for further signal evaluation instead. At $f_{\mathrm{s}} = 4\,\mathrm{MHz}$ the maximum amplitude error is in the range of 5 mV and the sampling frequency is still a factor of 20 lower than without preprocessing.

Another benefit of reducing the sampling frequency is that the amount of recorded data decreases. With $f_{\mathrm{s}} = 2\,\mathrm{MHz}$ the data stream is reduced to about 3 Megabytes every second compared to the initial 120 Megabytes per second. The PD detection algorithm thus has to process a lot less data and will be more efficient.

Accordingly, the output voltage of the analog peak detector circuit $u_{\mathrm{L,peak}}(t)$ is connected directly to an ADC input channel of the LPC4370 board. The sampling frequency is set to $f_{\mathrm{s}} = 2\,\mathrm{MHz}$. The digitized signal is then processed in real-time by the LPC4370 processor using a PD detection algorithm.

The algorithm is based on [71] and can be described with the following pseudocode.

```
# U(t) is the measured vector sampled by the ADC
# Settings
lag = 16;           # window length for moving mean and std. calculations
threshold = 3.5;    # peak when data point is 3.5 std. away from the mean value
influence = 0.01;   # peak data has very little influence on mean/std. calc.

# Initialize variables
out = 0;                              # initialize output signal
avgCalc = mean(U(1),...,U(lag));    # initial moving mean value
stdCalc = std(U(1),...,U(lag));     # initial moving standard deviation value

# Main loop
for i=lag+1,...,t do
  if absolute(U(i) - avgCalc) > threshold*stdCalc then
    out = 1;                                          # peak detected
    U(i) = influence*U(i) + (1-influence)*U(i-1);   # reduce influence of peak
                                                      # on next mean/std. calc.
  else
    out = 0;                                          # no peak detected
  end
  avgCalc = mean(U(i-lag+1),...,U(i));      # calculate moving average value
  stdCalc = std(U(i-lag+1),...,U(i));     # calculate moving std. value
end
```

The algorithm is based on the statistical parameters mean and standard deviation. The moving average and the moving standard deviation of the ADC data stream are calculated based on the last 16 measured values. The window length for these calculations can be adjusted with the *lag* setting. Each time the ADC provides a new reading, the main loop of the algorithm is executed once. At the beginning of the loop, it is checked whether the new data point is more than 3.5 standard deviations away from the moving average value. If yes, the output signal *out* is set to 1. The sensitivity of the algorithm can be adjusted with the *threshold* setting. To make the algorithm more robust, the peak values should have only a small influence on the calculation of mean and standard deviation. Thus, when a peak is detected, the value of the corresponding data point is artificially reduced based on the *influence* setting.

The algorithm has been tested with some example data created with LTSpice, see Fig. 5.15. The input data is similar to the pulse sequence shown in Fig. 5.13, but is additionally overlaid with noise. The signal-to-noise ratio is about 10. The absolute noise level is between 20 and 40 mV, which is a typical noise level for online PD measurements according to [72]. It can be seen that the algorithm detects all peaks of the input signal, i. e., all PD occurrences. The initial *delay*, *threshold*, and *influence* settings used for this test are determined by trial and error method. To improve algorithm performance, they should be statistically optimized in the future.

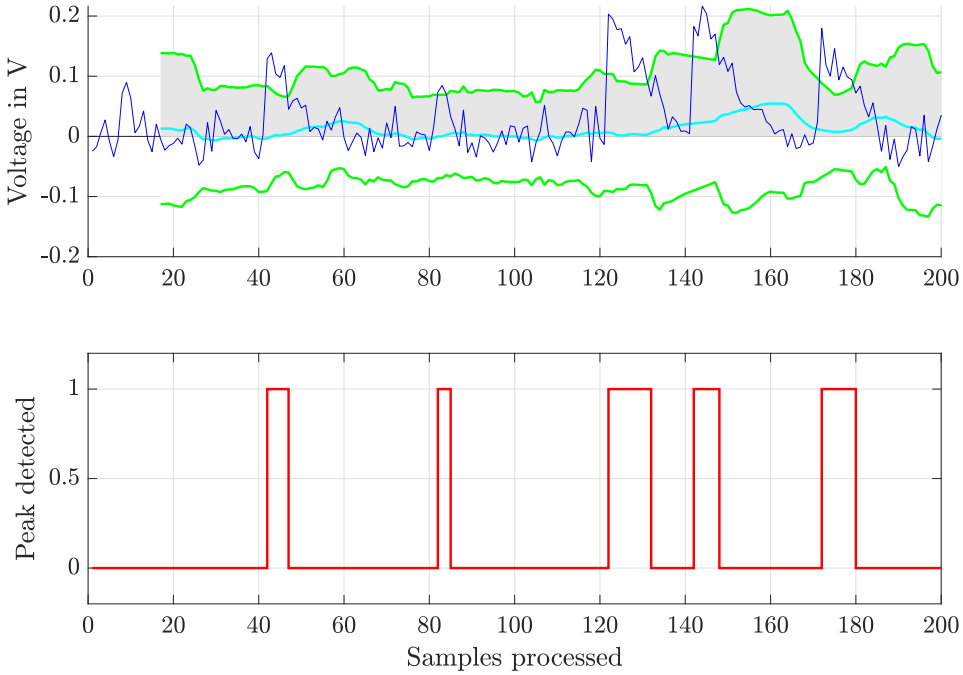

Figure 5.15: Simulative test of the PD detection algorithm. The upper plot shows the noisy input voltage (dark blue). Also shown are the moving average (cyan) and moving standard deviation (green) of the algorithm. The lower plot shows the output of the algorithm that indicates where PDs are detected.

In summary, this chapter has shown a concept how to improve HFCT technology for online PD monitoring of power cables. The developed prototype solves the saturation problem in a simple but efficient way. All conducted tests have been successful and prove that the concept works.

6 Conclusion and Future Work

This thesis deals with partial discharge (PD) measurements on power cables. If a distribution system operator (DSO) would monitor all power cables of its grid for PD, condition-based maintenance could be implemented to better manage the risk of supply interruptions. However, this is not practiced today due to a lack of low-cost and efficient PD sensors that are permanently installed at the power cable ends for continuous online monitoring. This work provides research on this topic and develops such a PD sensor. The main results of the thesis are briefly summarized below, followed by a final critical reflection of the developed sensor system and the identification of open research questions for future work.

The PD pulses are usually transmitted a distance along the power cable before being measured at its end. Power cables are designed for the transmission of 50 Hz currents and not for high-frequency (HF) signals and thus act like a low-pass for all PDs. Therefore, the bandwidth of PD signals is reduced depending on the distance transmitted. To develop an efficient PD sensor, the PD bandwidth at the cable ends must be known. To simulate the PD propagation, an analytical model that describes the transmission of HF signals, such as PD, on power cables is derived and validated in Chapter 2. The model is based on a solution of the telegrapher's equations. In addition, a calculation method of the propagation constant of power cables is presented and validated (the frequency dependency of all electrical parameters is considered). Simulations are then performed with this model to determine the bandwidth and amplitude loss of the transmitted PD pulses. It is concluded that the remaining bandwidth at the cable end is less than 10 MHz for most transmitted PD. An efficient PD sensor should therefore have maximum sensitivity within this bandwidth.

Based on the simulation results, a low-cost PD detector for power cables is developed in Chapter 3. The most promising type of PD sensor at a bandwidth of 10 MHz are high-frequency current transformers (HFCT) that use an inductive coupling principle between the power cable and the sensor. Accordingly, an optimal HFCT design for measuring PDs on power cables is investigated. To this end, an analytical HFCT model is first derived and validated against measurements. This model can then be used to calculate the transfer function of any HFCT, enabling simulative HFCT design. Subsequently, the influence of the core material, the secondary winding number and the core size on the HFCT transfer function is analyzed in detail. This knowledge is then used to determine an optimized HFCT design that best meets the requirements. Based on the investigations in this chapter, the sensor sensitivity could be maximized within the 10 MHz measurement bandwidth.

The HFCT is intended for online monitoring of power cables, but possible saturation effects due to the high 50 Hz operating current of the power cables are neglected in the

HFCT model, since it would otherwise be nonlinear and thus not analytically solvable. Accordingly, the developed HFCT design has been optimized for an unsaturated state only. However, when using HFCT for online PD measurements on power cables, core saturation is a major problem and must be avoided. Chapter 4 discusses in detail how to avoid magnetic saturation of the HFCT core. To get the developed HFCT less susceptible to saturation, its design is modified by using a split-core with two air gaps. The length of the air gaps should be large enough to avoid saturation, but not larger or the HFCT sensitivity will be compromised. The optimal air gap length depends mainly on the amplitude of the 50 Hz operating current of the power cable. Two ways to determine the optimal air gap length are shown, once experimentally and once by simulation. The split-core model developed for this purpose extends the previous HFCT model and enables a simple and computer-aided HFCT design process. Setting the optimal air gap length ensures that the HFCT core is always free of saturation. Successful online monitoring of power cables is only possible in this way. Since the current in the power cable changes constantly depending on the load, the optimal air gap length also changes over time.

Thus, to ensure maximum sensitivity at all times, the developed HFCT should be able to self-adjust the length of the air gaps of its split-core. The air gaps should be neither too short nor too large, but always close to the optimum for all 50 Hz operating currents. Chapter 5 presents a concept how such a split-core HFCT with active air-gap control can be realized. A corresponding prototype is made from 3D-printed parts and is equipped with a servomotor to drive the air gap. The servomotor is controlled by a microcontroller that measures and evaluates the saturation level of the HFCT core. It is experimentally shown, that the prototype works as intended and sets the air gap length close to optimum for all 50 Hz operating currents. The developed PD sensor can thus be used for online monitoring of power cables without running into magnetic saturation. Furthermore, the second part of the chapter explains how to detect the PD pulses in the HFCT output voltage. Once again, a microcontroller is used to digitize and process the analog voltage signal. To reduce the required sampling frequency of the analog-to-digital converter (ADC), an analog circuit for preprocessing the HFCT signal is shown. At the end, the preprocessed and digitized signal is analyzed with a robust PD detection algorithm. The influence of noise is taken into account.

The developed PD sensor with active air gap control solves the saturation problem of previous HFCT sensors in a simple but efficient way. It can be used for online monitoring without any restrictions. The sensor has a high sensitivity in a bandwidth of 0 – 10 MHz and is thus optimized for power cables. The sensor can probably be used on other assets, such as power transformers, but this needs to be verified in the future. Whether DSOs will equip their power cables with PD sensors in the future depends heavily on

the cost of such a system. The developed PD sensor remains cost-effective despite its improved technology. The components used in the prototype cost a total of about $ 80. For comparison, commercial HFCTs are much more expensive at about $ 500 – 2000 and they are still prone to magnetic saturation.

In summary, the developed PD sensor meets all the requirements defined in the introduction of this thesis. The main objective of this work, the development of a low-cost and efficient PD sensor for online monitoring of power cables, has thus been achieved. With the results of this thesis, a future implementation of condition-based maintenance is getting closer.

Besides all the positive results, there is still much to do. The following list shows the outstanding research and development issues of this thesis:

- Due to the magnetic forces, the sensor prototype of Fig. 5.2 tends to vibrate with short air gaps. The CAD design must be improved to reduce vibrations, e. g., by adding damping elements or changing the design of the sliding rail system for more stiffness. Lower vibrations lead to a more accurate THD calculation and thus to more precise air gap control.
- The maximum possible air gap of the prototype is currently 12.4 mm, such a large air gap is not required. The servo angle is almost always $\varphi < 60°$. Therefore, in order to better utilize the servo angle of 0 – 180°, the rotation-translation converter should be redesigned. The minimum step size of the servo motor of 0.0687 $\frac{\text{mm}}{1°}$ can thereby be reduced and the precision of the air gap control increased.
- Most parts of the prototype, including the rotation-translation converter, are printed with a simple FDM 3D printer. Printing the parts has low precision and may cause slippage between the gear wheel and gear rack. Perhaps it is better to use metal and high-precision manufacturing for these parts.
- The operational amplifier circuit of Fig. 5.4 can be further optimized. Currently, the amplifier sometimes overdrives, which of course affects the THD calculation. Maybe the gain should be readjusted or a rail to rail operational amplifier should be used instead of the LM324N type.
- The air gap control algorithm described in Fig. 5.6 can probably be further improved. Especially, the routine for shortening the air gap needs further improvement. Maybe it's better not to shorten the air gap after a fixed time t, but to look at the last actions in the past and work with a dynamic time and variable servo step size (brings some intelligence to the algorithm). The aim is to reduce the number of necessary servomotor actions and thus reduce energy consumption.

- Each servomotor action causes a small movement of the secondary winding. It must be checked whether the copper winding can withstand these stresses over a long period of time or whether fatigue failure will occur.
- It must be checked whether the servomotor is powerful enough to move the core smoothly even when the HFCT is mounted vertically. In all previous tests, the prototype was always horizontal and the weight of the core did not play a major role. In the vertical, the weight of the ferrite core stresses the servo even at halt.
- Heavy loads overheat and destroy the servomotor, e. g., if it is blocked. Therefore, the servo current should be measured and overload protection implemented.
- The analog peak detector circuit of Fig. 5.12 works only for positive PD pulses. In order to preprocess the negative pulses as well, the circuit has to be extended and tested both simulatively and experimentally.
- The peak detection algorithm shown on page 92 uses three free parameters (delay, threshold, influence). The parameters must be optimized for PD detection with a statistical optimization based on a large number of simulated or measured sample data. The performance of the algorithm must then be tested and evaluated again. What is the maximum signal-to-noise ratio at which PD pulses can be detected using this algorithm? Is there a better or more robust algorithm?
- The performance of the peak detection algorithm program code on page 92 can certainly be improved (avoid the for loop if possible). It must be ensured that the microcontroller running the algorithm is fast enough to process the ADC data in real-time.
- The sensor prototype currently uses two microcontrollers; only one should be used in the future. All sensor electronics should then be brought together on a printed circuit board (PCB), i. e., the microcontroller together with the analog circuits, which are shown in Fig. 5.4 and Fig. 5.12. The PCB design must follow the design rules for HF signals.
- The PCB board and all other sensor hardware then require a weatherproof housing for permanent outdoor installation. The design must allow for easy installation of the HFCT on power cables.
- The microcontroller and servomotor require a 5 V power supply, which is not yet implemented in the prototype. The voltage can perhaps be inductively decoupled from the power cable – this approach should be further researched (energy harvesting).
- All features of the PD sensor must be tested under real operating conditions (long-term test). Since the power cables are connected to the power grid, the amount of noise and interference will be much larger than in laboratory tests.

- To distinguish between linear and nonlinear HFCT operation, a THD threshold of 1 % has been used in this work, but in other environments harmonics and noise may result in a higher noise level for the 50 Hz measurement. It must be checked whether the THD threshold of 1 % still applies in such environments or how it must be adjusted. Probably a dynamic threshold that adapts to the actual background noise level would be best and should be researched in the future.
- For the HF measurement, there should be an additional feature to filter out periodic noise, such as that generated by inverters or other power electronics (harmonics).
- Further communication between PD sensor and DSO has not yet been developed. The communication protocol shall be based on the IEC 60870-5 standard and shall be added to the program code of the PD detection algorithm.
- The transmission line model from Chapter 2 was validated for XLPE medium voltage power cables. Presumably, it can also be used for XLPE high voltage power cables, but this remains to be verified.
- Regarding the transmission line model, it was stated that if multiple XLPE cable sections are connected by joints and their characteristic impedance is similar (this should usually be the case), the entire section can be treated as a single cable. This statement requires further verification.
- The HFCT model of Chapter 3 was validated neglecting parasitic inductance and capacitance. An accurate method for determining the parasitic elements of an HFCT is still needed. Only then the full HFCT model can be validated.
- The accuracy of the split-core HFCT model from Chapter 5 depends on the graphical construction of B_{Sat} and H_{Sat} of the ferrite material used. This step is prone to errors and needs to be done carefully. Therefore, a better and more robust method for determining B_{Sat} and H_{Sat} should be researched in the future.

So, it is obvious that the developed PD sensor needs further improvement, which will be done in the future. From today's perspective, the results of this thesis improve the knowledge on HFCT technology and provide new ideas on how to establish successful online monitoring in the future. In this way, condition-based maintenance of electrical grids moves one step closer.

References

[1] "Annual report on energy supply 2021 (german title: Die Energieversorgung 2021 - Jahresbericht)," tech. rep., BDEW German Association of Energy and Water Industries, Germany, June 2022. [Online] Available: https://www.bdew.de/service/anwendungshilfen/die-energieversorgung-2021/.

[2] C. Mayoux, "Degradation of insulating materials under electrical stress," *IEEE Transactions on Dielectrics and Electrical Insulation*, vol. 7, pp. 590–601, oct 2000.

[3] G. Montanari and L. Simoni, "Aging phenomenology and modeling," *IEEE Transactions on Electrical Insulation*, vol. 28, no. 5, pp. 755–776, 1993.

[4] "Zukünftige Rolle des Verteilnetzbetreibers in der Energiewende," tech. rep., BDEW German Association of Energy and Water Industries, Aug. 2017. [Online] Available: https://www.bdew.de/media/documents/20160906_Studie-E-Bridge-MITNETZ-DSO2.0-Paper.pdf.

[5] "Verteilnetzausbau für die Energiewende – Elektromobilität im Fokus," tech. rep., Agora Verkehrswende, Agora Energiewende, Regulatory Assistance Project (RAP), 2019. [Online] Available: https://static.agora-energiewende.de/fileadmin/Projekte/2018/Netzausbau_Elektromobilitaet/Agora-Verkehrswende_Agora-Energiewende_EV-Grid_WEB.pdf.

[6] *Key figures of supply interruptions electricity (German title: Kennzahlen der Versorgungsunterbrechungen Strom)*. Bundesnetzagentur Germany homepage. [Online], Sept. 2021. Available: https://www.bundesnetzagentur.de/DE/Fachthemen/ElektrizitaetundGas/Versorgungssicherheit/Versorgungsunterbrechungen/Auswertung_Strom/start.html.

[7] S. Boggs and J. Densley, "Fundamentals of partial discharge in the context of field cable testing," *IEEE Electrical Insulation Magazine*, vol. 16, pp. 13–18, sep 2000.

[8] R. Bartnikas, "Partial discharges. their mechanism, detection and measurement," *IEEE Transactions on Dielectrics and Electrical Insulation*, vol. 9, pp. 763–808, oct 2002.

[9] G. Stone, "Partial discharge diagnostics and electrical equipment insulation condition assessment," *IEEE Transactions on Dielectrics and Electrical Insulation*, vol. 12, pp. 891–903, oct 2005.

[10] "ISO/IEC 60270:2000, High-voltage test techniques – Partial discharge measurements."

[11] P. van der Wielen, J. Veen, P. Wouters, and E. Steennis, "Sensors for on-line PD detection in MV power cables and their locations in substations," in *Proceedings of the 7th International Conference on Properties and Applications of Dielectric Materials (Cat. No.03CH37417)*, IEEE, 2003.

[12] B. A. Siddiqui, P. Pakonen, and P. Verho, "Novel inductive sensor solutions for on-line partial discharge and power quality monitoring," *IEEE Transactions on Dielectrics and Electrical Insulation*, vol. 24, pp. 209–216, feb 2017.

[13] L. Mandache, A. Marinescu, and I. Dumbrava, "A high frequency current transformer with improved low frequency current capability," *Rev. Roum. Sci. Techn.– Électrotechn. et Énerg.*, vol. Vol 65, pp. 53 – 59, 2021.

[14] M. J. Foxall, A. P. Duffy, J. Gow, M. Seltzer-Grant, and L. Renforth, "Development of a new high current, hybrid 'ferrite-rogowski', high frequency current transformer for partial discharge sensing in medium and high voltage cabling," in *59th International Wire & Cable Symposium*, (Rhode Island Convention Centre, Providence, RI, USA), Nov. 2010.

[15] R. S. G. Heinzel, A. Rüdiger, "Spectrum and spectral density estimation by the discrete fourier transform (dft), including a comprehensive list of window functions and some new at-top windows.," tech. rep., Max-Planck Institut für Gravitationsphysik MPG, Feb. 2002.

[16] G. C. Stone, A. Cavallini, and G. Behrmann, "A review of the history of the development of partial discharge testing," in *2022 IEEE Electrical Insulation Conference (EIC)*, IEEE, jun 2022.

[17] M. Wild, S. Tenbohlen, E. Gulski, and R. Jongen, "Basic aspects of partial discharge on-site testing of long length transmission power cables," *IEEE Transactions on Dielectrics and Electrical Insulation*, vol. 24, pp. 1077–1087, apr 2017.

[18] R. V. Brunt, "Stochastic properties of partial-discharge phenomena," *IEEE Transactions on Electrical Insulation*, vol. 26, no. 5, pp. 902–948, 1991.

[19] A. Gaouda, A. El-Hag, T. Abdel-Galil, M. Salama, and R. Bartnikas, "On-line detection and measurement of partial discharge signals in a noisy environment," *IEEE Transactions on Dielectrics and Electrical Insulation*, vol. 15, pp. 1162–1173, aug 2008.

[20] S. Lu, H. Chai, A. Sahoo, and B. T. Phung, "Condition monitoring based on partial discharge diagnostics using machine learning methods: A comprehensive state-of-the-art review," *IEEE Transactions on Dielectrics and Electrical Insulation*, vol. 27, pp. 1861–1888, dec 2020.

[21] K. Bjorlow-Larsen, “High voltage cables at the turn of the century,” *IEEE Power Engineering Review*, vol. 20, no. 9, pp. 4–5, 2000.

[22] M. Mahdipour, A. Akbari, P. Werle, and H. Borsi, “Partial discharge localization on power cables using on-line transfer function,” *IEEE Transactions on Power Delivery*, vol. 34, pp. 1490–1498, aug 2019.

[23] M. Fritsch and M. Wolter, “Transmission model of partial discharges on medium voltage cables,” *IEEE Transactions on Power Delivery*, vol. 37, pp. 395–404, feb 2022.

[24] M. Fritsch and M. Wolter, “Measurable bandwidth of partial discharges on medium voltage cables,” in *2021 IEEE Power & Energy Society General Meeting (PESGM)*, IEEE, jul 2021.

[25] S. Boggs and G. Stone, “Fundamental limitations in the measurement of corona and partial discharge,” *IEEE Transactions on Electrical Insulation*, vol. EI-17, pp. 143–150, apr 1982.

[26] C. Herold, *Verfahren zur automatisierten Teilentladungsdiagnostik von Energiekabeln*. PhD thesis, Karlsruher Institut für Technologie, Karlsruhe, GER, 2012.

[27] J. Steiner, P. Reynolds, and W. Weeks, “Estimating the location of partial discharges in cables,” *IEEE Transactions on Electrical Insulation*, vol. 27, no. 1, pp. 44–59, 1992.

[28] P. Wagenaars, P. A. F. Wouters, P. J. M. V. D. Wielen, and E. Steennis, “Approximation of transmission line parameters of single-core and three-core XLPE cables,” *IEEE Trans. Dielectr. Electr. Insul.*, vol. 17, pp. 106–115, feb 2010.

[29] X. Hu, W. H. Siew, M. D. Judd, A. J. Reid, and B. Sheng, “Modeling of high-frequency current transformer based partial discharge detection in high-voltage cables,” *IEEE Trans. Power Del.*, vol. 34, pp. 1549–1556, aug 2019.

[30] Y. H. M. Thayoob, A. M. Ariffin, and S. Sulaiman, “Analysis of high frequency wave propagation characteristics in medium voltage XLPE cable model,” in *Proc. ICCAIE2010*, (Kuala Lumpur, Malaysia), pp. 665–670, dec 2010.

[31] M. Tozzi, A. Cavallini, G. Montanari, and G. Burbui, “PD detection in extruded power cables: an approximate propagation model,” *IEEE Trans. Dielectr. Electr. Insul.*, vol. 15, pp. 832–840, jun 2008.

[32] C. Herold and T. Leibfried, “Advanced signal processing and modeling for partial discharge diagnosis on mixed power cable systems,” *IEEE Trans. Dielectr. Electr. Insul.*, vol. 20, pp. 791–800, jun 2013.

[33] M. Leone, *Theoretische Elektrotechnik : elektromagnetische Feldtheorie für Ingenieure*. Wiesbaden: Springer Vieweg, 2018. pp. 371–376.

[34] W. H. Hayt and J. A. Buck, *Engineering electromagnetics*. McGraw-Hill series in electrical engineering, Boston, Mass. [u.a.], USA: McGraw-Hill, 6th ed ed., 2001. pp. 263-264 and pp. 301–322.

[35] K. W. Kark, *Antennen und Strahlungsfelder : elektromagnetische Wellen auf Leitungen, im Freiraum und ihre Abstrahlung*. Wiesbaden: Springer Vieweg, 7., überarbeitete und erweiterte ed., 2018.

[36] K. C. Gupta, *Computer-aided design of microwave circuits*. Dedham, MA, USA: Artech, 1981. pp. 30–39 and p. 59.

[37] W. Mathis and A. Reibiger, *Küpfmüller Theoretische Elektrotechnik : Elektromagnetische Felder, Schaltungen und elektronische Bauelemente*. Berlin: Springer Vieweg, 20., aktualisierte auflage ed., 2017. pp. 626–630.

[38] J. D. Jackson, *Classical electrodynamics*. New York [u.a.]: Wiley, 1962.

[39] H. Henke, *Elektromagnetische Felder : Theorie und Anwendung*. Springer-Lehrbuch, Berlin: Springer Vieweg, 5., erweiterte auflage ed., 2015.

[40] G. C. Stone and S. A. Boggs, "Propagation of partial discharge pulses in shielded power cable," in *Proc. IEEE CEIDP 1982*, oct 1982.

[41] G. Mugala, R. Eriksson, U. Gafvert, and P. Pettersson, "Measurement technique for high frequency characterization of semi-conducting materials in extruded cables," *IEEE Trans. Dielectr. Electr. Insul.*, vol. 11, pp. 271–280, jun 2004.

[42] E. C. Jordan and K. G. Balmain, *Electromagnetic Waves and Radiating Systems*. Prentice Hall India, 2nd edition ed., 1968. pp. 153 – 155.

[43] P. C. J. M. van der Wielen, *On-line Detection and Location of Partial Discharges in Medium-Voltage Power Cables*. PhD thesis, TU Eindhoven, Eindhoven, NL, Apr. 2005.

[44] J. Veen, *On-line signal analysis of partial discharges in medium voltage power cables*. PhD thesis, Eindhoven University of Technology, Eindhoven, NL, 2005.

[45] K. Steinbrich, "Influence of semiconducting layers on the attenuation behaviour of single-core power cables," *IEE Proceedings - Generation, Transmission and Distribution*, vol. 152, no. 2, p. 271, 2005.

[46] R. Papazyan, P. Pettersson, H. Edin, R. Eriksson, and U. Gafvert, "Extraction of high frequency power cable characteristics from s-parameter measurements," *IEEE Trans. Dielectr. Electr. Insul.*, vol. 11, pp. 261–270, June 2004.

[47] Y. Norouzi, S. Braun, C. Frohne, S. Seifi, and P. Werle, "Effect of cable joints on frequency domain analysis," in *2018 IEEE Conference on Electrical Insulation and Dielectric Phenomena (CEIDP)*, IEEE, oct 2018.

[48] M. Fritsch and M. Wolter, "High-frequency current transformer design and construction guide," *IEEE Transactions on Instrumentation and Measurement*, vol. 71, pp. 1–9, 2022.

[49] M. Fritsch and M. Wolter, "Determination of the optimal air gap of an HFCT," in *2023 IEEE Power & Energy Society Innovative Smart Grid Technologies Conference (ISGT)*, IEEE, jan 2023.

[50] J. V. Kluss, A.-P. Elg, and C. Wingqvist, "High-frequency current transformer design and implementation considerations for wideband partial discharge applications," *IEEE Transactions on Instrumentation and Measurement*, vol. 70, pp. 1–9, 2021.

[51] P. M. Sánchez, F. J. R. Sánchez, and E. S. Gómez, "An experimental strategy for characterizing inductive electromagnetic energy harvesters," *Sensors*, vol. 20, p. 647, jan 2020.

[52] C. McLyman, *Transformer and Inductor Design Handbook*. CRC Press, 2011. pp. 16–26.

[53] M. Getzlaff, *Fundamentals of Magnetism*. Springer Berlin Heidelberg, 2010. pp. 139–141.

[54] Material Data Sheets. (2021, Jun.) Fair-Rite Products Corp. homepage. [Online]. Available: `https://www.fair-rite.com/materials/`.

[55] N. Ahmed and N. Srinivas, "On-line partial discharge detection in cables," *IEEE Transactions on Dielectrics and Electrical Insulation*, vol. 5, pp. 181–188, apr 1998.

[56] C. Zachariades, R. Shuttleworth, R. Giussani, and R. MacKinlay, "Optimization of a high-frequency current transformer sensor for partial discharge detection using finite-element analysis," *IEEE Sensors Journal*, vol. 16, pp. 7526–7533, oct 2016.

[57] N. A. Spaldin, *Magnetic Materials*. Cambridge University Press, 2014. pp. 120-125.

[58] D. J. Griffiths, *Introduction to Electrodynamics*. Cambridge University Press, 2017. pp. 247-250.

[59] K. Poulsen, *SDR-Kits Female Calibration Kit of Rosenberger parts for the DG8SAQ VNWA*, revision 5 ed., May 2017. [Online] Available: https://www.sdr-kits.net/documents/Rosenberger_Female_Cal_Standards_rev5.pdf.

[60] J. V. Kluss and A.-P. Elg, "Challenges associated with implementation of HFCTs for partial discharge measurements," in *2020 Conference on Precision Electromagnetic Measurements (CPEM)*, IEEE, July 2020.

[61] M. Fritsch and M. Wolter, "Saturation of high-frequency current transformers: Challenges and solutions," *IEEE Transactions on Instrumentation and Measurement*, vol. 72, pp. 1–10, 2023. Early Access.

[62] I. Daut, S. Hasan, S. Taib, R. Chan, and M. Irwanto, "Harmonic content as the indicator of transformer core saturation," in *4th International Power Engineering & Optimization Conf. (PEOCO2010)*, (Shah Alam, Malaysia), IEEE, jun 2010.

[63] D. Shmilovitz, "On the definition of total harmonic distortion and its effect on measurement interpretation," *IEEE Transactions on Power Delivery*, vol. 20, pp. 526–528, jan 2005.

[64] P. Horowitz and W. Hill, *The Art of Electronics*. Cambridge University Pr., 2015. pp. 225 ff.

[65] Feetech RC Model Co., Ltd., *MG90S Servomotor Datasheet*, v1.0 ed. [Online] Available: https://bit.ly/3ywvGnk (version: 2023-13-03).

[66] NXP Semiconductors, *LPC4370 Datasheet*, rev. 2.4 ed., Jan. 2020. [Online] Available: https://www.nxp.com/docs/en/data-sheet/LPC4370.pdf.

[67] Texas Instruments, *OPA615 Datasheet*, sbos299e ed., Feb. 2014. [Online] Available: https://www.ti.com/lit/ds/symlink/opa615.pdf?ts=1678700929048&ref_url=https%253A%252F%252Fwww.ti.com%252Fproduct%252FOPA615.

[68] K. Achtenberg, J. Mikolajczyk, D. Szabra, A. Prokopiuk, and Z. Bielecki, "Review of peak signal detection methods in nanosecond pulses monitoring," *Metrology and Measurement Systems*, vol. 27, no. 2, pp. 203–218, 2020.

[69] V. Aristov and A. Ancans, "Transient phenomena analysis of peak detector for nanosecond pulse amplitude measurement," *Automatic Control and Computer Sciences*, vol. 56, pp. 587–594, dec 2022.

[70] W. Haas and P. Dullenkopf, "A novel peak amplitude and time detector for narrow pulse signals," *IEEE Transactions on Instrumentation and Measurement*, vol. IM-35, pp. 547–550, dec 1986.

[71] J. v. Brakel, "Robust peak detection algorithm using z-scores," 2014. Stack Overflow. [Online] Available: `https://stackoverflow.com/questions/22583391/peak-signal-detection-in-realtime-timeseries-data/22640362#22640362` (version: 2020-11-08).

[72] S. Chandrasekar, A. Cavallini, G. Montanari, and F. Puletti, "Bandwidth and sensitivity issues in PD detection in power cables," *IEEE Transactions on Dielectrics and Electrical Insulation*, vol. 14, pp. 735–743, jun 2007.

Res Electricae Magdeburgenses

MAgdeburger FOrum zur Elektrotechnik

MAFO-01 Orths, A.: *Multikriterielle, optimale Planung von Verteilungsnetzen im liberalisierten Energiemarkt unter Verwendung von spieltheoretischen Verfahren*, 2003. ISBN 3-929757-57-5.

MAFO-02 Purmann, M.: *Optimierung des Betriebsverhaltens von PEM-Brennstoffzellen unter Berücksichtigung von elektrischem und Gesamtwirkungsgrad bei unterschiedlichen Lastanforderungen und Betriebsparametern*, 2004. ISBN 3-929757-63-X.

MAFO-03 Al-Hamid, M.: *Extraktion von höheren Moden in TEM-Wellenleitern*, 2004. ISBN 3-929757-64-8.

MAFO-04 Haase, H., J. Nitsch, and T. Steinmetz: *Transmission-Line Super Theory – A new Approach to an Effective Calculation of Electromagnetic Interference*, 2004. ISBN 3-929757-67-2.

MAFO-05 Bachry, A.: *Power Quality Studies in Distribution Systems Involving Spectral Decomposition*, 2004. ISBN 3-929757-68-0.

MAFO-06 Styczynski, Z. A.: *Power Network and Renewables – A Scientific Report*, 2004. ISBN 3-929757-69-9.

MAFO-07 Blume, E.: *Numerische Analyse der Kopplung linearer Antennen innerhalb eines Resonators*, 2004. ISBN 3-929757-71-0.

MAFO-08 Handschin, E. and Z. A. Styczynski: *Power System Application of the Modern Battery Storage*, 2004. ISBN 3-929757-75-3.

MAFO-09 Haase, H.: *Full-Wave Field Interactions of Nonuniform Transmission Lines*, 2005. ISBN 3-929757-78-8.

MAFO-10 Nitsch, D.: *Die Wirkung eingekoppelter ultrabreitbandiger elektromagnetischer Impulse auf komplexe elektronische Systeme*, 2005. ISBN 3-929757-79-6.

MAFO-11 Hadzi-Kostova, B.: *Protection Concepts in Distribution Networks with Decentralized Energy Resources*, 2005. ISBN 3-929757-84-2.

MAFO-12 Steinmetz, T.: *Ungleichförmige und zufällig geführte Mehrfachleitungen in komplexen technischen Systemen*, 2006. Nummerierung geändert, ISBN 3-929757-98-2.

MAFO-13 Styczynski, Z. and J. Haubrock: *Influence of Distributed and Renewable Generation on Power System Security – Proceedings of the CRIS Workshop 2006*, 2006. ISBN 3-929757-99-0.

MAFO-14 Heideck, G.: *Ein autonomes Brennstoffzellensystem: Optimierungsansätze*, 2006. ISBN 3-929757-94-X.

MAFO-15 Styczynski, Z. und H.-D. Musikowski: *Dresdener Kreis Elektroenergieversorgung 7*, 2006. ISBN 3-929757-85-0.

MAFO-16 Gronwald, F.: *Antenna Theory in Resonating Systems derived from Fundamental Electromagnetism*, 2007. ISBN 3-929757-93-1.

MAFO-17 Krauthäuser, H.G.: *Grundlagen und Anwendungen von Modenverwirbelungskammern*, 2007. ISBN 978-3-929757-43-9.

MAFO-18 Dzienis, C.: *Ersatzmodelle nichtlinearer Lasten in elektrischen Verteilungsnetzen*, 2007. ISBN 978-3-929757-07-1.

MAFO-19 Styczynski, Z. and J. Haubrock: *Renewable and Dispersed Power Generation in Power Systems*, 2007. ISBN 978-3-929757-44-6.

MAFO-20 Haubrock, J.: *Parametrierung elektrischer Äquivalentschaltbilder von PEM-Brennstoffzellen*, 2008. ISBN 978-3-940961-02-0.

MAFO-21 Angelov, A. N.: *Rechnergestütztes Lernen im Bereich der Regenerativen Energien (Ausgewählte Aspekte)*, 2008. ISBN 978-3-940961-03-7.

MAFO-22 Komarnicki, P.: *Anwendung hochgenauer, synchroner Messungen zur Verbesserung des Betriebs von Verteilungsnetzen*, 2008. ISBN 978-3-940961-04-4.

MAFO-23 Roggatz, C.: *Trainingssimulator für die Führung von elektrischen Systemen mit dezentralen Energieeinspeisungen – Trainingsszenarien und Umsetzung*, 2008. ISBN 978-3-940961-05-1.

MAFO-24 Rudion, K.: *Aggregated Modelling of Wind Farms*, 2008. ISBN 978-3-940961-14-3.

MAFO-25 Ganjavi, M. R.: *Protection System Coordination Using Expert System*, 2008. ISBN 978-3-940961-15-0.

MAFO-26 Bofinger, S.: *Energieversorgungsnetze mit einem hohen Anteil an photovoltaischer Solarenergie: Standortbestimmung, Solarstromprognose, Netzintegration*, 2008. ISBN 978-3-940961-25-9.

MAFO-27 Styczynski, Z. and P. Komarnicki: *Distributed and Renewable Power Generation*, 2008. ISBN 978-3-940961-26-6.

MAFO-28 Kochetov, S. V.: *Time- and Frequency-Domain Modeling of Passive Interconnection Structures in Field and Circuit Analysis*, 2008. ISBN 978-3-940961-27-3.

MAFO-29 Magdowski, M.: *Entwicklung und Validierung eines Werkzeugs zur Berechnung der elektromagnetischen Einkopplung von stochastischen Feldern in Leitungsstrukturen*, 2008. ISBN 978-3-940961-28-0.

MAFO-30 Sonnemann, F.: *Elektromagnetische Effekte an elektrischen Zündmitteln (EED) mit angeschlossener Zündkreiselektronik (ZKE) bei impulsförmiger, breitbandiger Bestrahlung*, 2009. ISBN 978-3-940961-32-7.

MAFO-31 Smieja, T.: *Multikriterielle Planung interregionaler Elektrizitätsnetze im liberalisierten Energiemarkt*, 2009. ISBN 978-3-940961-35-8.

MAFO-32 Heyde, C. O.: *Dynamic Voltage Security Assessment for On-Line Control Room Application*, 2010. ISBN 978-3-940961-40-2.

MAFO-33 Styczynski, Z. A. and N. I. Voropai (Editors): *Renewable Energy Systems Fundamentals, Technologies, Techniques and Economics*, 2010. ISBN 978-3-940961-42-6.

MAFO-34 Styczynski, Z. A. и N. I. Voropai (Editors): Renewable Energy Systems Fundamentals, Technologies, Techniques and Economics (Russian Version), 2010. ISBN 978-3-940961-44-0.

MAFO-35 Styczynski, Z. A. and A. Lindemann (Editors): *Integration of Renewable Energies into the Grid / Proceedings of the Power & Energy Student Summit 2010*, 2010. ISBN 978-3-940961-47-1.

MAFO-36 Styczynski, Z. A. und H.-D. Musikowski (Editors): *Dresdener Kreis Elektroenergieversorgung 11*, 2010. ISBN 978-3-940961-51-8.

MAFO-37 Gurbiel, M. A.: *Definition and Testing of a Digital Interface of a Power Substation*, 2011. ISBN 978-3-940961-54-9.

MAFO-38 Lombardi, P.: *Multi Criteria Optimization of an Autonomous Virtual Power Plant*, 2011. ISBN 978-3-940961-55-6.

MAFO-39 Powalko, M.: *Beobachtbarkeit eines elektrischen Verteilungsnetzes – Ein Beitrag zum Smart Grid*, 2011. ISBN 978-3-940961-62-4.

MAFO-40 Styczynski, Z. A., K. Rudion, and C. Nguyen-Mau (Editorial Board): *Power System Dynamic Security Assessment*, 2011. ISBN 978-3-940961-61-7.

MAFO-41 Käbisch, M: *Optimale Dimensionierung und Betriebsführung einer brennstoffzellenbasierten Auxiliary Power Unit im Fahrzeug*, 2011. ISBN 978-3-940961-67-9.

MAFO-42 Styczynski, Z. A. und N. I. Voropai (Editors): *Special Issue Grant 220 Russian Federation SSmart Grid for Efficient Energy Power System for the Future", Proceedings Volume I*, 2012. ISBN 978-3-940961-74-7.

MAFO-43 Styczynski, Z. A., P. Komarnicki und A. Naumann (Editors): *Abschlussbericht Harz.ErneuerbareEnergien-mobility*, 2012. ISBN 978-3-940961-71-6.

MAFO-44 Heuer, M.: *Diagnosetool für stationär betriebene PEM-Brennstoffzellensysteme*, 2012. ISBN 978-3-940961-77-8.

MAFO-45 Stötzer, M.: *Demand Side Integration in elektrischen Verteilnetzen – Potenzialanalyse und Bewertung*, 2012. ISBN 978-3-940961-78-5.

MAFO-46 Magdowski, M.: *Vergleich der Einkopplung deterministischer und statistischer elektromagnetischer Felder in Leitungen*, 2012. ISBN 978-3-940961-75-4.

MAFO-47 Naumann, A.: *Leitwarte im Smart Grid*, 2012. ISBN 978-3-940961-81-5.

MAFO-48 Rudion, K.: *Offshore Power System Planning – Selected Aspects*, 2012. ISBN 978-3-940961-82-2.

MAFO-49 Nguyen-Mau, C.: *Electric Power System Stability Enhancement by Voltage Source Converter based High Voltage Direct Current Technology*, 2012. ISBN 978-3-940961-84-6.

MAFO-50 Guo, H.: *Measurement-Based Load Modeling for Smart Grid Planning*, 2012. ISBN 978-3-940961-86-0.

MAFO-51 Styczynski, Z. A.: *Proceedings No. 2 in the Scope of Mega Grant Baikal*, 2013. ISBN 978-3-940961-95-2.

MAFO-52 Styczynski, Z. A.: *Proceedings No. 3 in the Scope of Mega Grant Baikal*, 2013. ISBN 978-3-940961-98-3.

MAFO-53 Wenge, C.: *Optimaler Betrieb von mobilen Speichern im Smart Grid. -Mobilitätsleitwarte-* , 2013. ISBN 978-3-944722-01-6.

MAFO-54 Röhrig, C.: *Smart Distribution Planung unter Berücksichtigung von residualen Lasten*, 2014. ISBN 978-3-944722-06-1.

MAFO-55 Middelstädt, F.: *Research of SEM Poles of Complex Wire Structures*, 2014. ISBN 978-3-944722-07-8.

MAFO-56 Styczynski, Z. A. (Editor): *Power Network and Renewables – A Scientific Report – 15 Years Research*, 2014. ISBN 978-3-944722-08-5.

MAFO-57 Solonina, N. N., V. S. Stepanov, and K. V. Suslov: *Information technology in intelligent power networks*, 2014. ISBN 978-3-944722-13-9.

MAFO-58 Krebs, R.: *Fundamentals of Power System Protection*, 2014. ISBN 978-3-944722-15-3.

MAFO-59 Moskalenko, N.: *Optimal Dynamic Energy Management System in Smart Homes*, 2014. ISBN 978-3-944722-16-0.

MAFO-60 Hauer, I.: *Optimale Last- und Erzeugungsanpassung bei kritischen Netzzuständen – Algorithmen und deren Bewertung*, 2014. ISBN 978-3-944722-18-4.

MAFO-61 Richter, M.: *Dresdner Kreis Elektroenergieversorgung 15, Begleitband zum Workshop 2014*, 2014. ISBN 978-3-944722-21-4.

MAFO-62 Styczynski, Z. A., A. Richter und P. Kühne: *Second ELECON Workshop – Begleitband zum Workshop 2014*, 2014. ISBN 978-3-944722-23-8.

MAFO-63 Bernstein, P.: *Modellgestützte optimale Betriebsführung von PEM-Brennstoffzellen für autonome Anlagen*, 2015. ISBN 978-3-944722-24-5.

MAFO-64 Rabe, S.: *Betrieb einer Zweipunkt-Offshore-HGÜ-Verbindung – Modelluntersuchungen*, 2015. ISBN 978-3-944722-31-3.

MAFO-65 Arendarski, B.: *Reliability Assessment of Smart Grids*, 2015. ISBN 978-3-944722-32-0.

MAFO-66 Pan, X.: *Numerisches EMV-Simulationsverfahren zur Berechnung der Störaussendung elektrischer Antriebssysteme in Hybridfahrzeugen*, 2016. ISBN 978-3-944722-34-4.

MAFO-67 Richter, M.: *PMU-basierte Zustandsabschätzung in Smart Distribution*, 2016. ISBN 978-3-944722-43-6.

MAFO-68 Bielchev, I.: *Adaptiver Distanzschutz im Standard IEC 61850*, 2016. ISBN 978-3-944722-45-0.

MAFO-69 Hassan, A.: *Modeling of Single and Double-Shielded Cables for EMC Applications*, 2016. ISBN 978-3-944722-41-2.

MAFO-70 Liu, X.: *Control of Voltage Source Converter Based High Voltage Direct Current Transmission Systems for Grid Code Compliance*, 2016. ISBN 978-3-944722-46-7.

MAFO-71 Kaiser, M.: *Fusion of Interventional Ultrasound & X-ray*, 2016. ISBN 978-3-944722-51-1.

MAFO-72 Grieger, F.: *Ein Beitrag zur Bestimmung der Zuverlässigkeit von Leistungshalbleiterbauelementen unter Berücksichtigung der Anwendung*, 2016. ISBN 978-3-944722-52-8.

MAFO-73 Li, M.: *Towards a Robust Electromagnetic Tracking System for Use in Medical Applications*, 2018. ISBN 978-3-944722-66-5.

MAFO-74 Klabunde, C., J. Dancker, N. Gast, T. Schröter, F. Schulz, J. Rossberg und A. Richter: *Statusbericht der Otto-von-Guericke-Universität Magdeburg zum Verbundprojekt: Intelligentes Multi-Energie-System (SmartMES)*, 2018. ISBN 978-3-944722-69-6.

MAFO-75 Schröter, T.: *19. Dresdner Kreis Elektroenergieversorgung, Begleitband zum Workshop 2018 in Magdeburg*, 2018. ISBN 978-3-944722-79-5.

MAFO-76 Klabunde, C., J. Dancker, N. Gast, T. Schröter, F. Schulz und J. Rossberg: *Intelligentes Multi-Energie-System (SmartMES) – Statusbericht der Otto-von-Guericke-Universität Magdeburg zum Verbundprojekt, 2. Statusseminar 04. April 2019 in Magdeburg*, 2019. ISBN 987-3-944722-80-1.

MAFO-77 Helm, S., J. Dancker, M. Fritsch und T. Schröter: *Power and Energy Student Summit 2019, 09.–11. Juli*, 2019. ISBN 978-3-944722-84-9.

MAFO-78 Chychykina, I.: *Comparison of Different Redispatch Optimization Strategies*, 2019. ISBN 978-3-944722-89-4.

MAFO-79 Balischewski, S.: *Multifunktionaler Einsatz von Batteriespeichern in elektrischen Verteilnetzen*, 2020. ISBN 978-3-944722-92-4.

MAFO-80 Petzold, J.: *Analytische Beschreibung der Kopplung elektromagnetischer Felder durch Aperturen in Resonatoren*, 2020. ISBN 978-3-944722-91-7.

MAFO-81 Middelstädt, L.: *Transiente Effekte in leistungselektronischen Schaltungen mit schnellschaltenden Leistungshalbleitern unter besonderer Berücksichtigung der elektromagnetischen Verträglichkeit*, 2020. ISBN 978-3-944722-95-5.

MAFO-82 Liu, Y.: *Contribution to Improve the EMI Performance of Electrical Drive Systems in Vehicles With Special Consideration of Power Semiconductor Modules*, 2021. ISBN 978-3-948749-01-9.

MAFO-83 Gerlach, A.: *Regelung von direktangetriebenen elektrischen Maschinen für Verbrennungsmotoren*, 2021. ISBN 978-3-948749-03-3.

MAFO-84 Zhang, Y.: *Analysis and Control of Resonances in HVDC Connected DFIG-Based Offshore Wind Farms*, 2021. ISBN 978-3-948749-05-7.

MAFO-85 Pannicke, E.: *Empfangsspulen für bildgeführte Eingriffe mittels Magnetresonanztomographie*, 2021. ISBN 978-3-948749-12-5.

MAFO-86 Kasper, J.: *Analysis of the Stochastic Electromagnetic Field Coupling to Single and Multiconductor Transmission Line Structures*, 2021. ISBN 978-3-948749-13-2.

MAFO-87 Hauer, I.: *Abschlussbericht zum Projekt InKola: Infrastrukturkopplung – Platzierung und Betrieb von Ladestationen aus Verkehrs- und Energienetzsicht*, 2022. ISBN 978-3-948749-15-6.

MAFO-88 Raya, M.: *Circuit Models of Shielded Single and Multiconductor Cables for EMC Analyses*, 2022. ISBN 978-3-948749-16-3.

MAFO-89 Pribahsnik, F.: *GaN-Specific Mechanical Phenomena and Their Influence on Reliability in Power HEMT Operation*, 2022. ISBN 978-3-948749-17-0.

MAFO-90 Willmann, B.: *Elektromagnetische Umweltverträglichkeit eines Elektrofahrzeugs mit kontaktlosem Ladesystem*, 2022. ISBN 978-3-948749-19-4.

MAFO-91 Dancker, J.: *Sensitivity Factors for Integrated Energy Systems: A Joined Quasi-Steady-State Approach*, 2022. ISBN 978-3-948749-24-8.

MAFO-92 Tayyab, M.: *Holistic Approach for Microgrid Planning and Operation for E-Mobility Infrastructure Under Consideration of Multi-Type Uncertainties*, 2022. ISBN 978-3-948749-25-5.

MAFO-93 Richter, A.: *Virtuelle Kraftwerke im Verteilnetz – Systemstützender Betrieb im wirtschaftlichen Kontext – Eine gesamtheitliche Betrachtung virtueller Kraftwerke*, 2022. ISBN 978-3-948749-28-6.

MAFO-94 Woldu, T.: *Modeling and Simulation of Power System Dynamics for Studying the Impacts of Increasing Wind Power in a Weak Grid System*, 2022. ISBN 978-3-948749-31-6.

MAFO-95 Könneke, N.: *Entwurf eines Testbetts für Assistenzsysteme in der Netz- und Systemführung*, 2023. ISBN 978-3-948749-32-3.

MAFO-96 Glende, E. und M. Gebhardt: *23. Dresdner Kreis Elektroenergieversorgung, Begleitband zum Workshop 2022 in Magdeburg*, 2022. ISBN 978-3-948749-33-0.

MAFO-97 Kempiak, C.: *Lastwechselmethoden für Siliziumkarbid-MOSFETs unter Berücksichtigung von deren Schwellspannungsinstabilität*, 2023. ISBN 978-3-948749-38-5.